T.C.

DOKUZ EYLÜL UNIVERSITY

IZMIR INTERNATIONAL BIOMEDICINE AND GENOME INSTITUTE

EPIGENETIC REGULATION OF EPITHELIAL TO MESENCHYMAL TRANSITION (EMT) BY HISTONE VARIANT H3.3

ESİN ŞEKEROĞLU

DEPARTMENT OF MOLECULAR BIOLOGY AND GENETICS

DOCTOR OF PHILOSOPHY THESIS

IZMIR-2025

THESIS CODE: 10590940

T.C.
DOKUZ EYLÜL UNIVERSITY

IZMIR INTERNATIONAL BIOMEDICINE AND GENOME INSTITUTE

EPIGENETIC REGULATION OF EPITHELIAL TO MESENCHYMAL TRANSITION (EMT) BY HISTONE VARIANT H3.3

DEPARTMENT OF MOLECULAR BIOLOGY AND GENETICS

DOCTOR OF PHILOSOPHY THESIS

ESIN ŞEKEROĞLU

Thesis Supervisor:

Assoc. Prof. Dr. HANI ALOTAIBI

This thesis was supported by
TUBİTAK grant 118C354, 122N046 and 122Z886

IZMIR-2025

THESIS CODE: 10590940

Dokuz Eylül University Izmir International Biomedicine and Genome Institute Department of Genomics and Molecular Biotechnology, Molecular Biology and Genetics graduate program Doctor of Philosophy student Esin Şekeroğlu has successfully completed her Doctor of Philosophy thesis titled **"EPIGENETIC REGULATION OF EPITHELIAL TO MESENCHYMAL TRANSITION (EMT) BY HISTONE VARIANT H3.3"** on the date of 01/08/2025

Assoc. Prof. Dr. Hani Alotaibi
Dokuz Eylül University
CHAIR

Prof. Dr. Şerif Şentürk
Dokuz Eylül University
MEMBER

Prof. Dr. Ralph Meuwissen
Ege University
MEMBER

Assoc. Prof. Dr. Sinan Güven
Dokuz Eylül University
MEMBER

Assoc. Prof. Dr. Ayşe Banu Demir
İzmir Ekonomi University
MEMBER

Prof. Dr. Gökhan Karakülah
Dokuz Eylül University
SUBSTITUTE MEMBER

Prof Dr. Hatice Güneş Özhan
Dokuz Eylül University
SUBSTITUTE

Dokuz Eylül Üniversitesi İzmir Uluslararası Biyotıp ve Genom Enstitüsü Genom Bilimleri ve Moleküler Biyoteknoloji Anabilim Dalı, Moleküler Biyoloji ve Genetik Doktora programı öğrencisi Esin Şekeroğlu,

"EPİTELYALDEN MEZENKİMALE GEÇİŞİN H3.3 HİSTON VARYANTI İLE EPİGENETİK REGÜLASYONU" konulu Doktora tezini 01/08/2025 tarihinde başarılı olarak tamamlamıştır.

Doç. Dr. Hani Alotaibi
Dokuz Eylül University
BAŞKAN

Prof. Dr. Şerif Şentürk
Dokuz Eylül University
ÜYE

Prof. Dr. Ralph Meuwissen
Ege University
ÜYE

Doç. Dr. Sinan Güven
Dokuz Eylül University
ÜYE

Doç Dr. Ayşe Banu Demir
İzmir Ekonomi University
ÜYE

Prof. Dr. Gökhan Karakülah
Dokuz Eylül University
YEDEK ÜYE

Prof Dr. Hatice Güneş Özhan
Dokuz Eylül University
YEDEK ÜYE

CONTENTS

I. LIST OF ABBREVIATIONS....3
II. INDEX OF TABLES....4
III. INDEX OF FIGURES....5
IV. ACKNOWLEDGEMENTS....7
1. INTRODUCTION AND AIM....11
1.1. Aim of Study....11
1.2. Hypothesis of The Study....11
2. GENERAL INFORMATION....12
2.1. Epithelial to Mesenchymal Transition....12
2.2. Signalling Pathways and Transcriptional Networks on Regulation of EMT....12
2.3. Epithelial to Mesenchymal Transition in Physiological and Pathological Contexts....15
2.4. Human, Murine, and Pluripotent Cell Lines as Model Systems for EMT Studies....16
2.5. Chromatin organization and Histone proteins....17
2.6. Histone Variant H3.3 and Its Role in Chromatin Dynamics....19
3. MATERIALS AND METHODS....22
3.1. Type of the Study....22
3.2. Time and Place of the Study....22
3.3. Population and Samples of the Study....22
3.4. Research Material....22
3.5. Tools for Data Collection....22
3.5.1. Cell Culture....22
3.5.2. Characterization of MCF10A Cells for EMT Induction by TGFβ3....23
3.5.3. Neuronal Differentiation of mESCs as a Developmental EMT Model....24
3.5.4. Expression and Purification of Recombinant Mouse LIF....25
3.5.5. Immunofluorescence Staining and Confocal Microscopy....27
3.5.6. siRNA Transfection....27
3.5.7. mRNA Expression Analysis....28
3.5.8. Protein Purification and Western Blot Analysis....29
3.5.9. Cell Nucleus Size and Foci Analysis....30
3.5.10. Flow Cytometry Analysis....30
3.5.11. Single Cell Sorting and Expansion....30
3.5.12. RNA-seq Analysis....30
3.5.13. Cell Cycle Analysis....31
3.5.14. Growth Curve and Srb Assays....31
3.5.15. Chromatin Immunoprecipitation....31
3.5.16. Statistical Analysis....32
3.6. Planning and Calendar of the Study....32
3.7. Limitations of Study....33
3.8. Ethical Committee....33
4. RESULTS....34
4.1. Comparative Assessment of EMT Marker Expression Across Multiple Cell Models as MCF10A, NMuMG, and Embryonic Stem Cells Undergoing Neuronal Differentiation....34
4.2. Transcriptional Analysis of EMT Markers and H3.3A Expression Across Cell Models....36
4.3. H3.3A Knockdown Does Not Induce EMT in NMuMG Cells....37

4.4. siRNA-Mediated Knockdown of H3.3A Produces Variable Effects on Cell Morphology and CDH1 Expression 38
4.5. siRNA Target Sites and Splice Variant-Specific Depletion of H3.3A in MCF10A Cells 39
4.6. H3.3A Depletion and TGFβ3 Treatment Induce Similar Morphological Changes and Cytoskeletal Remodelling 40
4.7. MCF10A cells' heterogeneity misleading the effect of TGFβ3 on EMT studies 44
4.8. TGFβ3-Induced EMT in Single-Cell Derived MCF10A Clones Reveals Persistent Morphological and Cytoskeletal Heterogeneity 47
4.9. Forskolin Affects TGFβ3-Induced Epithelial-to-Mesenchymal Transition in MCF10A Cells at Morphological and Molecular Levels 52
4.10. EpCAM Expression Dynamics Under Forskolin Treatment Reveal Distinct Subpopulations and Their Association with EMT in MCF10A Cells 55
4.11. Dual CDH1 and EpCAM Sorting Reveals Enhanced Resolution of Epithelial Heterogeneity and EMT Dynamics in MCF10A Cells 56
4.12. MCF10A cells gain increased proliferation rate by Fsk treatment 58
4.13. TGFβ3 Treatment Reduces Transcriptomic Heterogeneity and Induces EMT-Associated Gene Expression in MCF10A Cells 60
4.14. H3.3A Depletion Drives EMT-Like and Cell Cycle Regulatory Changes with Overlapping and Distinct Features with Canonical TGFβ3 Response 62
4.15. HIRA Knockdown Induces Variable EMT-Like Phenotypes and Transcriptional Reprogramming in MCF10A Cells Similar to H3.3A Depletion 63
4.16. H3.3A Depletion Disrupts G1/S Transition and Decreases Cell Proliferation in MCF10A Cells 66
4.17. HIRA Knockdown Impairs H3.3 and ELF3 Deposition at Epithelial Gene Regulatory Regions 68
5. DISCUSSION 70
6. CONCLUSIONS AND SUGGESTIONS 75
7. REFERENCES 77
8. APPENDIX 84
8.1. Ethics Approval 84
8.2. Publications 85
8.3. Poster Presentations 97
8.3.1. 14th EMBO Young Scientists' Forum 97
8.3.2. TBS International Biochemistry Congress 98
8.3.3. MolBiyoKon 2022 99
8.4. Curriculum Vitae in Arbis Format 100

I. LIST OF ABBREVIATIONS

CABIN1	:	Calcineurin-Binding Protein 1
cAMP	:	Cyclic Adenosine Monophosphate
CHD1	:	Chromodomain Helicase DNA-binding Protein 1
E-Cad (CDH1)	:	E-Cadherin
EGF	:	Epidermal Growth Factor
ELF3	:	E74-Like Factor 3 (Ets Domain Transcription Factor)
EMT	:	Epithelial-Mesenchymal Transition
EMT-TFs	:	EMT-associated transcription factors
EpCAM	:	Epithelial Cell Adhesion Molecule
ESC	:	Embryonic Stem Cells
FN1	:	Fibronectin 1
GRHL3	:	Grainyhead Like Transcription Factor 3
HIRA	:	Histone Cell Cycle Regulator-A
MCF10A	:	a non-malignant human mammary gland cell
MET	:	Mesenchymal-Epithelial Transition
MyC	:	Myelocytomatosis oncogene
N-Cad (CDH2)	:	N-Cadherin
NMuMG	:	Normal Murine Mammary Gland
OCLN	:	Occludin
OVOL2	:	Ovo Like Zinc Finger 2
RNAi	:	RNA interference
SMAD	:	Small mother against decapentaplegic
SNAI	:	Snail Family Zinc Finger
TGFβ	:	Transforming Growth Factor Beta
TWIST	:	Twist-related protein 1
UBN1	:	Ubinuclein-1
ZEB2	:	Zinc Finger E-Box Binding Homeobox 1

II. INDEX OF TABLES

Table 1. Gene list 13
Table 2. Primers used for qPCR for analysis of neuronal differentiation of mESCs. 25
Table 3. Primers used for recombinant LIF production 25
Table 4. Antibodies used in this study 27
Table 5. Sequences and targets of siRNAs 28
Table 6. RT-PCR primers for amplification of H3.3A splice variants 28
Table 7. List of primers used for qPCR 29
Table 8. Primers used for qPCR 32

III. INDEX OF FIGURES

Figure 1. TGFβ Signalling Pathways in EMT Regulation. 13
Figure 2. Protein interaction network of EMT-related genes. 14
Figure 3. Three types of epithelial to mesenchymal transition 15
Figure 4. The roles of EMT in developmental processes including mesodermal lineage formation and neural crest differentiation. 16
Figure 5. Hierarchical organization of chromatin and structure of the nucleosome core particle. 18
Figure 6. Schematic representation of histone variants with their corresponding roles 19
Figure 7. H3 histone variants and their roles on chromatin organization with regarding chaperons. 20
Figure 8. Sequence alignment of human histone H3 variants which represents amino acid differences among human H3 variants compared to H3.3 as the reference (Szenker et.al.2011) 20
Figure 9. Schematic overview of experimental design for investigating the role of histone variant H3.3 in epigenetic regulation of EMT by siRNA based H3.3 Knockdown 23
Figure 10. Schematic overview of experimental design of EMT by TGFβ3 induction 24
Figure 11. Flow chart of neuronal differentiation protocol followed from mESCs to CAs, neural progenitor cells and mature neurons. 24
Figure 12. Cloning, expression, and purification of recombinant mouse LIF. 26
Figure 13 Comparative analysis of EMT induction across three different cell models as MCF10A cells (non-tumorigenic human mammary epithelial) cells, NMuMG (normal murine mammary gland epithelial) cells, B6Blu (mouse embryonic stem cells). 34
Figure 14. Gene expression analysis of EMT markers of different cell and EMT models MCF10A, NMuMG, and mESCs. 36
Figure 15. H3f3a knockdown in NMuMG cells does not induce significant changes. 37
Figure 16. Different siRNAs targeting H3.3A produce variable effects on cell morphology and CDH1 expression. 38
Figure 17. siRNA target regions and expression of H3.3A splice variants. 40
Figure 18. H3.3A knockdown and TGFβ3 treatment induce similar morphological changes. 41
Figure 19. Depletion of H3.3A induces an EMT-like transcriptional profile similar to TGFβ3 induced EMT. 42
Figure 20. H3.3A Knockdown and TGFβ3 Treatment Induce N-cadherin Upregulation on Protein Level 43
Figure 21. Heterogeneity in MCF10A Cells Reveals Diverse Responses to TGF-β3 Treatment. 44
Figure 22. MCF10A Heterogeneity Persists Following Multiple E-Cadherin Sorting. 45
Figure 23. MCF10A Heterogeneity Persists on Transcriptional Level confirmed by qPCRs and Immunostaining. 46
Figure 24. Schematic representation of sorting strategy and the experimental design for clonal expansion of single cell derived populations 47

Figure 25. Representative images of clonal growth patterns depicting epithelial and mesenchymal phenotypes for A) CDH $^{(++)}$ and B) CDH $^{(--)}$ single-cell derived MCF10A Clones. 48
Figure 26. Clonality and E-Cadherin levels of single cell clones. 49
Figure 27. Single-Cell Derived MCF10A Clones Undergoing EMT Exhibit Persistent Transcriptional Heterogeneity. 49
Figure 28. MCF10A Cells Show Persistent Heterogeneity After Clonal Expansion of Cells. 50
Figure 29. The effect of Fsk treatment on TGFβ3-mediated EMT in MCF10A cells, exploring changes in cellular behaviour and phenotype. 52
Figure 30. The effect of Fsk treatment on transcriptional and protein level for TGFβ3 mediated EMT in MCF10A cells, exploring changes by qPCR and western blots. ..53
Figure 31. Comprehensive Analysis of EpCAM Expression, EMT Marker Associations, and Cellular Heterogeneity in MCF10A Cells under Fsk Treatment...54
Figure 32. EpCAM Expression Highlights the Presence of Distinct Subpopulations Within the MCF10A Population. 56
Figure 33. Combined CDH1 and EpCAM Sorting Provides Higher Resolution on Landscape of Cellular Heterogeneity in MCF10A Cells. 57
Figure 34. DNA Content Analysis Reveals No Significant Differences in Cell Cycle Distribution Related to Forskolin Treatment. 58
Figure 35. Proliferation and DNA damage analysis of Fsk $^{(+)}$ and Fsk $^{(-)}$ cells with and without TGFβ3 treatment. 59
Figure 36. Transcriptomic profiling of parental and TGFβ3-treated MCF10A cells..60
Figure 37. Transcriptomic alterations upon H3.3A knockdown and comparison with TGFβ3-induced EMT. 61
Figure 38. Gene Set Enrichment Analysis (GSEA) reveals distinct pathway enrichment profiles following H3.3A knockdown and TGFβ3 treatment. 63
Figure 39. siRNAs mediated knockdown of HIRA reveals variable effects on EMT-associated phenotypes. 64
Figure 40. Immunofluorescence staining of E-Cadherin and actin stress fibers (phalloidin) in MCF10A cells for vehicle and cells with HIRA knockdown using si07 or si10. Nuclei were counterstained with DAPI and images were acquired using confocal microscope. 65
Figure 41. HIRA depletion induces EMT-like transcriptional reprogramming. 66
Figure 42. H3.3A depletion impairs G1/S transition and alters cell cycle progression. 67
Figure 43. Effects of H3.3A and HIRA knockdown on cell proliferation. 68
Figure 44. A) Schematic representation of the ChIP-qPCR workflow following HIRA knockdown and pulldown by IgG, H3.3 and ELF3 enrichment. B) Agarose gel confirming mononucleosome enrichment of chromatin that was digested using micrococcal nuclease. C-F) qPCRs showing enrichment at the transcription start site (+1) and upstream regulatory region (−1) of CDH1 and GRHL3 genes. 69

IV. ACKNOWLEDGEMENTS

First and foremost, I would like to express my sincere gratitude to my supervisor, Dr. Hani Alotaibi, and the members of his lab for their support throughout my PhD. I also extend my deep thanks to Prof. Stefan Dimitrov, who played a pivotal role in my academic journey from guiding me through my PhD to generously guiding me through the postdoc application process, even rehearsing interviews with me. Working in their labs during my PhD was an incredibly enriching experience.

I gratefully acknowledge TÜBİTAK and TUSEB for funding my work through the following grants: 118C354, 122N046, and 122Z886. I would also like to thank TUBİTAK 2211-A and 2250 programs for supporting me throughout my PhD studies. I would also like to thank the IBG core facilities, especially the Flow Cytometry and Microscopy units for their continuous technical support throughout my research.

I owe my deepest gratitude to Dr. Imtiaz Nisar Lone. I feel incredibly lucky to have worked with him on many projects, and I will always carry his influence with me. His guidance in the lab, his calm and thoughtful approach to every challenge, and his constant support, both scientifically and personally have meant the world to me. Imtiaz was always the one we could rely on, especially in times when things were uncertain or difficult. His kindness, patience, and generosity have left a lasting impact on me. I also thank Dr. Kasım Diril for his collaboration on these projects.

A very special thank you goes to Şeyma, my close collaborator and friend. We worked side by side through every step of our thesis works, building a partnership that made even the most intense days manageable and meaningful.

I would like to express sincere gratitude to Tuğçe Batur who joined us later but quickly became a central part of our team. Her support and dedication made our heterogeneity paper possible. I also want to acknowledge her student Ece and express my best wishes for her future.

My heartfelt thanks to Abed, with whom I shared many long experiments, troubleshooting, analysing, discussing ideas, and sharing both the frustrations and joys of research. He is a cherished friend and co-author, whose work ethic, companionship and friendship I deeply admire.

I’m thankful to Esra and Ceren, my very first lab mates, who made the beginning of this journey unforgettable. Together with Imtiaz, we were a tight-knit team in science, COVID, and life with great excitement and care. Also, I want to thank Tuğba who brought joy and energy to the lab with her endless enthusiasm.

Finally, I’m grateful to Gkamze, who were one of the brightest, most competent, and most wholehearted people I have ever met. Our long days and nights in the lab, and the friendship we shared and the most treasured memories. Her presence kept me grounded through many challenging moments.

I am deeply grateful to my family for their unwavering support and love throughout this journey. To my mother for being my role model with her love, care, discipline and principles. I owe much of my ability to stay practical, efficient, and quick on my feet especially during chaotic lab days. Her strength, love, and endless sacrifices have carried me through every step of this journey. To my father who sparked my curiosity in science, introduced me to the world of popular science as a kid and encouraging me to explore. Their guidance shaped both who I am and what I do today. To my sister, my very first title in life was being her sister, and I wear that title with love and joy. Her ever-present smile, and her ability to make every moment lighter have always been a source of strength for all of us. She also has contributed to my academic life in your unique, artistic way. I am deeply grateful to my husband, Emre, the most supportive partner any PhD student could ever wish for. From long lab nights to the dreams I carry for the future, he has been beside me every step of the way even willing to make sacrifices to support my academic path. He has been my constant source of calm, strength, and stability with always ready with a quiet hug, a cup of tea to calm me down, a late-night walk to clear my head, or simply sitting next to me in silence until he makes me laugh again. I am endlessly grateful for his love, patience, and belief in me. I would also like to thank his family for their understanding and kindness throughout this journey. I can’t imagine this journey without my family. They always supported me in ways both visible and silent.

Lastly, I thank every member of my family and friends, close or distant, for listening to my endless stories about science.

EPIGENETIC REGULATION OF EPITHELIAL TO MESENCHYMAL TRANSITION (EMT) BY HISTONE VARIANT H3.3

Esin Şekeroğlu, Dokuz Eylül University Izmir International Biomedicine and Genome Institute, 35340, Izmir / TURKEY

ABSTRACT

Epithelial to mesenchymal transition (EMT) is a fundamental biological process in which epithelial cells lose their polarity and cell-cell adhesion properties and acquires mesenchymal traits such as increased motility and invasiveness. EMT plays essential roles in biological processes such as embryonic development, wound healing, embryonic stem cell differentiation and proliferation. In addition to its regulatory functions, it is also significantly associated with pathological contexts including tumour progression, metastasis, and resistance to apoptosis and chemotherapy. The transcriptional regulation of EMT has been well characterised. However, current knowledge on its epigenetic control, especially the contribution of histone variants remains limited.

Recent publications showed that the depletion of histone variant H2A.Z downregulated epithelial and upregulated mesenchymal markers resulting in an EMT-like phenotype. Histone variant H3.3 is a key epigenetic regulator with important roles in cell maintenance, chromatin remodelling, gene expression and genome integrity. Mutations and mis-regulation of H3.3 have been identified as associated with cancers. With the overlapping functions of H2A.Z on control of nuclear homeostasis, gene expression and mitosis, we hypothesised that histone variant H3.3 might have significant implications on EMT.

Considering these, we aim to provide an understanding of the epigenetic regulation of EMT by the histone variant H3.3 by comparison in 3 different cell models, TGFβ induced EMT of MCF10A and NMuMG cells and neuronal differentiation of mouse embryonic stem cell B6Blu. We employed siRNA mediated H3.3A knockdown to understand its direct role in the regulation of EMT with detailed analysis of model systems through EMT and H3.3A depletion processes.

Taken together, our findings present novel insight into the regulation of epithelial to mesenchymal transition by histone variant H3.3A in a context dependant manner as its knockdown induced EMT-like phenotype and altered the expression of key epithelial and mesenchymal markers in a context dependant manner.

Keywords: EMT, Histone Variants, H3.3, Transcriptional Networks, Heterogeneity

EPİTELYALDEN MEZENKİMALE GEÇİŞİN H3.3 HİSTON VARYANTI İLE EPİGENETİK REGÜLASYONU

Esin Şekeroğlu, İzmir Uluslararası Biyotıp ve Genom Enstitüsü, Dokuz Eylül Üniversitesi, 35340. İzmir, Türkiye.

ÖZET

Epitelden mezenkimale geçiş (EMT), epitel hücrelerin polaritelerini ve hücre-hücre yapışma özelliklerini kaybederek artmış hareketlilik ve invazivlik gibi mezenkimal özellikler kazandığı temel bir biyolojik süreçtir. EMT, embriyonik gelişim, yara iyileşmesi, embriyonik kök hücre farklılaşması ve proliferasyonu gibi çeşitli biyolojik süreçlerde önemli roller üstlenmektedir. Ayrıca, tümör progresyonu, metastaz, apoptoz direnci, kemoterapiye direnç gibi patolojik süreçlerle de ilişkilidir.

EMT'nin transkripsiyonel düzeydeki düzenlenmesi iyi tanımlanmış olmasına rağmen, epigenetik kontrol mekanizmaları ve özellikle histon varyantlarının katkısı konusunda mevcut bilgiler oldukça sınırlıdır. Son çalışmalar, histon varyantı H2A.Z'nin yokluğunun epitel belirteçlerini baskılarken mezenkimalleri artırdığını ve bunun sonucunda EMT-benzeri bir fenotip ortaya çıktığını göstermiştir. Histon varyantı H3.3, hücre korunumu, kromatin yeniden düzenlenmesi, gen ekspresyonu ve genom bütünlüğü gibi süreçlerde kilit rol oynayan önemli bir epigenetik düzenleyicidir. H3.3'ün mutasyonları ve yanlış düzenlenmesi, kanserle ilişkili olarak tanımlanmıştır. H2A.Z'nin nükleer homeostaz, gen ekspresyonu ve mitoz üzerindeki H3.3 histon varyantı ile örtüşen işlevleri göz önünde bulundurulduğunda, H3.3 histon varyantının EMT üzerinde önemli etkileri olabileceği hipotezi öne sürülmüştür.

Bu doğrultuda, epitelden mezenkimal geçişin H3.3 histon varyantı tarafından epigenetik olarak nasıl düzenlendiğinin anlaşılması hedeflenmiştir. Bu amaçla, üç farklı hücre modelinde; MCF10A ve NMuMG hücrelerinde TGFβ ile indüklenen EMT süreci ve B6Blu fare embriyonik kök hücrelerinde nöronal farklılaşma, karşılaştırmalı analizler gerçekleştirilmiştir. EMT'nin düzenlenmesindeki doğrudan rolünü ortaya koymak için H3.3A genine karşı siRNA aracılı susturma uygulanmış ve model sistemlerde EMT ve H3.3A yokluğu süreçleri detaylı bir şekilde analiz edilmiştir.

Sonuç olarak, bulgularımız histon varyantı H3.3A'nın EMT'nin düzenlenmesinde rol oynadığına dair yeni bir bakış açısı sunmaktadır. H3.3A'nın baskılanması bağlama bağlı şekilde EMT-benzeri bir fenotipin oluşmasına ve temel epitel ile mezenkimal belirteçlerin ifadesinin değişmesine yol açmıştır.

Anahtar Kelimeler: EMT, Histone Variantları, H3.3, Transkripsiyonel Ağlar, Heterojenite

1. INTRODUCTION AND AIM

1.1. Aim of Study

We aim to investigate the role of H3.3 on the epigenetic regulation of EMT of cell lines from different species and characteristics; MCF10A, a non-malignant human mammary gland cells, NMuMG, normal murine mammary gland epithelial cells and mouse embryonic stem cells to address fundamental questions in epigenetics using non-malignant and normal cell lines.

1.2. Hypothesis of The Study

EMT is an important process in which epithelial cells lose their polarity, cell-cell junctions and gains mesenchymal properties like increased motility, invasiveness and morphological changes [1-3].

It has important roles in many biological processes such as embryonic development, wound healing, embryonic stem cells differentiation and proliferation [4]. Apart from its normal biological function, EMT and its regulation by transcription factors has significant importance in cancer because of the cells acquired migratory and invasive characteristics, roles in tumour progression, resistance to apoptosis and chemotherapy [5].

Histone variants are nonallelic isoforms of canonical histones that are expressed during all stages of cell cycle unlike canonical histones that are only expressed during S-phase. With important functions in biological processes such as nuclear homeostasis, gene expression, and mitosis, mutations in histone variant H3.3 found to be associated with several cancer types.

Recent publications showed that the depletion of histone variants such as H2A.Z resulted in an EMT-like phenotype as downregulated epithelial and upregulated mesenchymal markers. It is known that H2A.Z has essential roles in the formation of mesoderm and neural crest which is critically dependent on the EMT process [6, 7]. With the overlapping functions with H2A.Z, we hypothesized that histone variant H3.3 would significantly affect EMT [7, 8].

In this study, we expect to see an EMT-like phenotype by the knockdown of histone variant H3.3 by RNA interference in MCF10A and NMuMG cell lines. In these cells, morphological changes and expression levels of widely accepted EMT markers of transcriptional regulation mechanisms controlling the EMT program will be examined. Therefore, we aim to provide an understanding of the epigenetic regulation of EMT by histone variant H3.3, to address fundamental questions in epigenetics.

2. GENERAL INFORMATION

2.1. Epithelial to Mesenchymal Transition

Epithelial to Mesenchymal Transition

Epithelial-to-mesenchymal transition (EMT) is a highly dynamic and tightly regulated biological process in which epithelial cells lose their epithelial features such as apico-basal polarity and intercellular junctions and gains mesenchymal characteristics including enhanced motility, invasiveness, and cytoskeletal and morphological remodelling [9, 10].

Importantly, EMT is considered as a spectrum including partial/ hybrid states which exhibits both epithelial and mesenchymal properties. This phenotypic plasticity creates advantage for cancer cells in metastasis, stemness and therapy and apoptosis resistance by dynamically switching between epithelial and mesenchymal traits [1, 5, 11-14].

EMT is driven by tightly regulated transcriptional reprogramming regulated by key EMT-inducing transcription factors involved in cell adhesion, cytoskeleton remodelling and motility such as SNAI1/2, TWIST1/2, and ZEB1/2 [10, 12, 15],

EMT is a complex process that requires high levels of plasticity and orchestrated by transcriptional reprogramming including regulation of two members of cadherin superfamily, downregulation of E-Cadherin (CDH1) and upregulation of N-Cadherin (CDH2) markers, known as cadherin switch [12, 13]. The cadherin switch is a major process during EMT. CDH1 and CDH2 are calcium-dependent transmembrane adhesion proteins and two of the major proteins that regulates dynamic cell-cell interactions, including tight junctions (TJs), adherent junctions [12, 15, 16]. It is noted that cells undergoing partial EMT often express CDH1 and CDH2 simultaneously highlighting their hybrid identity and enhanced plasticity [13, 14].

2.2. Signalling Pathways and Transcriptional Networks on Regulation of EMT

Among various EMT inducing agents, transforming growth factor β3 (TGFβ3) is one of the major and most used inducers of EMT through several signalling pathways with key roles in proliferation, cell homeostasis, differentiation, cell adhesion and extracellular matrix organization [17, 18].

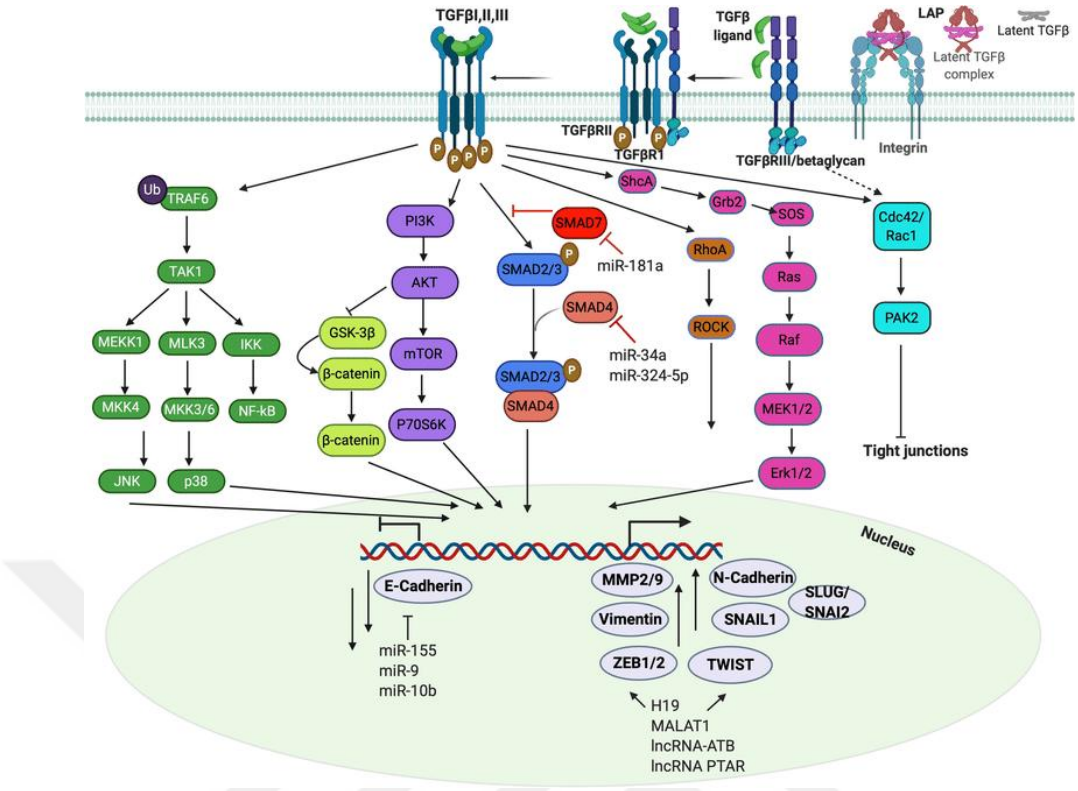

Figure 1. TGFβ Signalling Pathways in EMT Regulation.
The diagram illustrates key TGFβ signalling mechanisms involved in epithelial to mesenchymal transition through canonical SMAD-dependent signalling and non-canonical cascades such as PI3K/AKTand MAPK to orchestrate EMT-related transcription regulatory networks (Kumari, R. & Jat, P. (2021))

Table 1. Gene list

ABCC3	B3GNT3	CLDN7	EPS8L2	GPR56	KRT19	MXRA7	PYCARD	SLC9A3R1	TGFB1I1	TSPAN15
ADAP1	BAG2	CNKSR1	ERBB2	GPX2	KRT7	MYH14	RAB11FIP1	SLPI	TGFB2	TTC39A
AGR2	BIK	COL5A2	ERBB3	GRB7	KRT8	MYL9	RAB20	SMAD4	TGFB3	TUBA1A
AIM1	BLNK	COMT	ERMP1	GRHL2	LAD1	MYO1D	RAB25	SMAD5	TGFBR1	TUBB6
AKAP12	BSPRY	CTSH	ESRP1	GRHL3	LCN2	MYO5C	RABGAP1L	SMAD9	TGFBR2	TWIST1
ALDH3B2	CALD1	CYB561	ESRP2	HES1	LEPRE1	MYO6	RBM47	SNAI1	TGFBR3	TWIST2
ALOX5	CAMK2N1	CYP4F3	ETV1	HNMT	LGALS1	OAS1	RECK	SNAI2	TJP1	UGT1A1
ANK2	CAPN1	DDR1	EVPL	HPGD	LHFP	OCLN	RHOD	SOAT1	TJP2	VAMP8
ANK3	CBLC	DENND2D	EXPH5	ICA1	LLGL2	OR7E14P	S100A14	SOBP	TMC6	VGLL1
ANXA4	CD46	DENND5A	F11R	IL1RN	LOXL2	OVOL2	S100P	SORL1	TMEFF1	VIM
ANXA9	CD9	DSC2	FA2H	IL20RA	LSR	PERP	SACS	SPARC	TMEM158	XBP1
AP1M2	CDH1	DSP	FBP1	IRF6	LY75	PKP3	SCEL	SPINT1	TMEM30B	ZEB1
AP1S2	CDH2	DTX4	FERMT2	ITGA5	MALL	PLS1	SCNN1A	SPINT2	TMPRSS2	ZEB2
AQP3	CDH3	EHF	FHL1	ITGB4	MANSC1	PLXNB2	SDC1	SRPX	TMPRSS4	ZNF165
ARAP2	CDS1	ELF3	FN1	ITGB6	MAP1B	PMP22	SERINC5	SSH3	TNFSF13	CEBPA
AREG	CEACAM1	ELF5	FOXA1	JUP	MAP7	POF1B	SERPINE1	ST14	TOB1	HNF4A
ARHGAP8	CEACAM6	ELMO3	FSTL1	KCNK1	MAPK13	POPDC3	SFN	STAP2	TOX3	
ARHGDIB	CEP170	EMP3	FXYD3	KDELC1	MGST2	PPFIBP2	SH2B3	SYNGR2	TPM2	
ARHGEF5	CHN1	EPCAM	GALNT3	KLF5	MPZL2	PPL	SH2D3A	TACSTD2	TRIM31	
ATP1B1	CKMT1A	EPHA1	GFPT2	KLK6	MSN	PRSS8	SH3YL1	TCF4	TRPC1	
ATP2C2	CLDN1	EPN3	GJA1	KRT15	MST1R	PTK6	SHANK2	TGFA	TSPAN1	
AXL	CLDN4	EPS8L1	GLYR1	KRT18	MTUS1	PTRF	SLC37A1	TGFB1	TSPAN13	

TGFβ signalling pathway initiates a well-orchestrated and tightly regulated cascade of EMT associated reprogramming (Figure 1). Upon binding of TGFβ ligands (TGFβ1, TGFβ2, TGFβ3) to the receptor complex (TGFβR1/ TGFβR2), SMAD proteins get activated by phosphorylation and form SMAD complex which further translocate into nucleus where the transcriptional regulation of EMT associated genes happens in cooperation with chromatin remodelers and other transcription factors [15, 19, 20].

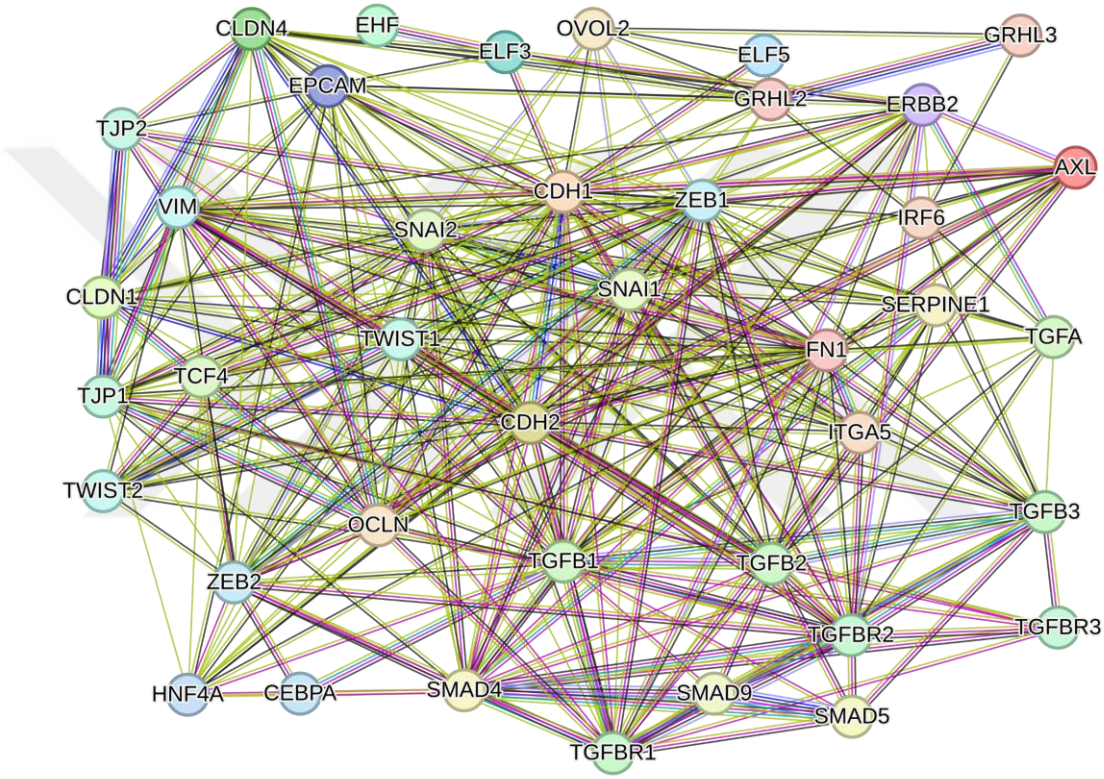

Figure 2. Protein interaction network of EMT-related genes.
A STRING network was generated to illustrate the complexity of EMT and predicted protein-protein interactions including key regulatory proteins of EMT showing highly connected nodes between TGFβ and commonly used EMT markers such as CDH1, ZEB1, VIM, SNAI1 and SNAI2. The EMT gene list used for the analysis is provided in **Table 1**.

This phenomenon induces key EMT transcription factors such as ZEB1, ZEB2, SNAI1, SNAI2 further resulting in the downregulation of epithelial markers such as CDH1, OCLN, GRHL3 and ELF3 and upregulation of mesenchymal markers including VIM, FN1 followed by phenotypic changes of actin reorganization, loss of adherent junctions and increased migration[10, 21] (Figure 2).

The gain of mesenchymal markers along with retaining epithelial characteristics rather than complete loss of epithelial identity refers to a hybrid or partial EMT state [10].

2.3. Epithelial to Mesenchymal Transition in Physiological and Pathological Contexts

Considering its distinct roles, EMT can be classified into three sub types [5]. The EMT which is associated with embryogenesis and mesoderm formation is Type I-EMT while Type II-EMT is associated with wound healing and tissue regeneration. Finally, Type III-EMT is related with cancer related processes such as tumour progression and metastasis (Figure 3).

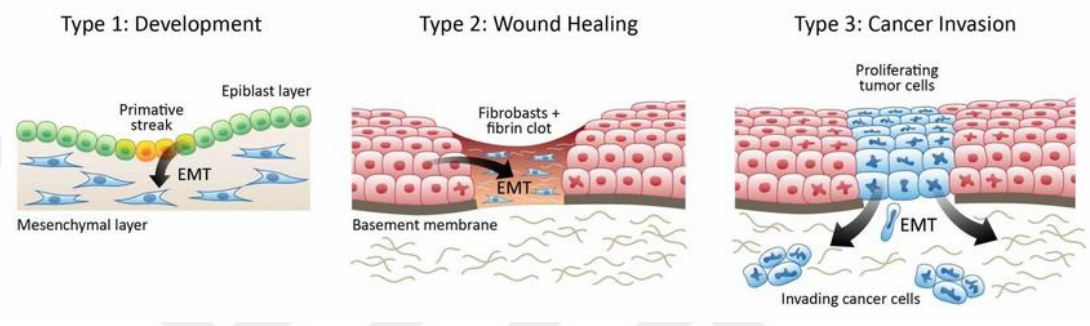

Figure 3. Three types of epithelial to mesenchymal transition
Type 1 EMT occurs during embryonic development, enabling mesoderm and neural crest formation. Type 2 EMT is activated during wound healing and tissue regeneration. Type 3 EMT is associated with cancer progression, facilitating tumour cell invasion and metastasis (Scanlon 2014).

Apart from its roles in metastasis and tissue modelling, EMT has important functions in early embryonic development regarding differentiation of pluripotent stem cells into lineage specific progenitors. Although this process differs from canonical process most significantly including CDH1, CDH2 and Vimentin [22].

Type 1 EMT regulates key developmental events such as implantation of embryo, gastrulation and neural crest formation which is tightly linked to conserved signalling pathways including Wnt and TGFβ cascades and consecutively transcriptional regulators of SNAI, ZEB, TWIST and Sox families and downstream proteins such as Nodal and Vg1 [22-24]. Briefly epithelial cells undergo EMT and migrate to form mesenchymal layer through primitive streak. Type 2 EMT on the other hand, is responsible in wound healing and tissue regeneration by contributing to tissue integrity by migrating to the wounded region [24].

Among these, Type 3 is the most studied EMT type with direct links to tumour progression, metastasis and chemotherapy resistance [9]. Its regulation is orchestrated by several transcription factors including Snail 1/2, ZEB1/2, and TWIST1/2 to promote mesenchymal state and inhibiting epithelial gene patterns

resulting in characteristic features of decreased cell-cell adhesion, increased migratory functions, resistance to apoptosis [25-27] (Figure 4).

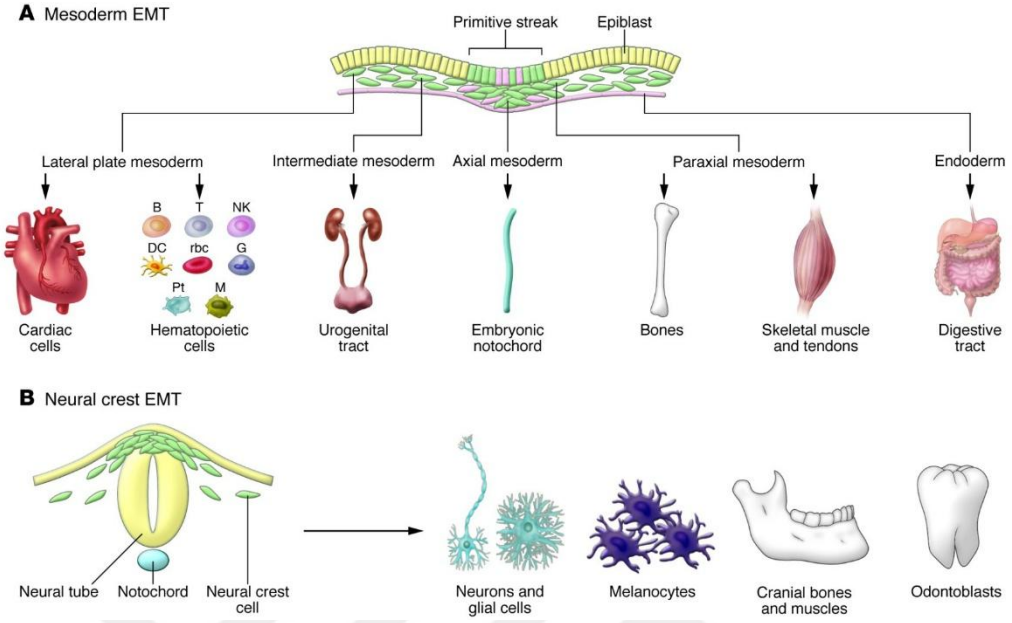

Figure 4. The roles of EMT in developmental processes including mesodermal lineage formation and neural crest differentiation.
A) EMT works in mesodermal lineage formation from lateral, intermediate, paraxial axial mesoderm along with endoderm. B) Neural crest cell differentiation into neurons, glial cells, melanocytes, craniofacial bones and muscles and odontoblasts through EMT reprogramming that enables migration. (Acloque, 2009)

2.4. Human, Murine, and Pluripotent Cell Lines as Model Systems for EMT Studies

EMT responsiveness to EMT inducing signals differs significantly on the cellular context as epithelial cells exhibit distinct and complex baseline characteristics compared to cancer cell lines that effect EMT progression [28, 29].

MCF10A cell line is an immortalised non-tumorigenic human breast epithelial cell line which is known by benign proliferative features of the derived tissue and its lack of oestrogen receptor [30, 31]) and is commonly used for EMT studies with their homogenous epithelial characteristics, and high plasticity.

NMuMG cells are non-transformed mouse mammary gland cells that is used as a suitable model for EMT response to TGFβ with a strong morphological transition [32, 33].

Embryonic stem cells (ESCs) are characterised by high capacity of pluripotency and self-renewal which allows them to differentiate into all somatic cell types [34]. This differentiation from pluripotent cells to lineage development is tightly regulated during early development. Epithelial to mesenchymal transition, although is

canonically associated with mesoderm and neural crest formation, recent research showed that EMT-like and partial EMT processes have important regulatory roles in pluripotency and neuroectoderm differentiation in embryonic stem cells [35]. This dynamic remodelling of cellular identity is particularly effective during early phases of neural induction via loss of epithelial characteristics such as apical-basal polarity and cell-cell adhesion [36].

2.5. Chromatin organization and Histone proteins

Eukaryotic cells contain approximately 2 meters of DNA within a nucleus just around 6 μm in diameter in an ordered fashion. This highly sophisticated compaction is achieved by important hierarchical folding of DNA around histones and orchestrated via interactions with histones and small regulatory proteins [37]. This higher order structure of chromatin starts with nucleosome which is the fundamental repeating unit consists of 147 base pairs long DNA wrapped around histone octamer by 1.7 turns [38, 39] (Figure 5). Histone octamer consists of 2 of each histone proteins as dimers of H2A-H2B and H3-H4.

Chromatin has transcriptionally active gene rich domains and inactive domains enriched near nuclear periphery both with different roles in DNA repair, gene expression regulation and cellular homeostasis [40-42]. Several models emphasised the dynamic and context-dependent nature of chromatin folding, which allows for rapid reorganization in response to developmental or environmental stimuli [43-46]. This dynamic organization is regulated by protein-protein and protein-DNA interactions, transcription factors as well as posttranslational modifications such as histone methylation and acetylation, together forming three dimensional chromatin folding [47, 48]. Three dimensional chromatin loops are regulated within these active and repressive domains by lineage specific transcription factors [47, 49]. It is also important to note that histone methylations including H3K4me3, H3K27me3, H3K9me3 and histone acetylation such as H3K27ac dynamically regulates these regulatory regions to stimulate silencing or activation of lineage specific processes [50].

Histone variants are non-allelic isoforms of canonical histones that is expressed in a DNA replication independent manner compared to their canonical counterparts [51]. They are mostly coded by single genes located outside of genomic clusters of canonical histones that includes multiple intronless genes incorporating

into chromatin, allowing them to respond dynamically to various physiological and developmental processes [52-55].

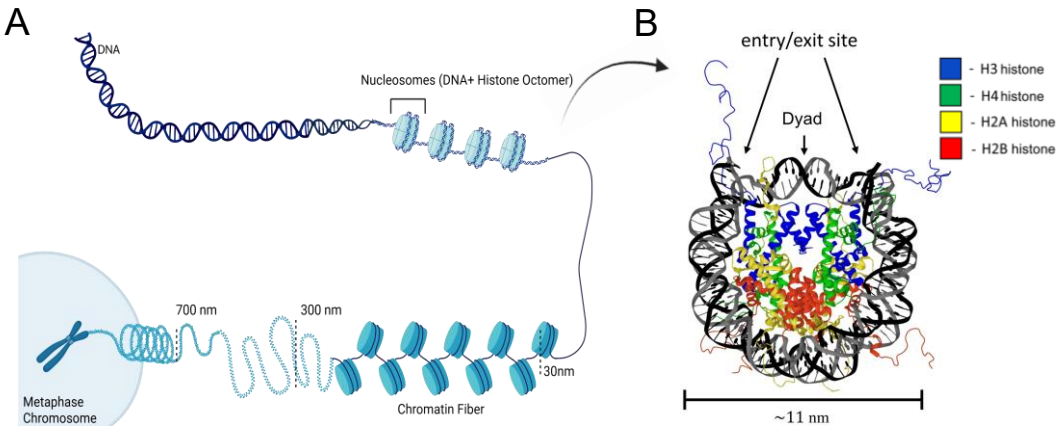

Figure 5. Hierarchical organization of chromatin and structure of the nucleosome core particle. A) Chromatin undergoes multiple levels of compaction, beginning with DNA wrapping around histone octamers to form nucleosomes further compacted to beads-on-a-string structures (approx. 11 nm in diameter) followed by higher-order 30 nm fibers, finally forming the 300 nm and 700 nm loops observed in a condensed metaphase chromosome. B) Structural organization of the nucleosome core particle composed of DNA wrapped around a histone octamer consists of two each of H2A, H2B, H3, and H4 histones. (Unkraintsev et.al.2024)

To date, there are many histone variants that has been identified with distinct roles in transcription, replication, chromosome segregation and DNA repair [56]. Among those, histone H2A has the most abundant number of identified variants with 17 variants with highest sequence differences compared to other histone variants including H2AZ-1, H2A.Z-2, H2A.X, macroH2A and H2A.B which extensively studied for their role and regulation [51, 57] (Figure 6). Among these, H2AZ has been previously studied through many mechanisms and research showed that its loss causing impaired motility and concurrently deficiencies on mesoderm and neural crest formation in Xenopus laevis [58] and also is lethal at pre-implantation stage of blastocyst in mice embryos [59], suggesting its vital roles during embryonic development. It is also known that it is important for the regulation of chromatin with high enrichment profiles at promoters and enhancers in embryonic stem cells regulating differentiation and pluripotency. Additionally, recent studies showed that

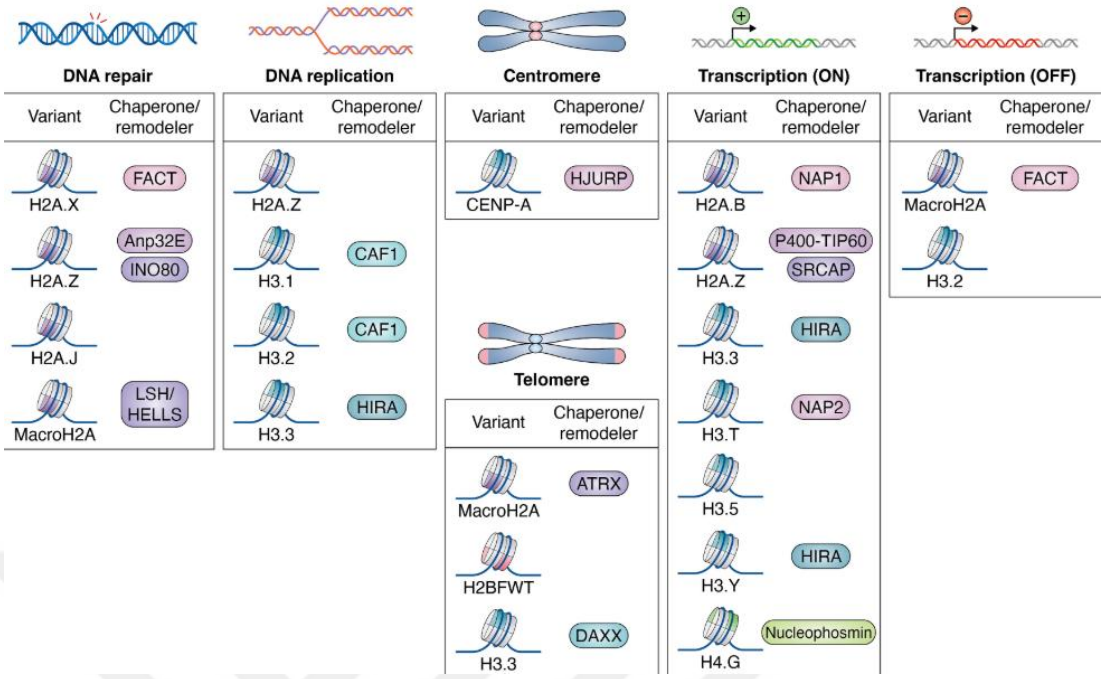

Figure 6. Schematic representation of histone variants with their corresponding roles.

H2AZ is highly associated with EMT as H2AZ depletion found to be linked to higher migration rate, slower proliferation, impaired colony formation and mesenchymal like morphology supported with EMT-like transcriptional profiles [6].

2.6. Histone Variant H3.3 and Its Role in Chromatin Dynamics

Similar to histone H2, numerous H3 variants are also reported including H3.1, H3.2, H3.2, CENP-A, H3.1T, H3.5, H3.X and H3.Y which shows sequence dissimilarities ranging from minor sequence differences to significant structural differences [53, 54]

Histone variant H3.3 is a key epigenetic regulator with important roles in cell maintenance, chromatin remodelling, gene expression and genome integrity. H3.3 is highly enriched at the active domains and regulatory domains such as enhancer and promoters, highlighting its roles at key regulatory regions including maintenance of open chromatin. [55, 60, 61]. As well as being enriched in active domains, H3.3 is incorporated into both heterochromatin and euchromatin regions and also in DNA damage sites in mammals suggesting critical associations in chromatin stability [62].

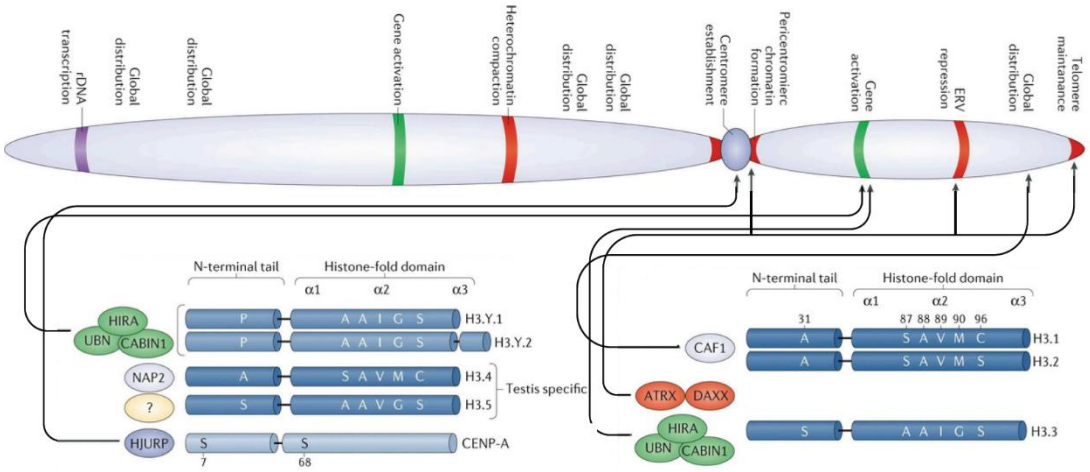

Figure 7. H3 histone variants and their roles on chromatin organization with regarding chaperons. Schematics emphasizing significant roles of histone variant isoforms with sequences and structure differences comparable to canonical counterparts. (Adapted from Martire et.al.2020)

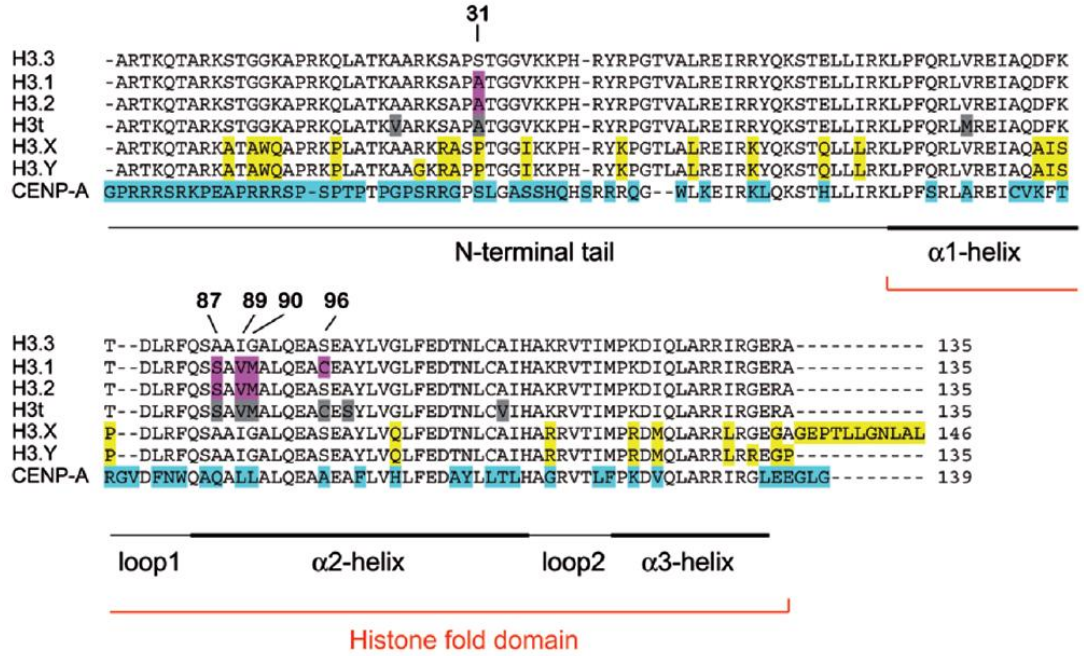

Figure 8. Sequence alignment of human histone H3 variants which represents amino acid differences among human H3 variants compared to H3.3 as the reference (Szenker et.al.2011).

H3.3 has also been found to have important roles in transcriptional regulation similar to H2AZ. They share many common features such as evolutionarily conserved structure and enrichment on promoters and enhancers [61, 63, 64] .

It has high sequence similarities with its canonical H3 histone, and it only differs by 4 amino acids from replication dependent H3.2, five with H3.1 [61, 65]. Although, there are very minor changes, these specific regions result in different functional roles.

H3.3 has two isoforms in several organisms including human and mouse as H3.3A and H3.3B coded by their corresponding genes with differences in their untranslated region translating into same H3.3 protein [61, 66]. HIRA Chaperone in Histone Variant Deposition

HIRA is one of the histone chaperons that is responsible for the deposition of histone variant H3.3 into chromatin in complex with CABIN1 and UBN1 [67]. It is first described in Xenopus egg extracts independent of DNA replication [68, 69] . Further studies confirmed specific interactions of histones including H3.3 with HIRA in human cells [70, 71], functioning as a complex with CABIN1 and UBN1 whose roles in specific recognition and deposition of H3.3 at euchromatic regulatory regions such as promoters and enhancers were confirmed [72]. It is also shown that HIRA is not essential for H3.3 deposition in embryos or adult somatic cells but is required during chromatin condensation in male pronucleus of Drosophila suggesting context dependant deposition pathways [73] . Supporting this, multiple mechanisms is found to be regulating H3.3 deposition is identified such as ATP-dependent chromatin remodelling factor CHD1 [74].

Moreover, it is demonstrated that, HIRA is the leading factor in H3.3 deposition in euchromatic regions orchestrating H3.3 deposition together with CHD1 during DNA damage response and chromatin maintenance, highlighting a complex chaperone network for H3.3 deposition [75]. Additionally, it has been shown that the loss of HIRA results in impaired enrichment of H3.3 in embryonic stem cells resulting in reduced chromatin accessibility at proximity to promoter regions and across gene bodies [76].

3. MATERIALS AND METHODS

3.1. Type of the Study

This study is composed of experimental methods and techniques supported with in-silico analysis.

3.2. Time and Place of the Study

All experiments were performed in laboratories of Izmir Biomedicine and Genome Center between February 2020 and July 2025.

3.3. Population and Samples of the Study

All the research experiments were performed using commercial cell lines from Alotaibi Lab and Dimitrov Lab's inventory and in-silico methods.

3.4. Research Material

Non tumorigenic human breast cell line (MCF10A), normal murine mammary gland cell line (NMuMG/E9) and mouse Embryonic stem cell line B6Blu used in the experiments were commercially obtained from ATCC with catalogue numbers; ATCC® CRL-1636, ATCC® CRL-10317 and ATCC® SCRC-1019, respectively.

3.5. Tools for Data Collection

To investigate the role of H3.3A in EMT, we established a workflow integrating RNA interference-based gene silencing followed by morphological analysis by phase contrast and confocal microscopy, RNA level investigation by qPCR and transcriptomics, protein level analysis by western blotting and investigated chromatin level changes by chromatin immunoprecipitation alongside comprehensive analysis of model cell lines.

3.5.1. Cell Culture

Human non-tumorigenic breast cell line MCF10A cells were cultured in DMEM/F-12, GlutaMAX medium (Gibco, 31331-038) supplemented with 20 ng/ml human epidermal growth factor (hEGF, Thermo Scientific PHG0311), 500 ng/ml hydrocortisone (Sigma, H0888), 1X penicillin/streptomycin (Gibco, 15-140-122), 5 % heat inactivated horse serum (Gibco, 26050-070), and freshly added 0.01 mg/ml insulin and with and without 1 uM Forskolin (Sigma, F3917) and maintained at 37 °C in a 5% CO_2 atmosphere. Cells were passaged every 4 days by detachment by 0.05% trypsin-EDTA (Thermo Fisher Scientific 25300-054) to a density of 500k cells/10 cm

plate while media changed every 48 hours. NMuMG (Clone: E9) cells were cultured in DMEM (Gibco) supplemented with 10% fetal bovine serum (FBS; Gibco) and 1% penicillin/streptomycin (Gibco, 15-140-122) without no further fresh supplementation and maintained at 37°C in an incubator supplied with 10% CO_2.

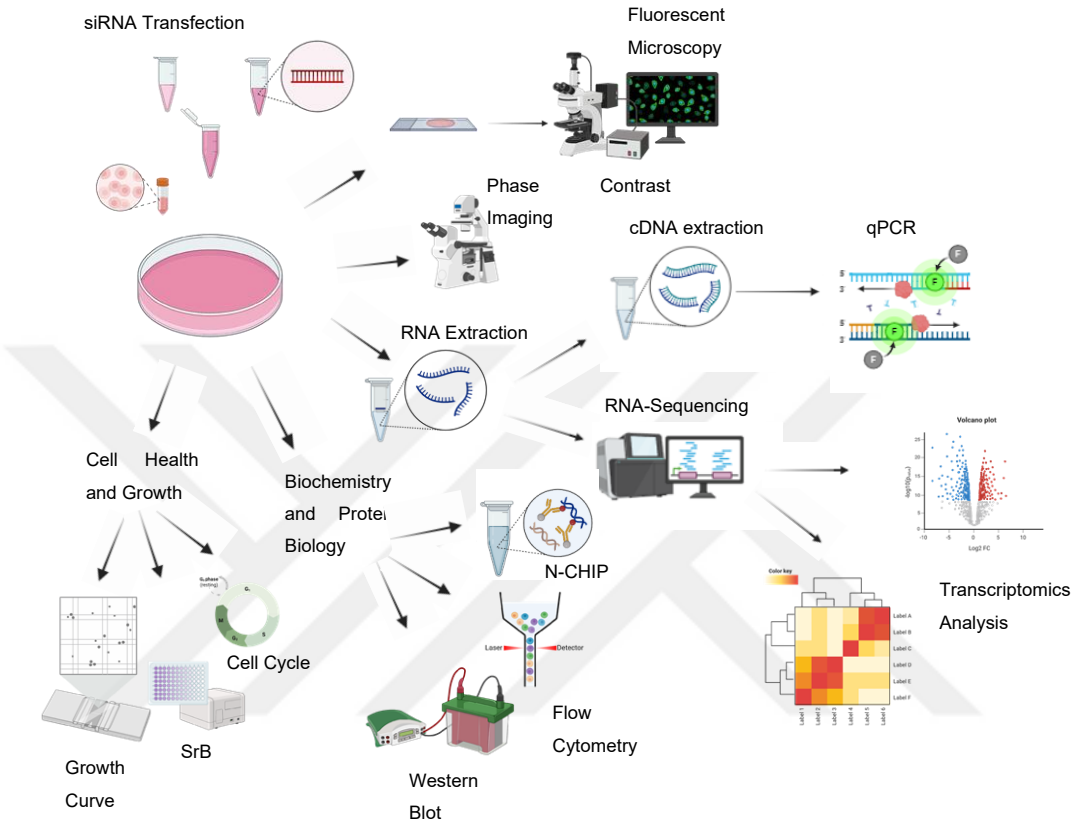

Figure 9. Schematic overview of experimental design for investigating the role of histone variant H3.3 in epigenetic regulation of EMT by siRNA based H3.3 Knockdown

3.5.2. Characterization of MCF10A Cells for EMT Induction by TGFβ3

The time needed for EMT induction by TGFβ3 treatment is optimized for MCF10A cells by treating with 5 ng/ml TGFβ3 for 10 days of time course experiment while media changed every 48 hours. Both Fsk $^{(+)}$ and Fsk $^{(-)}$ cells were treated with TGFβ3 (5 ng/ml) for 4 days or 10 days. While Fsk $^{(+)}$ cells were used in H3.3A knockdown related experiments. NMuMG cells are induced by 2.5 ng/ml according to optimized protocol by our group.

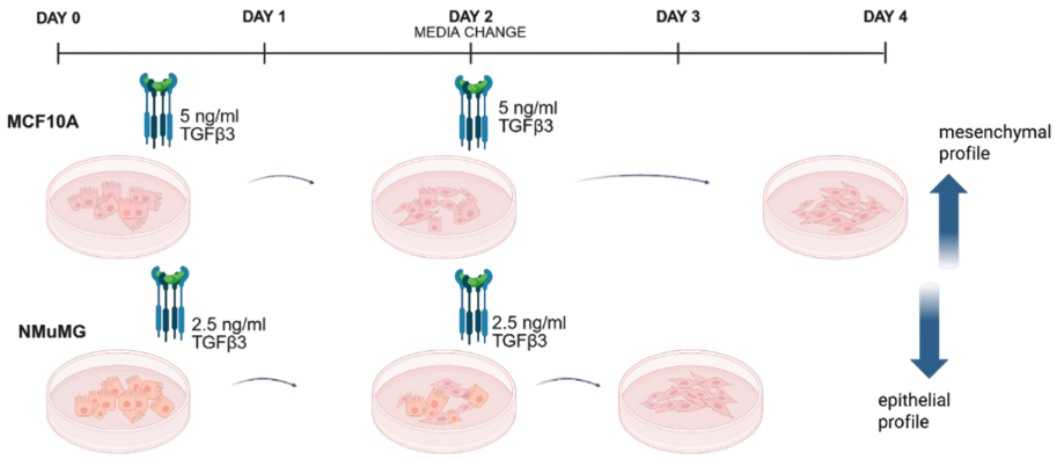

Figure 10. Schematic overview of experimental design of EMT by TGFβ3 induction

3.5.3. Neuronal Differentiation of mESCs as a Developmental EMT Model

Mouse ESCs (B6Blu) were differentiated into neurons according to protocol described by Bibel et al.,2007 [77]. Briefly, mESCs were cultured on mouse embryonic fibroblasts (MEFs) in ES cell media containing DMEM-High Glucose (# 41965039), 15% FBS (FBS, Gibco, #10500064). 1 × NEAA (Thermo Fisher Scientific, #11140035), 55-μM 2-Mercaptoethanol (Sigma-Aldrich, #M3148), 1 × sodium pyruvate (Panbio, #43100), 1 × Pen-Strep (Thermo Fisher Scientific, 15-140-122). For maintenance of pluripotency, media is supplemented with 40 ng/mL HM-LIF for three passages on MEF.

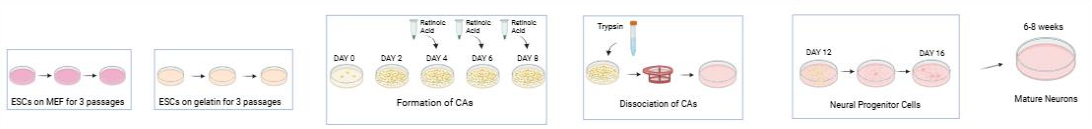

Figure 11. Flow chart of neuronal differentiation protocol followed from mESCs to CAs, neural progenitor cells and mature neurons.

Differentiation was induced by differentiation media containing DMEM-High Glucose (# 41965039), 10% fetal bovine serum (FBS, Gibco, #10500064), 1X sodium pyruvate (Panbio, #43100), 1X NEAA solution (Thermo Fisher Scientific, #11140035), 1X penicillin–streptomycin (Thermo Fisher Scientific, 15-140-122), and 110 μM 2-Mercaptoethanol (Sigma-Aldrich, #M3148)) and cultured in low adhesion plates (Griener Bacteriological Petri Dish, #633102) to promote embryoid body formation. Later, embryoid bodies were further cultured for another four days in the presence of retinoic acid retinoic acid (5 μM). On day 8, the embryoid bodies were dissociated

using trypsin and plated in Poly-d-lysine hydrobromide (Sigma-Aldrich, #P8638) and laminin (Roche, #11243217001)-precoated plates to support neuronal attachment in N2 medium (DMEMHigh Glucose (#41965-039) and DMEM F-12 (#31330038) medium at 1:1 ratio supplemented with 1X N2 supplement (#17502-001), 1X sodium pyruvate (#Panbio 43100), 0.0025% BSA, 1% Pen-Strep (#15140-122)). Medium was refreshed every 24h starting with initial 2h change. Two days post-plating, culture was changed to complete medium containing DMEM-High Glucose (#41965- 039) and Neurobasal medium (#21103049) at 1:1 ratio supplemented with 1X N2 supplement

Table 2. Primers used for qPCR for analysis of neuronal differentiation of mESCs.

Target Gene	Reagent	Forward 5' to 3'	Length	Reverse 5' to 3'	Length	Expected Fragment Size (bp)
OCT 4	SybrGreen	TCTTTCCCCAGGCCCCCGGCTC	22	TGCGGGCGGACATGGGGAGATCC	23	223
SOX-2		CGCGGCGGAAAACCAAGACG	20	GCCGGCGCCCACCCCAACC	19	110
NANOG		CCTTCCCTCGCCATCACACT	20	AGAGGAAGGGCGAGGAGAGG	20	194
MAP2		GCCAGCCTCGGAACAAACA	19	GCTCAGCGAATGAGGAAGGA	20	101
DCX		ATGCAGTTGTCCCTCCATTC	20	ATGCCACCAAGTTGTCATCA	20	182
TUJ1		TAGACCCCAGCGGCAACTAT	20	GTTCCAGGTTCCAAGTCCACC	21	127
GAPDH		TTCACCACCATGGAGAAGGC	20	GGCATGGACTGTGGTCATGA	20	237

(#17502-001), 1X B27 supplement (#17504044), 1X Pyruvate (#Panbio 43100), 0.0025% BSA, 1% Pen-Strep (#15140-122)) (Figure 11). By a total of 13 days monitoring, neurons were analysed by bright-field microscopy and qPCR for different time points followed by neuronal characterization by Map2 immunostaining. The sequences of the primers used for qPCR are listed in (Table 2)

3.5.4. Expression and Purification of Recombinant Mouse LIF

Leukaemia inhibitory factor (LIF) is an essential supplementation to mESC media to maintain pluripotency of mouse embryonic stem cells and to have stable conditions prior to differentiation. However, due to high cost, we developed a method to cost effectively produce recombinant mouse LIF using bacterial expression systems [78].

Table 3. Primers used for recombinant LIF production

Target Gene	Forward 5' to 3'	Reverse 5' to 3'	Expected Fragment Size (bp)
mLIF	GATCGGATCCCCTCTTCCCATCACCCCTGTA	GATCCTCGACCTAGAAGGCCTGGACCACCA	552

To do this, total RNA was extracted from NMuMG cells to amplify LIF coding region from cDNA. Then, it was cloned to the pGEX-6P-1 vector to create an N-terminal GST-tagged construct as described in Figure 12

The plasmid expressed via BL21 cells for protein expression by IPTG induction. Then lysed and incubated with glutathione-agarose beads. Acquired fusion protein then cleaved by HRV 3C protease and dialyzed and concentrated resulting in approximately 0.8 mg of protein/ 100 ml culture.

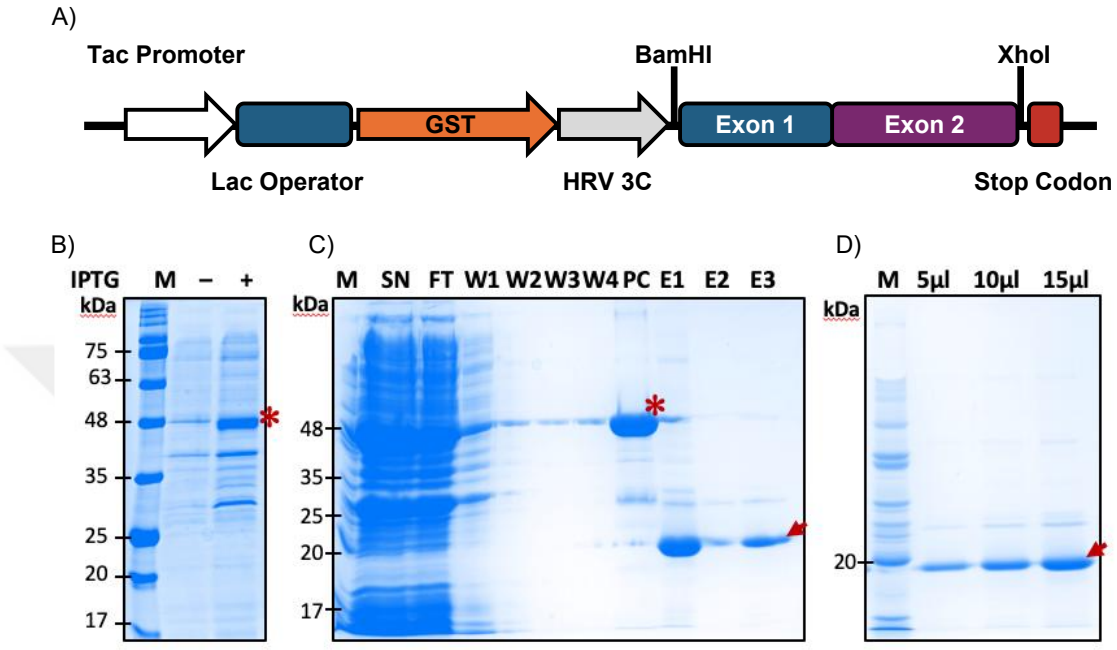

Figure 12. Cloning, expression, and purification of recombinant mouse LIF.
A) Schematic representation of LIF cloning into the pGEX-6P-1 vector using BamHI and XhoI sites. B) SDS-PAGE showing GST-LIF expression in E. coli BL21 cells of uninduced and IPTG-induced lysate. Asterisk indicates GST-LIF (~46 kDa). C) Purification of GST-LIF using glutathione-agarose beads (SN), cleared lysate (FT), flow-through (W1–W4), wash steps (PC), pre-cleavage (E1–E3), eluates after HRV 3C protease cleavage. Arrowhead marks cleaved LIF (~20 kDa). D) SDS-PAGE analysis of the final purified and concentrated HM-LIF protein.

3.5.5. Immunofluorescence Staining and Confocal Microscopy

Table 4. Antibodies used in this study

Antibody	Catalog No.	Company	Dilution	Host	Application	Size
Anti E-Cadherin	BD 610181	BD Biosciences	1:500	Mouse	Immunofluorescence staining	-
			1:1000		Western Blot	130 kDa
	bs-10009R	Bioss Antibodies	1:500	Rabbit	Immunofluorescence staining	-
Anti N-Cadherin	BD-610920	BD Biosciences	1:1000	Mouse	Western Blot	140 kDa
Phalloidin	A12379	Invitrogen	1:500	488-conjugated	Immunofluorescence staining	-
	A22287		1:500	647-conjugated	Immunofluorescence staining	-
Anti H3F3B	Abnova-H00003021-M01	Abnova	1:1000	Mouse	Western Blot	17 kDa
			2 ul		ChIP	
Anti- Tubulin	ab56676	Abcam		Mouse	Western Blot	52 kDa
Anti- β-Actin	3700S	Cell Signalling	1:2000	Mouse	Western Blot	45 kDa
Anti-human E-Cadherin APC antibody	FAB18381A-025	R&D Systems	1:500	Mouse	Immunofluorescence staining	-
Anti-human CD326 (EpCAM) FITC Antibody	324204	Biolegend	1:11	Mouse	Flow cytometry	-
IGG-HRP-linked-Mouse	7076-S	Cell Signalling	1:5000	Mouse	Western Blot	-
IGG-HRP-linked-Rabbit	7074-S	Cell Signalling	1:5000	Rabbit		-
Elf3	NBP1-30873S	Novus Biologicals	1:200	Rabbit	ChIP	41 kDa
Anti-Map2	Ab32454	Abcam	1:150	Rabbit	Immunofluorescence staining	70 kDa

MCF10A cells were seeded on cover slides assembled in 6 wells for H3.3A related experiments and 12-well plates for both Fsk $^{(+)}$ and Fsk $^{(-)}$ cells and treated with and w/o TGFβ3 (5 ng/ml) for 4 or 10 days. Cells then washed with PBS and fixed with 4% formaldehyde for 10 min and permeabilized for 10 min with 0.25% Triton X-100. The cells were incubated with primary antibodies in different dilutions as listed at Table 4 for 1h at room temperature. Then, the cells were washed thoroughly and incubated with secondary antibodies for 1h at room temperature. DAPI staining (1:1000, Invitrogen, D1306)) was performed for nuclei staining and the slides were mounted with antifade mounting solution (Thermo Fisher, P36962). Immunoassayed cells were visualized by confocal microscopy (Zeiss LSM880) and processed with ZEN and ImageJ (v.1.54k) software.

3.5.6. siRNA Transfection

Both MCF10A and NMuMG cells have been transfected by 20 nM siRNA targeting human H3.3A (H3f3a), histone regulator A (HIRA), and mouse H3.3A (H3f3a), genes using Lipofectamine RNAi-Max (13778150 Invitrogen) for 72 h for three biological replicates.

In MCF10A cells, transfections were performed for 4 potential siRNAs provided by Qiagen and analysed for off-target effects by UCSC-Blat and one or more siRNAs was selected for further experiment according to preliminary results of

morphological analysis and RNA expression levels of E-Cadherin. The list of siRNAs is given at Table 5 in detail.

Table 5. Sequences and targets of siRNAs

siRNA-ID	Organism	Target Gene	Target sequence	Length	Vendor	#CatNo
Hs_H3F3A_3	Human	H3.3A	CTCCGTGAAATTAGACGTTAT	21	Qiagen	Product Name: FlexiTube GeneSolution GS3020 for H3f3a GeneGlobe Id:GS3020 Catalog Number: 1027416
Hs_H3F3A_5			ATGCGGAGACGTAAAGCATTA	21	Qiagen	
Hs_H3F3A_8			ATACGTGGAGAACGTGCTTAA	21	Qiagen	
Hs_H3F3A_9			CAGCGGTTCAACTTTATAATA	21	Qiagen	
Hs_HIRA_7		HIRA	GCAGGCGATTCTGTCAATAAA	21	Qiagen	Product Name: FlexiTube GeneSolution GS7290 for HIRA GeneGlobe Id: GS7290 Catalog Number: 1027416
Hs_HIRA_8			CTGGGTCAACCACAATGGCAA	21	Qiagen	
Hs_HIRA_9			AAAGCTGTGACTGTCGTGAAA	21	Qiagen	
Hs_HIRA_10			AACGAAGGGTTTGAATACCGA	21	Qiagen	
siRNA J-042679-06	Mouse	H3f3a	AGAAUCAGGUAUUGGCGUU	19	Qiagen	ON-TARGETplus Mouse H3f3a siRNA J-042679-06

Table 6. RT-PCR primers for amplification of H3.3A splice variants

Splice Variant	Forward	Length	Reverse	Length	Product Size
ENST00000366814.3	TCGTTACAGGCCTGGTA	17	CACAACAGGAATACAAACTCT	21	208 bp
ENST00000366813.1	GATCATAATTTCCAGATTTGG	21	AGTACCAGGCCTGTAACGATG	21	176 bp
ENST00000667897_1	TAAAATGGAGGCAAGTG	17	GAGAATGAAATGTTTCC	17	168 bp

3.5.7. mRNA Expression Analysis

For gene expression analysis, total RNA was isolated from control and knockdown cells by NucleoSpin RNA Mini kit (740955.50, Macherey-Nigel) and the integrity and quantity of RNA samples was determined by NanoDrop 2000' (Thermo Scientific). Then, 500 ng or 1 ug of total RNA is reverse transcribed into cDNA using the Maxima First Strand cDNA Synthesis Kit (K1642, Thermo Scientific). The acquired cDNAs were diluted 1:20 and used for qPCR analysis, performed to analyse the expression of EMT, H3.3A, cell cycle and stemness related genes with SybrGreen Master Mix or LightCycler® 480 Probes Master (Roche, 04707494001 and quantified using the $\Delta\Delta$Ct method. Primers and probes are presented in Figure 7.

Table 7. List of primers used for qPCR

Target Gene	Probe	Organism	Reagent	Forward 5' to 3'	Reverse 3' to 5'	
CDH1	N/A	Human	SybrGreen	GCTTCTGCTCAT TACTACACTGGT	CTGGCCGATAGA ATGAGACC	78
CDH2	N/A	Human	SybrGreen	AGATGGCCCTT GACATTGAG	CAGGGAGGAAAA GTTTGGAA	95
EHF	12	Human	LightCycler® 480 Probes Master	TTCCCACCCAGA ATCTTTAGG	CCGGGGTTGAGA TTCATTAC	73
ELF3	2	Human	LightCycler® 480 Probes Master	GATGCTGGGAC CCTTAGGA	TGGAGGTCTCTG CCTCCAT	66
EpCAM	8	Human	LightCycler® 480 Probes Master	CAAAGCTGGCT GCCAAATGT	TCAGGTTTTGCTC TTCTCCCA	76
FN1	31	Human/Mouse	LightCycler® 480 Probes Master	AGGTGGACCCC GCTAAAC	TGCCGCAACTACT GTGATTC	60
GRHL3	30	Human	LightCycler® 480 Probes Master	GTTGAAGACCC CAGACCTGA	TCAGGGAACCCAT ACTTCTCA	63
PUM1	22	Human	LightCycler® 480 Probes Master	GATCGGAGAGT GGGGGACTA	CTTAGACAGGAAT CGCCCGG	76
VIM	N/A	Human	SybrGreen	CTCCATGTGCC GGATAGC	CGATTTCACCAGA AGCCTCTAC	92
ZEB2	N/A	Human	SybrGreen	TTGAAGTGATGC ATGTGTGAAT	ACCACCTTACAAA GGCTTTCTTT	103
SNAI1	2	Human	LightCycler® 480 Probes Master	CTACAAGGCCAT GTCCGGAC	ATCTGAGTGGGTC TGGAGGT	114
ZEB1	137	Human	LightCycler® 480 Probes Master	CTGCTGGGAGG ATGACACAG	CTGCTTCATCTGC CTGAGCT	71
HIRA	57	Human	SybrGreen/LightCycler® 480 Probes Master	ATTATGGTGTGG AAGCGGGC	TGGCAAGCTTACC ACTGGAG	70
H3F3A	19	Human/Mouse	SybrGreen/LightCycler® 480 Probes Master	GCCATCTTTCAA TTGTGTTCG	GCCATGGTACAG AGACCTCCT	124
Cdh1	18	Mouse	LightCycler® 480 Probes Master	ATCCTCGCCCT GCTGATT	ACCACCGTTCTCC TCCGTA	62
Cdh2	17	Mouse	LightCycler® 480 Probes Master	TCCCTGAGATAC AGCGTCACT	ATAATGAAGATGC CCGTTGG	62
Ehf	29	Mouse	LightCycler® 480 Probes Master	GATAATTGGTGG GCGACAA	CTTAAGGGGAAA GAGTCATGATTTA	95
Gapdh	9	Mouse	LightCycler® 480 Probes Master	AGCTTGTCATCA ACGGGAAG	TTTGATGTTAGTG GGGTCTCG	62
Grhl3	100	Mouse	LightCycler® 480 Probes Master	AAGGAAGATGT CGAATGAACTTG	TCGTCCTCATTAC TGTAGGGAAA	96
Vim	74	Mouse	LightCycler® 480 Probes Master	ACGTTTCCAAGC CTGACCT	AGCCACGCTTTCA TACTGCT	65

3.5.8. Protein Purification and Western Blot Analysis

Cells are washed with 1X PBS prior to dissociation. Then dissociated by 0.25 uM EDTA solution for 20 mins. Dissociated cells are precipitated by cold centrifugation at 0.3 rpm for 5 mins. Then, lysed for 30 mins on ice by RIPA buffer containing; 25 mM Tris–HCl pH 7.6, 150 mM NaCl, 5mM EDTA, 1% NP40 or 1% Triton X-100, 1% Sodium deoxycholate, 0.1%SDS and freshly added 1 mM DTT (Sigma, 43815)), 1 mM PMSF (Sigma, P7626), 1X Protease inhibitors (Roche) (Roche, 11873580001). Then the supernatant containing protein from whole cell extraction is collected by centrifugation at 14,000g, 10 min, 4 ^{0}C. Protein expression was analysed by western blotting by electrophoresis of 40 ug protein on 10 % SDS-Gel and transferred to PVDF membranes (Millipore, IPVH00010). Then, membranes are blocked for 1 h at room temperature by 5% milk solution. Blocked membranes are incubated overnight by primary antibodies and 1h at room temperature with HRP-linked secondary antibodies listed at Table 4 and visualized by ECL kit (Bio-Rad, 1705061) on Bio-Ead Gel Imaging (Bio-Rad, 17001402). Images are quantitatively analysed using ImageJ software.

3.5.9. Cell Nucleus Size and Foci Analysis

Nuclear size analysis was performed using ImageJ (NIH,v1.53k). DAPI stained images were first converted to 8-bit grayscale and segmented by automatic thresholding with converting into binary mask with black background. Then, particles with a 0.8 to 1.00 circularity were identified using analyse particle's function.

For γH2AX foci quantification, images were processed using the Gaussian blur (Sigma=1) method with background substruction to reduce noise and converted into stack. Then, foci were detected by find maxima function with a prominence threshold of 45. Average number of foci is calculated by number of foci/nuclei. Both analyses performed in triplicates.

3.5.10. Flow Cytometry Analysis

$1x10^6$ cells are prepared as single cell suspension by dissociating with 0.25 uM EDTA solution and washing with PBS, then incubated with 1 ul Anti-human CD326 (EpCAM) FITC (#Biolegend 324204) and Anti-human E-Cadherin APC (#FAB18381A-025-) antibodies for 1h at room temperature and resuspended at 100 ul buffer (1xPBS+5%HorseSerum) to process by BD FACS Canto II (BD Immunocytometry Systems) and analysed by Flowjo software (v.10.10.0).

3.5.11. Single Cell Sorting and Expansion

A total of 1×10^6 cells were dissociated using 0.25 µM EDTA and passed through a 70 µm cell strainer (SPL Life Sciences, 93070) to obtain a single-cell suspension. The cells were then incubated with Anti-human E-Cadherin-APC antibody (R&D Systems, FAB18381A) at a concentration of 10 µl per 1×10^6 cells for 1 hour at room temperature. Following incubation, cells were washed twice with PBS and resuspended in FACS buffer containing 5% horse serum in PBS. Using a BD FACSAria III cell sorter, CDH1-positive and -negative populations were isolated as single cells into 96-well plates, starting from an initial population of 10×10^6 cells.

3.5.12. RNA-seq Analysis

Total RNA was isolated using the NucleoSpin RNA II kit (Macherey-Nagel), according to the manufacturer's instructions. The Agilent Bioanalyzer 2100 was used to assess the integrity of the RNA after RNA-seq libraries were created using the Illumina Stranded Total RNA Prep with Ribo-Zero Plus kit. An outside service provider performed the sequencing on an Illumina NovaSeq 6000 platform. Trimmomatic (v0.39) was used to process raw reads to eliminate adapter contamination and trim

low-quality sequences. HISAT2 (v2.0.5) was used to align clean reads to the GENCODE human reference genome (GRCh38, release v37). Hisat2-build was used to generate genome indices, and the -dta option was used to perform alignments in order to preserve splicing information. SAMtools (v1.10) was then used to convert and sort SAM files into BAM format. The Rsubread package's featureCounts function was used to quantify gene-level expression. Low-expression transcripts (FPKM < 0.5 in all treated and control samples) were not included in the analysis. Principal component analysis (PCA) and heatmaps were then created using RNA-seq data to assess transcriptional variation among biological replicates and treatment groups. List of the EMT signature gene set that was used to create the heatmap can be found on Table 1.

3.5.13. Cell Cycle Analysis

$1x10^6$ cells were collected from Fsk $^{(+)}$ and Fsk $^{(-)}$ cells that are treated with and w/o TGFβ3 for 10 days. Then, washed in cold PBS once and fixed by drop-by-drop ice-cold absolute ethanol and incubated at 20°C overnight. Fixed cells then washed twice in ice-cold PBS and stained with 50 µg/mL PI, 1 mg/mL RNAase A, 0.05% Triton X containing staining solution for 30 mins at room temperature. The DNA quantified by BD FACS Canto II (BD Immunocytometry Systems) to reveal the distribution of cells during cell cycle stages and analysed by Flowjo software (v.10.10.0).

3.5.14. Growth Curve and Srb Assays

$5x10^3$ cells were plated into 12-well plates for 10days with and w/o TGFβ3 for both Fsk $^{(+)}$ and Fsk $^{(-)}$ cells while media changed every 2 days. Then cells are detached by Trypsin every 2 days and counted using Neubauer chamber. The doubling time was calculated during the exponential growth phase from 48h to 96h according to the formula $DT= \Delta t \times \ln 2/\ln (C^{48h} / C^{96h})$. Δt representing time interval while C representing number of cells for different time points.

3.5.15. Chromatin Immunoprecipitation

Chromatin immunoprecipitation (ChIP) was performed using a micrococcal nuclease-based protocol to assess histone H3.3 and ELF3 occupancy at regulatory regions of the CDH1 and GRHL3 loci following HIRA knockdown or TGFβ3 treatment in MCF10A cells. Following treatment, cells were lysed, and the chromatin was digested using micrococcal nuclease (MNase) overnight to obtain mononucleosomes. The extent of digestion was monitored by electrophoresis on a 2% agarose gel; a

single, well-defined band around 200 bp confirmed efficient MNase digestion. MNase-digested chromatin was immunoprecipitated overnight at 4 °C using the following antibodies, H3.3 (to assess histone variant occupancy), ELF3 (a transcriptional regulator of GRHL3), and IgG (negative control). Protein sepharose beads were used to pull down antibody-bound chromatin. After several washes, DNA was eluted and purified for subsequent qPCR analysis. Primers were designed to amplify the -1 (upstream) and +1 (downstream) regions of the transcription start site (TSS) of CDH1 and GRHL3. Enrichment of target DNA was quantified by real-time PCR using SYBR Green chemistry. Data were normalized to input DNA and presented as fold enrichment over IgG. Primer sequences are listed in Supplementary Table 8.

Table 8. Primers used for qPCR

Target Gene	LAB ID	Probe	Organism	Reagent	Experiment	Forward	Length	Reverse	Length
CDH1 (-1)	SD-530/531	23	Human	SybrGreen	CHIP	GCCCTTTCTGA TCCCAGGTC	20	CCTGCACGGTT CTGATTCCA	20
CDH1 (+1)	SD-532/533	23	Human	SybrGreen	CHIP	CCTGACTTGCG AGGGACG	18	GGTGACGACG GGAGAGGAA	19
GRHL3 (-1)	SD-492/493	20	Human	SybrGreen	CHIP	TCCATCCCTCC TCCCTCATC	20	TGTTAACTCTT AGCCCGCCG	20
GRHL3 (+1)	SD-494/495	3	Human	SybrGreen	CHIP	GCACCTGTACC TGTAGCCAA	20	TGGGTGTCGA GATTTTGCTGA	21

3.5.16. Statistical Analysis

Statistical analyses of qPCR and related experimental results were carried out using one-way or two-way ANOVA, followed by Tukey's post hoc tests, calculated and visualized by GraphPad Prism (v10.4.1). All computational analyses regarding RNA-seq were performed in R. Gene expression heatmaps were created with the pheatmap package (v1.0.12), using row-wise scaling of log2(FPKM + 1) values and filtering out genes with low expression (rowsums ≤ 0.5). Principal component analysis (PCA) was conducted using the prcomp function from the stats package, and results were visualized using ggplot2 (v3.5.2).

3.6. Planning and Calendar of the Study

February 2020-April 2020	April 2020-May 2025	February 2022-April 2023	May 2025-July 2025
Literature Reading	In-Vitro Analysis	In Silico Analysis	Writing

3.7. Limitations of Study

The study was limited to two epithelial cell lines (MCF10A and NMuMG), which may not fully capture tissue-specific or in vivo complexity of EMT.

Additionally, due to import restrictions, cholera toxin which is a critical component of MCF10A medium for maintenance could not be used. This required extensive media optimization, which may have influenced cell behaviour and phenotype.

3.8. Ethical Committee

This thesis was approved by Izmir Biomedicine and Genome Center Noninvasive Research Ethics Committee (IBG-GOEK) carrying protocol number “2022-039” *(see Appendix)*

4. RESULTS

4.1. Comparative Assessment of EMT Marker Expression Across Multiple Cell Models as MCF10A, NMuMG, and Embryonic Stem Cells Undergoing Neuronal Differentiation

Since EMT is a dynamic and context dependant process, we used a comparative approach to understand the EMT marker expression and response across multiple cell models including non-tumorigenic mammary epithelial cell line MCF10A, murine mammary epithelial cell line NMuMG and mouse embryonic stem cells undergoing neuronal differentiation. We employed TGFβ3 induced EMT for two

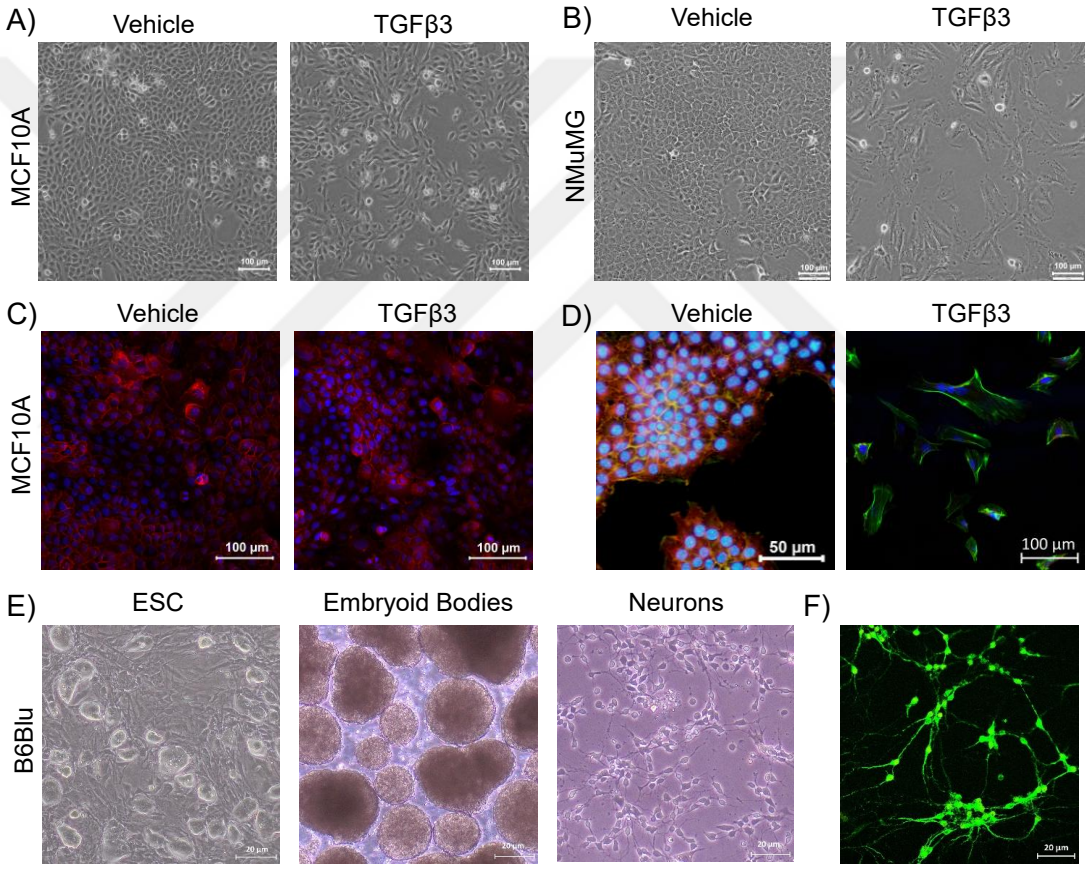

Figure 13 Comparative analysis of EMT induction across three different cell models as MCF10A cells (non-tumorigenic human mammary epithelial) cells, NMuMG (normal murine mammary gland epithelial) cells, B6Blu (mouse embryonic stem cells).
Phase contrast images of A) MCF10A cells for control (vehicle) B) NMuMG cells and after 4 days and 3 days of TGFβ3 treatment respectively, representing a transition from epithelial to mesenchymal morphology. Immunofluorescence staining of C) E-cadherin (red) and nuclei in MCF10A and D) E-cadherin (red) and Phalloidin (green) in NMuMG cells with and without TGFβ3 treatment. E) Phase contrast images of different phases of neuronal differentiation of mESCs cultured on HM-LIF. ESCs representing undifferentiated mESC grown on MEF feeders while embryoid bodies formed by day 8, followed by neurite outgrowth and neural networks on day13. F) Immunofluorescence staining for MAP2 (green) confirming neuronal differentiation. Overall representing TGFβ3 induced and developmental EMT-like process.

well established epithelial cell line models (MCF10A and NMuMG) to study the role of histone variant H3.3A. Additionally, since neuronal differentiation of embryonic stem cells demonstrates EMT-like transitions characterised by downregulation of epithelial markers and upregulation of mesenchymal profile suggesting a good in vitro model to study EMT from developmental aspects. Given the developmental importance of EMT-like processes during neurogenesis, we initially wanted to examine if the histone variant H3.3 was dynamically regulated during neuronal differentiation of mESCs in parallel to MCF10A and NMuMG cells. This comparative approach was intended to explore whether chromatin level changes involving H3.3 might be a shared feature of EMT across different biological contexts.

To establish EMT models for our study we first analysed MCF10A and NMuMG cells by phase contrast microscopy upon TGFβ3 induction. Consistent with EMT induction, images showed, upon 4 days of 5 ng/ ml TGFβ3 induction for MCF10A (Figure 13.A) and 3 days of 2.5 ng/ml for NMuMG cells (Figure 13.B) ,as previously optimized by our group, morphology of both cells have changed from more cobblestone like epithelial morphology to elongated, spindle shaped mesenchymal like morphology, with stronger observations on NMuMG cells. To further examine the profile, immunostaining with E-Cadherin and phalloidin antibodies performed and results showed while MCF10A cells did not demonstrate a strong decrease on E-Cad levels, instead reorganization of E-Cadherin protein from membrane to cytoplasm occurred (Figure 13.C) while significant loss of E-Cadherin was identified on NMuMG cells (Figure 13.D).

In addition to TGFβ3 induced cell models, our neuronal differentiation system analysing in three steps as ESC maintenance, embryoid body formation and neural network formation, showed an expected employment of neuronal differentiation. As shown on the bright field images, ESCs transitioned to round, non-adherent embryoid bodies which further differentiated into neuron-like cells (Figure 13.E). It is also further characterised through immunostaining analysis by using Map2 antibody to confirm successful differentiation (Figure 13.F).

4.2. Transcriptional Analysis of EMT Markers and H3.3A Expression Across Cell Models

To support bright field and confocal observations, we next investigated transcriptional response of CDH1 and H3.3A across three models upon EMT. Our results showed an effective EMT characterized by significant downregulation of CDH1 for both MCF10A and NMuMG cells while H3.3 expression was slightly upregulated in MCF10A cells but H3.3A expression didn't show a significant change upon TGFβ3 induced EMT (Figure 14.A-B). Next, we examined neuronal differentiation model, first

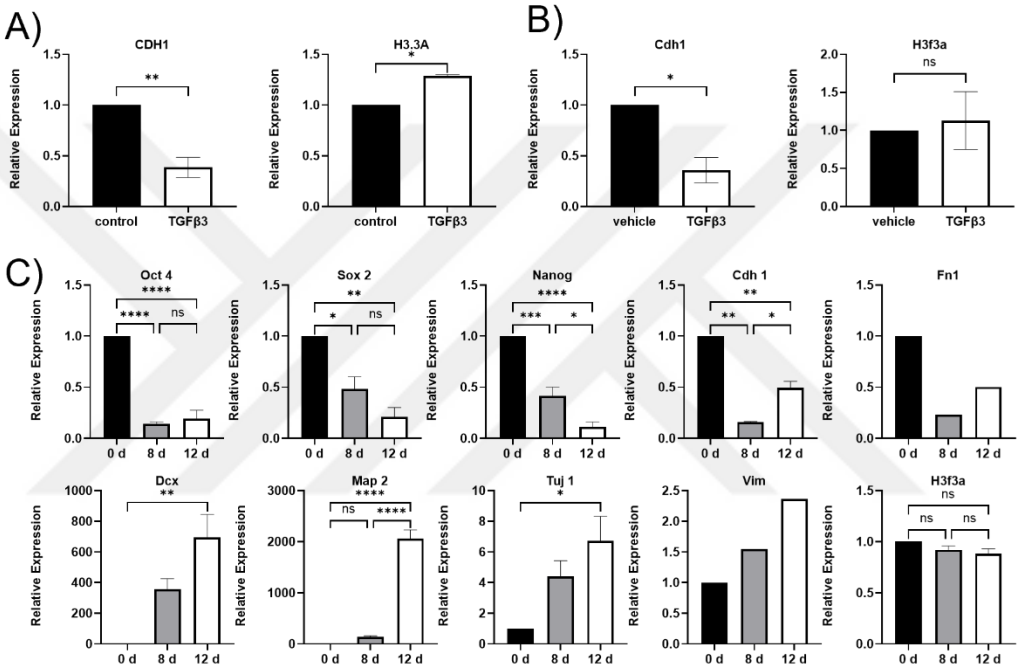

Figure 14. Gene expression analysis of EMT markers of different cell and EMT models MCF10A, NMuMG, and mESCs.
A) qPCR analysis of CDH1 and H3.3A expressions in MCF10A cells with or without TGFβ3 for 4 days. B) Expression of Cdh1 and H3f3a in NMuMG cells after 3 days of TGFβ3 treatment. C) Validation of neuronal differentiation in mESCs cultured with HM-LIF characterised by downregulation of pluripotency markers (Oct4, Sox2, Nanog) and upregulation of neuronal markers (Dcx, Tuj1, Map2). D) qPCR analysis of EMT markers (Cdh1, Fn1, Vim) and expression of H3f3a in mESCs before and after neuronal differentiation showing EMT markers including Cdh1, Fn1 and Vim showed similar expression patterns to TGFβ3 treated epithelial cells. (*p < 0.05, **p < 0.01, ***p < 0.001, ****p < 0.0001)

by assessment of transcriptional changes to confirm efficient neuronal differentiation. To assess this, pluripotency markers such as Oct4, Sox2 and Nanog and neuronal markers such as Dcx, Map2 and Tuj1 were analysed for three stages of ESCs, embryoid bodies and neurons. Results showed significant downregulation of pluripotency markers along with concurrent upregulation of neuronal markers confirming the loss of stemness and successful neuronal differentiation (Figure 14).

After confirmation of model set up, we examined the expression of EMT markers including Cdh1, Fn1 and Vim and H3f3a gene. During the differentiation process, results showed significant Cdh1 downregulation and Fn1 and Vim upregulation suggesting EMT-like process (Figure 14.C). However, H3f3a expression remained stable through all stages similar to NMuMG cells (Figure 14.C, bottom right).

4.3. H3.3A Knockdown Does Not Induce EMT in NMuMG Cells

To understand the role of H3.3A in EMT induction for mouse cell lines, we have decided to continue our experiments using NMuMG cells considering strong morphology upon TGFβ3 induction and technical and financial limitations of ESC culture and differentiation protocols, even though our effort to outcome the financial limitations by recombinant protein production (Figure 12).

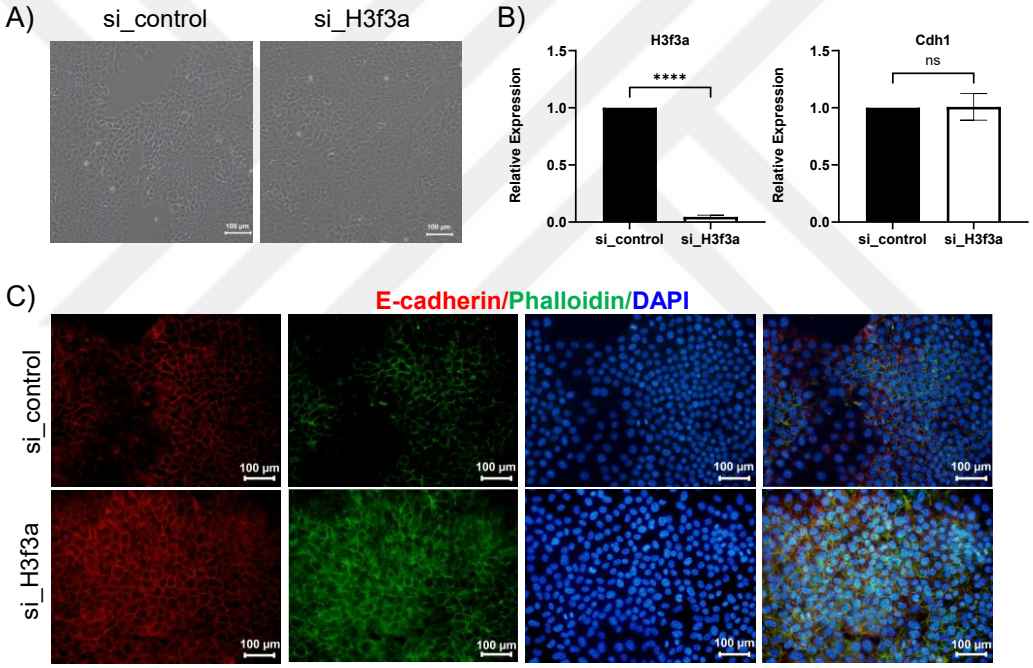

Figure 15. H3f3a knockdown in NMuMG cells does not induce significant changes.
A) Brightfield images showing the morphology of NMuMG cells following siRNA mediated knockdown of H3f3a (H3.3A) expression for 72 hours showing no morphological changes. B) qPCR validation of H3f3a knockdown efficiency confirms significant downregulation of H3f3a levels compared to control untreated cells. C) qPCR analysis showing Cdh1 expression demonstrates no significant change following H3f3a knockdown D) Immunofluorescence staining for E-Cadherin and phalloidin further confirms consistent epithelial structure, with E-Cadherin localization at cell junctions and preserved phalloidin profile indicating that although H3f3a knockdown was efficiently performed, cells do not undergo EMT. (*p < 0.05, **p < 0.01, ***p < 0.001, ****p < 0.0001)

To assess the impact of H3.3A depletion on NMuMG cells, we performed siRNA mediated knockdown for 72 hours and compared to control cells. Bright field images revealed no significant changes in cell morphology (Figure 15.A) further confirmed on transcriptional level by assessment of Cdh1 expression levels

(Fig.16.B). Then, we wanted to analyse if E-Cadherin protein relocated from membrane to cytoplasm without any change on expression level. However, results showed neither loss nor redistribution of the protein and with no difference on the F-actin staining by phalloidin (Fig.16.C). Altogether, suggesting H3.3A depletion does not promote EMT in normal murine mouse epithelial cells, NMuMG.

4.4. siRNA-Mediated Knockdown of H3.3A Produces Variable Effects on Cell Morphology and CDH1 Expression

To understand the role of H3.3 in epithelial to mesenchymal transition, H3.3A was depleted through si-RNA mediated knockdown in MCF10A cells by 4 different siRNAs (si_03, si_05, si_08, si_09) targeting H3.3A gene at a final concentration of 20 nM, using Lipofectamine RNA-iMax transfection reagent. After 24h of siRNA transfection, followed by 48h of post-transfection, cells are first examined by phase-contrast microscopy. Initial assessments showed that among four different siRNAs targeting H3.3A, different morphologies observed (Figure 16).

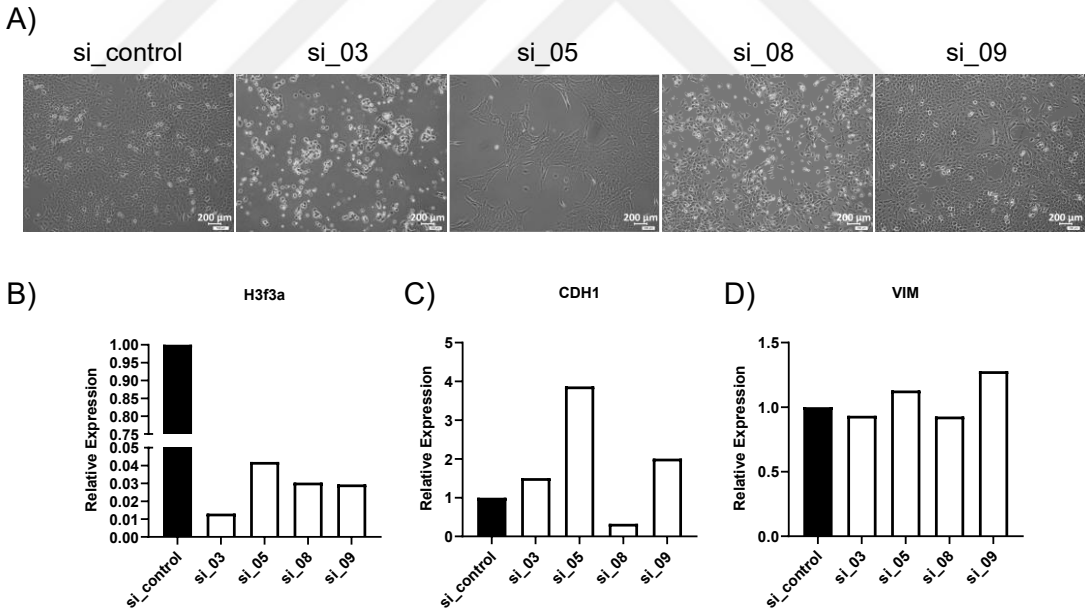

Figure 16. Different siRNAs targeting H3.3A produce variable effects on cell morphology and CDH1 expression.
A) Phase-contrast images showing different morphologies among four siRNAs targeting H3.3A, si_03 causes excessive cell death, si_05 and si_09 have minimal effects on both morphology, while si_08 shows EMT-like characteristics, following 72h of siRNA transfection B) qPCR analysis revealing that although all siRNAs shows significant decrease on H3.3A levels, C) si_08 leads to a significant reduction in CDH1 expression while si_03 and si_09 leads minimal differences and si_05 shows an upregulation in CDH1 gene expression highlighting the importance of siRNA selection in functional studies. D) No significant difference is observed on VIM levels among all siRNAs. List of siRNAs with the sequence information can be found at Table 5.

Specifically, si_03 was causing extensive cell death with cellular debris, possible apoptotic cells and significant decrease in the cell density. On the other hand, si_05 and si_09 had minimal impact on cell morphology and viability showing epithelial morphology characterized by a cobblestone-like structure with high cell-cell junctions and limited intercellular spacing. Significantly, si_08 induced more elongated cell morphology with reduced cell-cell contacts, suggesting an EMT-like phenotype which is characterised by spindle-shaped morphology. Furthermore, we extended our research to RNA level, to understand the morphological differences among siRNAs remain on the transcriptional level. Our results showed that, all siRNAs were efficient to knockdown H3.3A gene as the mRNA expression of the gene decreased by 95.8 to 98.7 % among all siRNAs (Figure 16.B). To look from EMT perspective, we also investigated CDH1 and Vimentin (VIM) mRNA expressions which revealed that although all siRNAs resulted in significant decrease on H3.3A levels, si_08 led to a significant downregulation of CDH1 expression while si_03 and si_09 led non-significant increase and si_05 showed upregulation on CDH1 levels (Figure 16.C). In addition, none of the siRNAs induced a change on VIM levels (Figure 16.D).

4.5. siRNA Target Sites and Splice Variant-Specific Depletion of H3.3A in MCF10A Cells

Given the distinct phenotypical differences following siRNA mediated transfection with different siRNAs, we wanted to analyse the possibility of off-target effects. All siRNA sequences were analysed by blat using UCSC Genome Browser to see any off-target effect in-silico. Analysis showed no off-target effect. However, we noted that each siRNA was designed to a different region of the H3.3A gene. Since, H3.3A gene has multiple transcript variants through alternative splicing, the sequence hit ratio of siRNAs into different splice variants differ widely. When we examined the exon-intron structures and sequence alignments on H3.3A splice variants, our analysis revealed that, si_03 was able to knockdown all splice variants and si_08 has sequence match except “ENST00000366814.3” while si_05 and si_09 only targets four and three variants (Figure 17.A). To further understand if the difference might be significantly resulted from these splice variants, we analysed RNA-seq data of MCF10A cells without any treatment to determine the expression levels. The results revealed that although the canonical transcript (ENST00000366815.10) is the most abundant, multiple variants are expressed above threshold (Figure 17.B).

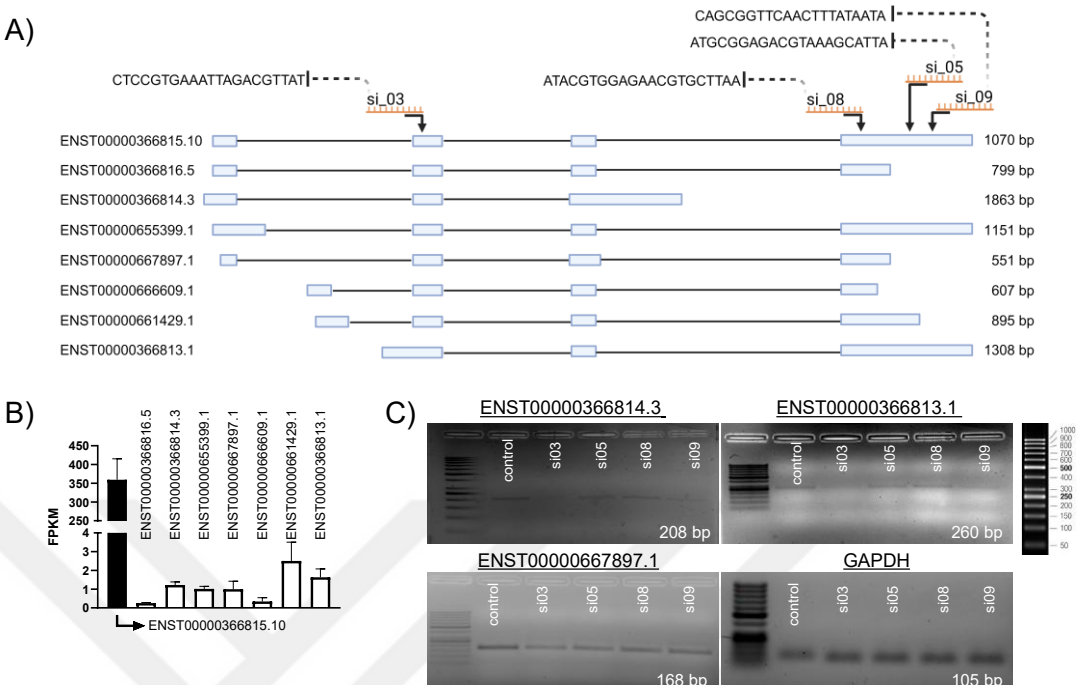

Figure 17. siRNA target regions and expression of H3.3A splice variants.
A) Schematic illustration showing the target sites of different siRNAs on H3.3A splice variants. The exon-intron structures of the transcript isoforms were analysed using UCSC Genome Browser, and the schematic was created with BioRender. B) RNA-seq analysis of control MCF10A cells showing detectable expression of H3.3A splice variants while the reference H3.3A (ENST00000366815.10) showing significantly higher expression. C) RT-PCRs showing the level of depletion for each siRNA for different transcript variants, GAPDH was used as internal control.

Additionally, we designed variant-specific RT-PCR primers to evaluate the knockdown efficiency of each siRNA for each transcript variant. The PCR products were visualized on 2% agarose gel to assess the extent of depletion for each siRNA for each variant. Among these, we were able to amplify ENST00000366814.3, which showed complete downregulation by si_03 but no change was observed on remaining siRNAs as expected. RT-PCR targeting ENST00000366813.1 showed complete depletion by si_03 and slight downregulation by si_08. Additionally, all siRNA treatments resulted in slight downregulation of ENST00000667897.1 expression (Figure 17.C). On the other hand, remaining splice variants could not be analysed by RT-PCR because of low expression and minor sequence differences.

4.6. H3.3A Depletion and TGFβ3 Treatment Induce Similar Morphological Changes and Cytoskeletal Remodelling

Considering these analyses, the contribution of individual transcript variants to the observed phenotype and the functional relevance of H3.3A isoforms in epithelial identity is explored to decide the selected siRNA for further experiments. si_03,

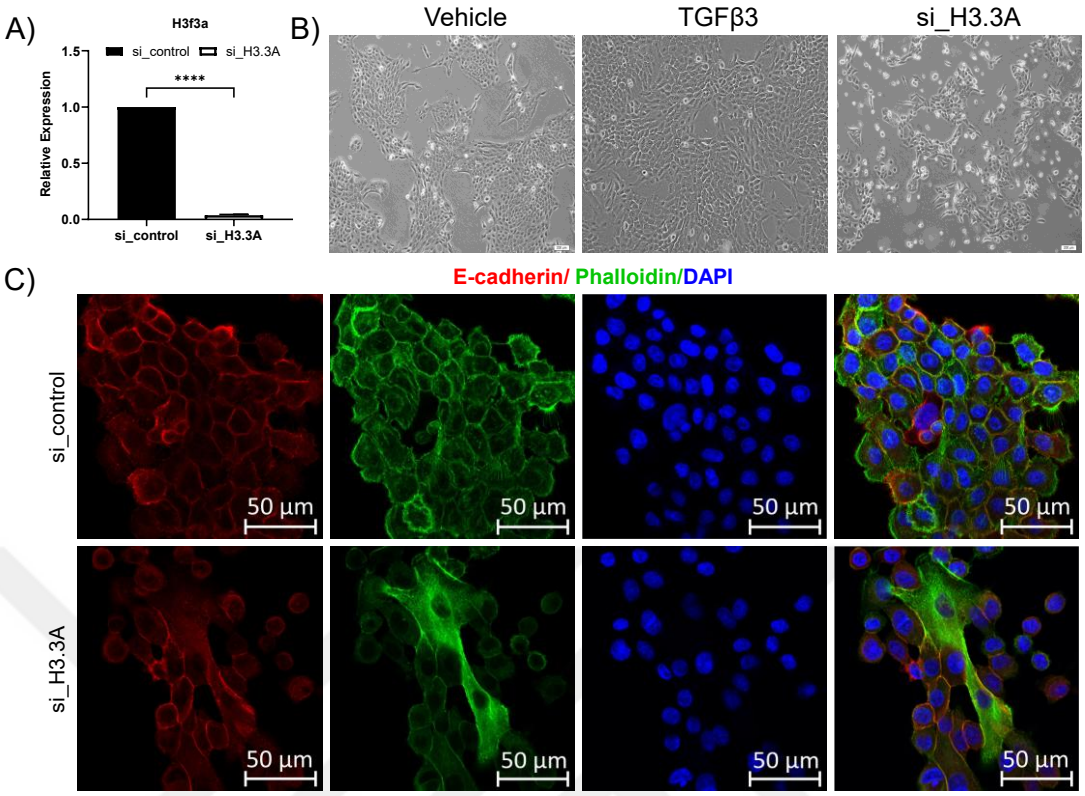

Figure 18. H3.3A knockdown and TGFβ3 treatment induce similar morphological changes.
A) Quantitative PCR analysis showing an efficient knockdown in H3.3A mRNA levels following siRNA-mediated knockdown by si_08 compared to the control condition. Data are presented as mean ± SD (n = 6). Statistical significance was determined using multiple t'tests. B) Bright-field microscopy shows that both H3.3A knockdown (72 hours) and TGFβ3 treatment (4 days) shows slight changes in morphology such as a spindle-shaped, mesenchymal-like morphology compared to vehicle cells, which maintain a cobblestone-like epithelial structure. Additionally, H3.3A knockdown also results in a visible reduction in cell density as a result of increased cell death after siRNA treatment. C) Confocal microscopy reveals that siRNA-mediated depletion of H3.3A leads to a significant loss of membrane-localized E-Cad (red) and induces the formation of actin stress fibers by phalloidin staining (green), compared to control cells. Nuclei are counterstained with DAPI (blue). (*p < 0.05, **p < 0.01, ***p < 0.001, ****p < 0.0001)

although effective against all transcript variants, was cytotoxic and unsuitable for continued use. si_08, in contrast, targets most H3.3A variants, missing only one, whereas si_05 and si_09 had limited coverage. These observations support the interpretation that the effects seen with si_08 reflect the true consequence of H3.3A depletion, while the lack of phenotype with si_05 and si_09 may result from incomplete silencing due to variant-specific compensation. After selecting si_08 as the most suitable siRNA for H3.3A knockdown, we performed experiments to investigate its effects further. To start with, we performed transfection by si_08 many times with different biological replicates at different time points and revealed 96.2% knockdown on average (n=6) (Figure 18.A). To better understand the effect of H3.3A depletion on EMT, we performed TGFβ3 treatment which is a commonly used inducer for EMT studies for 4 days as control to induce EMT in MCF10 cells. Phase-contrast

microscopy revealed that both H3.3A depletion and TGFβ3 treatment resulted in visible but slight morphological changes including spindle shaped and mesenchymal like morphology (Figure 18.B). In addition, H3.3A knockdown resulted in visible decrease in cell density compared to TGFβ3 treatment might be caused by cell death following siRNA transfection or the effect of H3.3A itself. Confocal microscopy further confirmed the loss of E-Cadherin on the membrane for both conditions with significant overall decrease on the expression when H3.3A is depleted. Additionally, phalloidin staining revealed actin stress fibre formation across cytoplasm for both conditions confirming EMT-like phenotype (Figure 18.C). Moreover, we observed unexpected E-Cadherin localization on both vehicle and TGFβ3 treated MCF10A cells as E-Cad were localized both on membrane and cytoplasm with some cells with no E-Cad expression, which did not reflect normal epithelial phenotype.

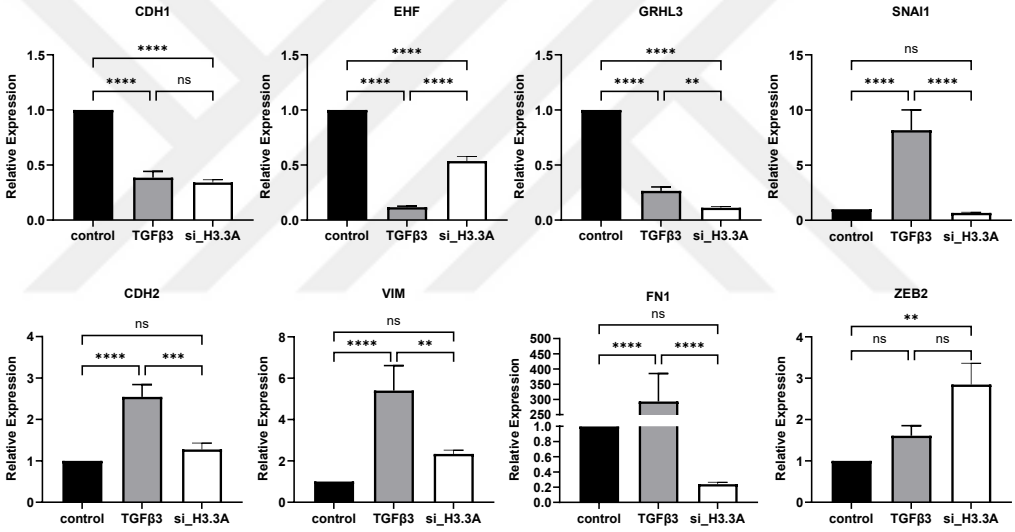

Figure 19. Depletion of H3.3A induces an EMT-like transcriptional profile similar to TGFβ3 induced EMT. qPCR analysis to understand the expression of epithelial and mesenchymal markers. Expression of EMT-related genes was analysed, including epithelial marker CDH1, EHF mesenchymal markers CDH2, FN1, and VIM and EMT-regulating transcription factors SNAI1, OVOL2, and ZEB2. The expression profile indicates a shift toward a mesenchymal-like state upon H3.3A depletion. Data are presented as mean ± SD (H3.3A depletion;n = 6, TGFβ3 treatment; n=3). Statistical significance was determined using t'test where (*p < 0.05, **p < 0.01, ***p < 0.001, ****p < 0.0001)

To determine the effect of H3.3A depletion on transcriptional level, we next examined EMT related genes including CDH1 and CDH2 which their regulation is an important signal of cadherin switch and several epithelial and mesenchymal markers. Among these, CDH1 showed a significant upregulation while CDH2 is significantly downregulated with slight differences between H3.3A depletion and TGFβ3 treatment. Additionally, epithelial markers such as EHF and GRHL3 showed strong

downregulation while mesenchymal markers such as VIM and ZEB2 significantly increased, suggesting an EMT-like phenotype. On the other hand, SNAI1 and FN1 remarkably upregulated on TGFβ3 treatment while H3.3A depletion has no effect on SNAI1 and reversed effect on FN1 expression, speculating a different mechanism than TGFβ3 induced pathway (Figure 19).

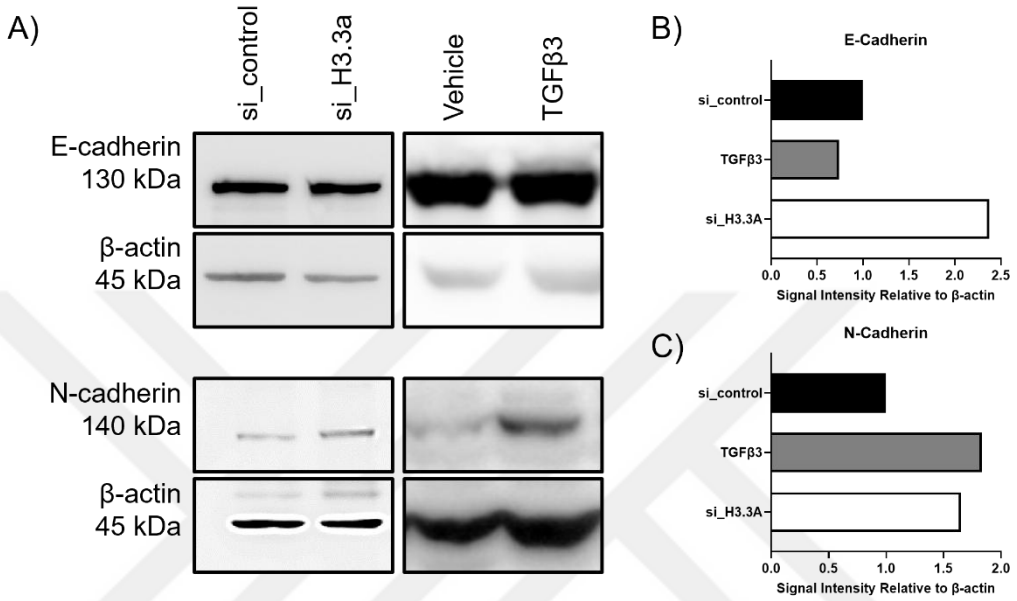

Figure 20. H3.3A Knockdown and TGFβ3 Treatment Induce N-cadherin Upregulation on Protein Level A) Western blot analysis of E-Cadherin and N-cadherin expression in H3.3A knockdown (72 hours) and TGF-β3 treatment (4 days) of MCF10A cells showed that N-cadherin expression was increased in both conditions, while E-Cadherin protein levels remained unchanged by visual inspection of the blots. β-Actin was used as a loading control. B-C) Quantification of signal intensity confirmed a significant upregulation of N-cadherin following both H3.3A knockdown and TGFβ3 treatment showing a mesenchymal transition. In contrast, E-Cadherin levels showed no significant decrease, even quantified as upregulated. The intensity of E-Cadherin and N-cadherin bands were measured and normalized to the corresponding β-Actin loading control using ImageJ. consistent with a mesenchymal transition.

Furthermore, we wanted to analyse if the change in transcriptional level is consistent on the protein level. However, western blots (Figure 20.A) indicated that E-Cadherin levels remained unchanged following siRNA transfection and TGFβ3 treatment while N-Cadherin levels are significantly increased (Figure 20.B-C).

Considering this inconsistency and our prior observations on confocal microscopy, we reasoned that heterogeneity of the population might have an effect on EMT process in MCF10A cells.

4.7. MCF10A cells' heterogeneity misleading the effect of TGFβ3 on EMT studies

To identify and characterize MCF10A cell's response to EMT in detail, we first compared the effects of TGFβ1 and TGFβ3 treatment for 4 days which are known to be major EMT inducers. Our results showed no difference between two inducers; thus, we continued experiments using TGFβ3 (Figure 21.A). Secondly, we further

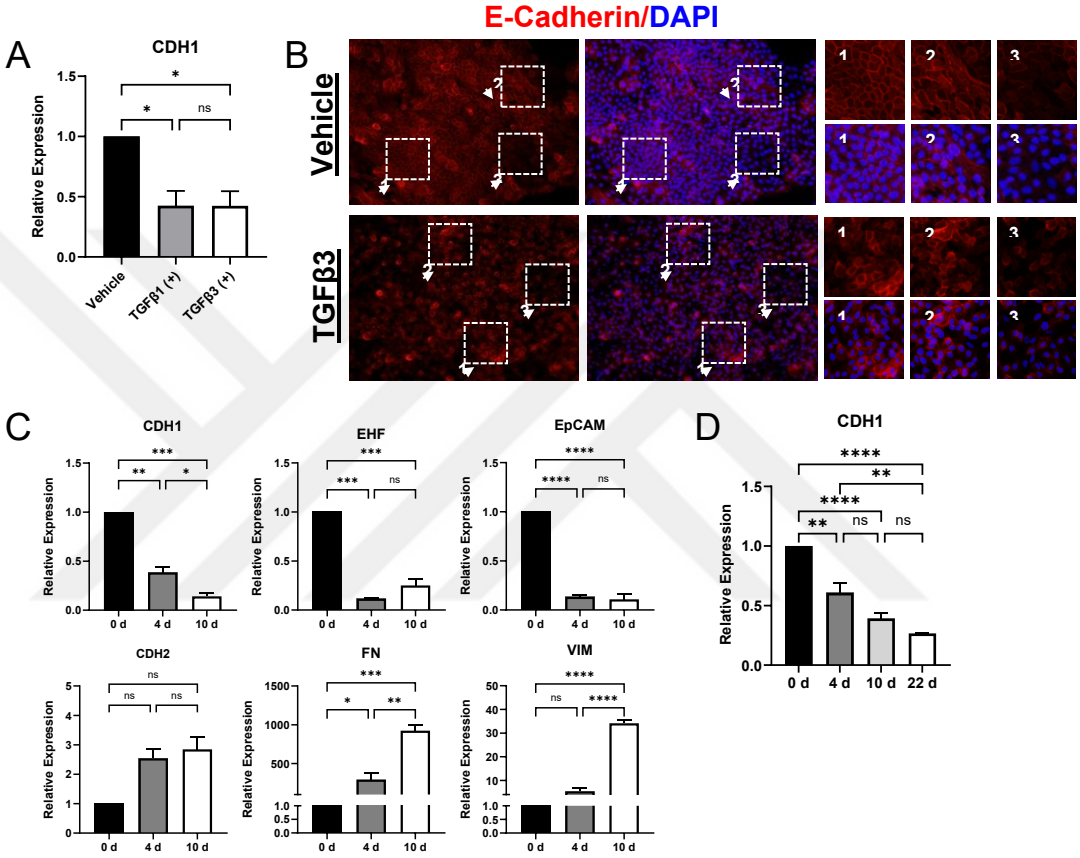

Figure 21. Heterogeneity in MCF10A Cells Reveals Diverse Responses to TGF-β3 Treatment.
A) qPCR analysis of epithelial (CDH1) and mesenchymal (FN1, VIM) markers in MCF10A cells after 4 days of TGFβ1 or TGFβ3 treatment B) Immunofluorescence analysis of E-Cadherin and nuclei were counterstained with DAPI in MCF10A cells with and without TGFβ3 treatment. Higher magnification images of selected regions highlighting the cellular heterogeneity within the sample numbered as membrane located [1], cytoplasm located [2] and lack of CDH1 expression [3], respectively. C) The qPCRs showing the expression of CDH1, CDH2 and EMT markers including EHF, EpCAM, FN, and VIM in control and 4 days of TGFβ3 treated cells. D) CDH1 expression of MCF10A cells after extended TGFβ3 treatment up to 22 days, showing the long-term effect of TGFβ3 exposure. (*p < 0.05, **p < 0.01, ***p < 0.001, ****p < 0.0001)

analysed vehicle and TGFβ3 treated MCF10A cells by confocal microscopy with E-Cadherin staining. Upon examining vehicle and treated cells, we observed the presence of three distinct subgroups within the vehicle MCF10A population: E-Cad $^{(+)}$ cells, which exhibited E-Cadherin localization on the plasma membrane, cells that E-Cad is located on cytoplasm and E-Cad $^{(-)}$ cells with no E-Cad expression. Moreover,

although there is partial EMT throughout the slide, certain areas displayed E-Cadherin localization at the plasma membrane after TGFβ3 treatment (Figure 21.B).

To analyse MCF10A cells from EMT perspective in detail, cells are stimulated by TGFβ3 for two different time points as 4 days and 10 days and mRNA expression of EMT related markers are analysed. To this extend, we used CDH1 and CDH2 as the indicators of cadherin switch, EHF and EpCAM as epithelial markers and FN and VIM as mesenchymal markers for their roles on epithelial/mesenchymal integrity, extracellular matrix and switch between epithelial and mesenchymal states (Figure 21.C). Our results also stated that 4 days of TGFβ3 treatment was sufficient to start EMT, consequently further extension of TGFβ3 treatment to 10 days showed stronger mesenchymal transcriptional profile. With that, although, we identified the decrease on epithelial markers accompanied with an increase on mesenchymal markers, the decrease on CDH1 expression was not significant enough as the anticipated cadherin switch with less than 1-fold decrease and 2-fold increase on CDH1 and CDH2, respectively. Additionally, we performed extended treatment with TGFβ3 up to 22 days which demonstrated no additional decrease in CDH1 levels, suggesting a portion of the population persistently maintained CDH1 expression (Figure 21.D).

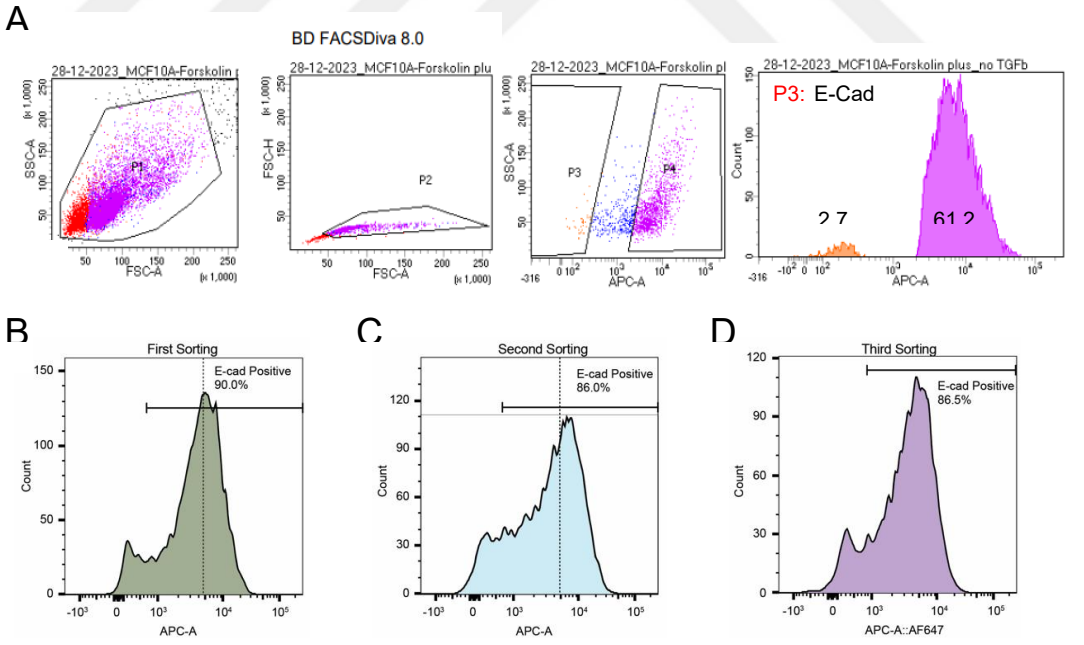

Figure 22. MCF10A Heterogeneity Persists Following Multiple E-Cadherin Sorting.
A) Flow cytometry plots representing gating strategy for E-Cad $^{(+)}$ and E-Cad $^{(-)}$ populations using anti-APC-E-Cad antibody on a BD FACSAria III. Flow cytometry analysis showing the percentage of cells expressing membrane-bound E-Cadherin in B) E-Cad $^{(+)}$ C) E-Cad $^{(++)}$ and D) E-Cad $^{(+++)}$ cells. Cells were stained with anti-APC-E-Cad antibody and analysed using FlowJo.

Furthermore, we used flow-cytometry to reveal the percentage of each subgroup expressing E-Cadherin on the plasma membrane and tried to homogenize the population by flow sorting by membrane bound Anti-APC-E-Cad antibody by BD FACSAria III. Rigorous gating strategy is applied to be able to sure about purity of the sorted cells by taking only 61.2% of the E-Cad (+) cells (Figure 22.A). Our results showed that, even after three consecutive sorting of E-Cad (+) cells as we measured 90% E-Cad positivity after initial sorting followed by 86% on second sorting and 86.5% on third sorting (Figure 22.B). Between sorting experiments cells were incubated for 5 days recovery period.

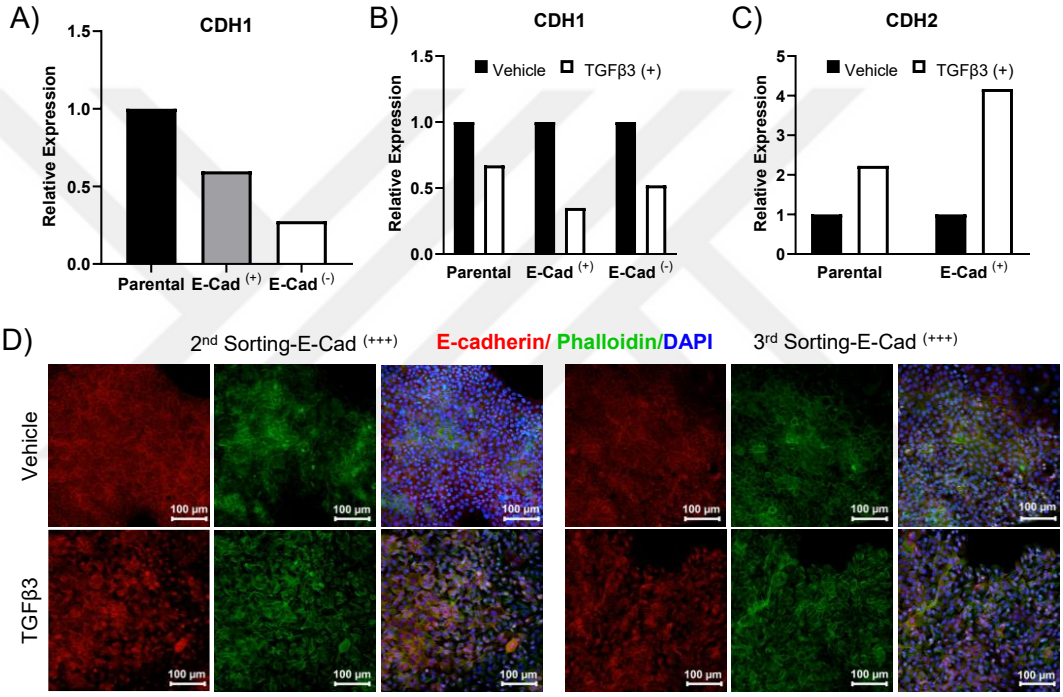

Figure 23. MCF10A Heterogeneity Persists on Transcriptional Level confirmed by qPCRs and Immunostaining.
A) The qPCRs showing the expression of CDH1 for parental, E-Cad (+) and E-Cad (-) cells. B) The expression of CDH1 following TGFβ3 treatment for parental and sorted populations. C) qPCR showing the increase on CDH2 expression after TGFβ3 treatment with comparison of parental to E-Cad (+) cells (*$p < 0.05$, **$p < 0.01$, ***$p < 0.001$). D) Immunofluorescence analysis of E-Cadherin, actin stress fibres are indicated by phalloidin staining and nuclei were counterstained with DAPI in MCF10A cells levels in response to TGF-β3 treatment for parental and CDH1 (+++) cells. TGFβ3 treatment was initiated immediately after sorting, without passaging.

After each sorting, cells are also plated into 6 well plates for maintenance and further exploration of vehicle cells and for TGFβ3 treatment immediately to eliminate any effects associated with passaging. Then, CDH1 levels were analysed by qPCR for both parental, E-Cad $^{(+)}$ and E-Cad $^{(-)}$ cells in vehicle state after one passage and for parental and E-Cad $^{(+)}$ cells upon TGFβ3 treatment without passaging. However, our results showed that CDH1 levels reduced back to parental state, even slightly

further reduced possibly due to cell death and stress caused by sorting (Figure 23.A). Furthermore, when TGFβ3 treated and vehicle cells compared, we observed slightly better decrease of approximately 1-fold on CDH1 levels accompanied by 2-fold increase on CDH2 levels for E-Cad $^{(+)}$ cells. However, further passaging of the cells, resulted in same response of parental CDH1 levels and similar TGFβ3 response (Figure 23.B-C). Immunostaining of 2nd (E-Cad $^{(++)}$) and 3rd sort (E-Cad $^{(+++)}$) samples also confirmed that heterogeneity consists after consecutive sorting as both cells that have E-Cad on the membrane and cytoplasm and lack of expression observed (Figure 23.D).

4.8. TGFβ3-Induced EMT in Single-Cell Derived MCF10A Clones Reveals Persistent Morphological and Cytoskeletal Heterogeneity

To determine whether the observed heterogeneity in MCF10A cells is an intrinsic characteristic or population-level variation, we performed clonal expansion of single cells sorted based on E-Cadherin expression (either positive or negative) from a second-sorted population (E-Cad $^{(++)}$). As described in Figure 24, a total of 1 × 10^{6}

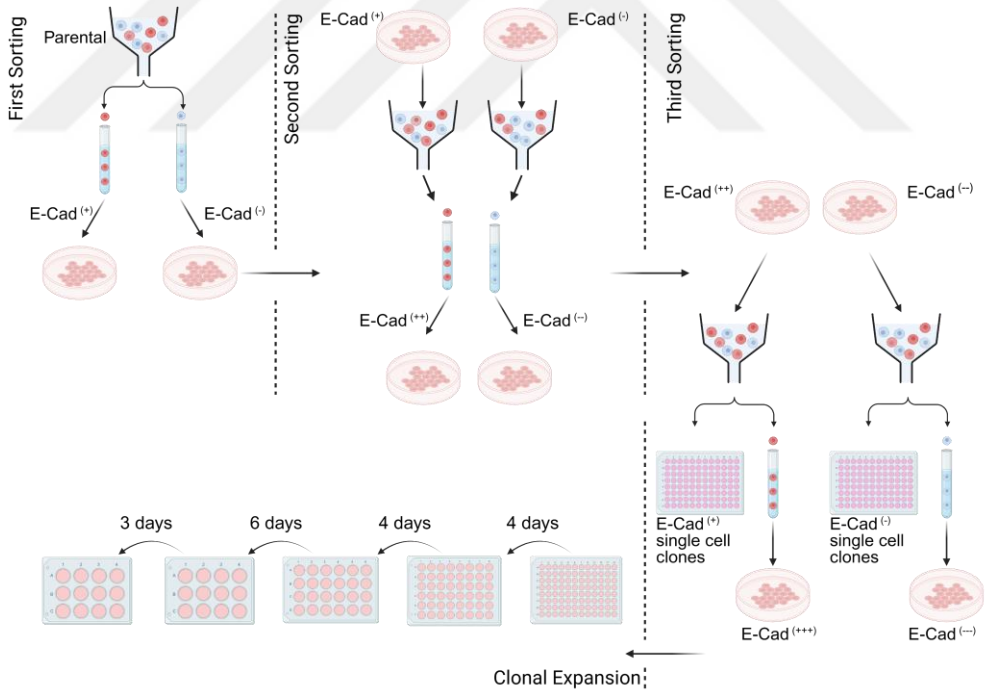

Figure 24. Schematic representation of sorting strategy and the experimental design for clonal expansion of single cell derived populations.
Cells were first sorted by FACS based on CDH1 expression and cultured separately to establish E-Cad (+) and E-Cad (-) populations (Step 1). These populations were then individually expanded and re-sorted without passaging to enrich for subpopulations (Step 2). A third sorting experiment performed to further enrich the population and both bulk and single cells were collected. Single cells from each enriched population were seeded into 96-well plates to allow clonal expansion (Step 3). Expanded clones were transferred sequentially to larger culture formats (96-well to 6-well plates) for expansion and downstream analysis (Step 4).

cells were dissociated using 0.25 µM EDTA and passed through a 70 µm cell strainer (SPL Life Sciences, 93070) to obtain a single-cell suspension. The cells were then incubated with Anti-human E-Cadherin-APC antibody (R&D Systems, FAB18381A) at a concentration of 10 µl per 1 × 10^6 cells for 1 hour at room temperature. Following incubation, cells were washed twice with PBS and resuspended in FACS buffer containing 5% horse serum in PBS. Using a BD FACSAria III cell sorter, CDH1-positive and -negative populations were isolated as single cells into 96-well plates, starting from an initial population of 10 × 10^6 cells.

The growth of individual clones was monitored over 18 days using the Solentim Cell Metric imaging system (Solentim, Dorset, UK) (Figure 25), after which successfully expanded clones were further cultured. Out of 96 single cells sorted from each condition, E-Cadherin-negative cells showed a higher colony formation rate than the E-Cadherin-positive ones (Figure 26.A).

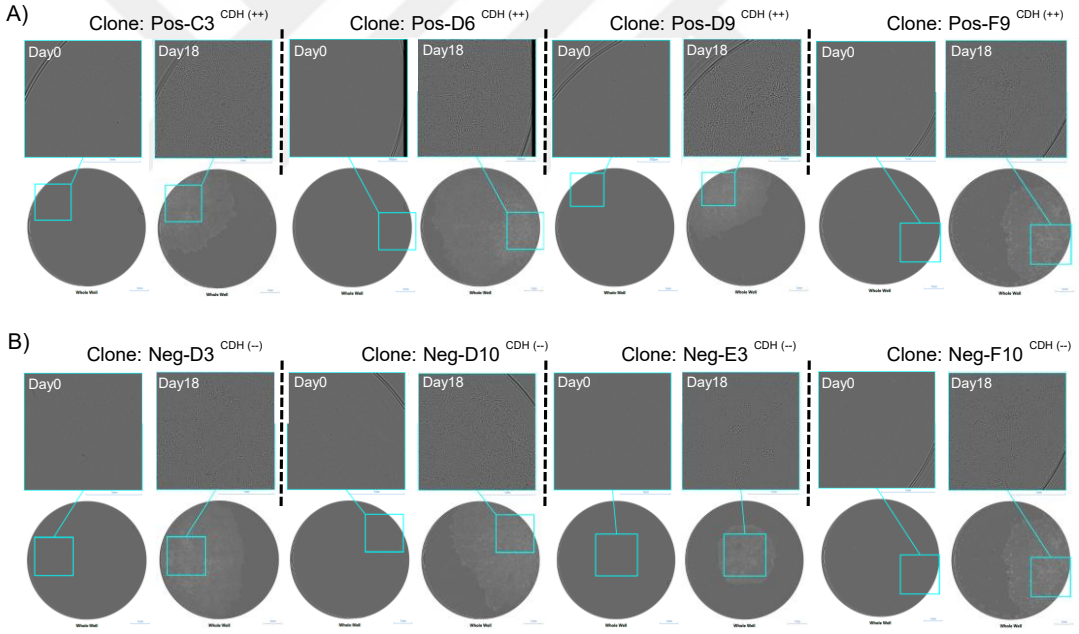

Figure 25. Representative images of clonal growth patterns depicting epithelial and mesenchymal phenotypes for A) CDH $^{(++)}$ and B) CDH $^{(--)}$ single-cell derived MCF10A Clones.

After clonal expansion to 6-well stage, fully confluent clones were re-analysed by flow cytometry. Interestingly, colonies derived from E-Cadherin-positive cells largely retained their original phenotype, with ~90% of cells remaining E-Cadherin positive (Figure 26.B), suggesting persistent heterogeneity even after clonal selection.

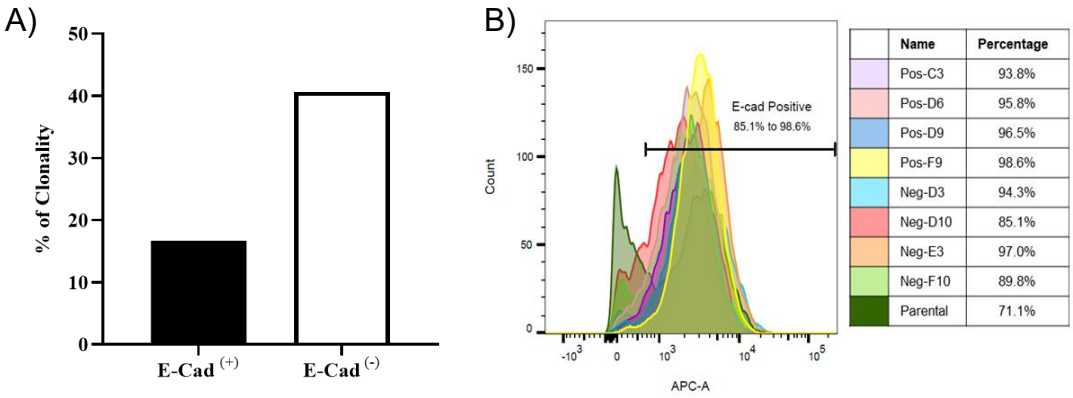

Figure 26. Clonality and E-Cadherin levels of single cell clones.
A) Clonality of single cells sorted as E-Cadherin-positive or -negative was quantified during the 96-well clonal expansion phase using data from the Cell Metric system. (B) Flow cytometry results illustrating the proportion of cells expressing membrane-localized E-Cadherin in clones derived from single E-Cad $^{(+)}$ or E-Cad $^{(-)}$ cells.

This observation indicates that membrane-bound E-Cadherin can be restored in cells that initially lacked its detectable expression, potentially through renewed expression or redistribution of cytoplasmic E-Cadherin to the membrane. These results demonstrate that MCF10A cells are capable of regenerating E-Cadherin-positive populations even after attempts to isolate them by FACS, implying that the observed heterogeneity is not temporary but rather a consistent and inherent characteristic of this cell line. To assess whether this inherent heterogeneity impacts

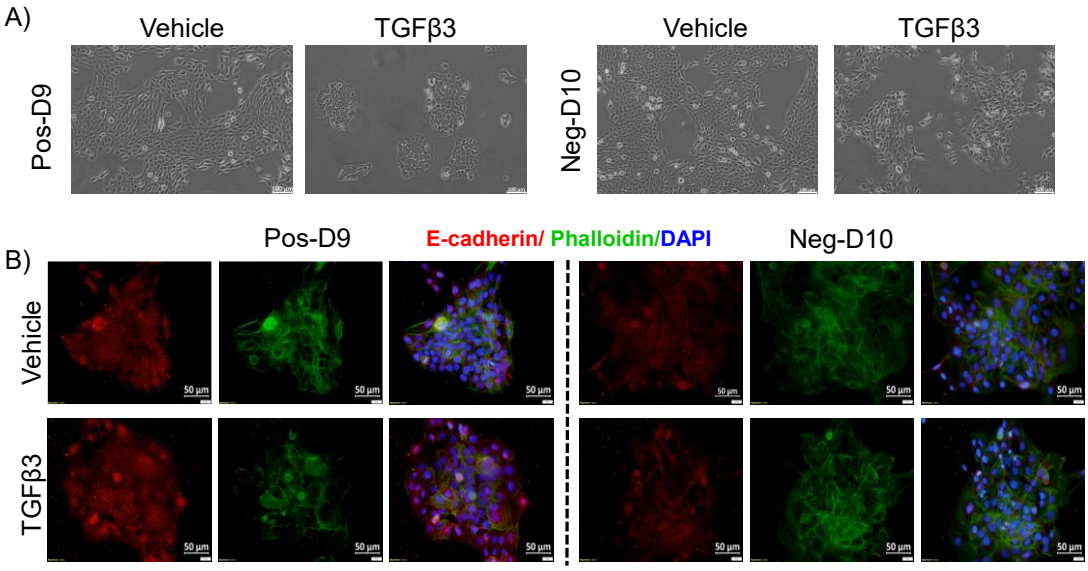

Figure 27. Single-Cell Derived MCF10A Clones Undergoing EMT Exhibit Persistent Transcriptional Heterogeneity.
A) Phase contrast images showing epithelial and mesenchymal morphologies of selected single cell derived MCF10A clones following 4 days of TGFβ3 treatment. B) Immunofluorescence staining of E-Cadherin and actin stress fibres (phalloidin) in single-cell derived MCF10A clones treated with TGFβ3 directly for 4 days. Nuclei were counterstained with DAPI.

EMT responsiveness, we investigated how these sorted populations respond to TGFβ3 treatment. To gain insights into transcriptional EMT responses within these cells, we treated the single-cell-derived clones along with the parental line and bulk-sorted populations with TGFβ3. Bright-field and immunofluorescence imaging revealed partial EMT across the cells like Parental cells further supporting that this heterogeneity is maintained at the clonal level with certain areas retaining E-Cadherin at the plasma membrane along with F-actin stress fibres, as confirmed by confocal microscopy (Figure 27.A-B).

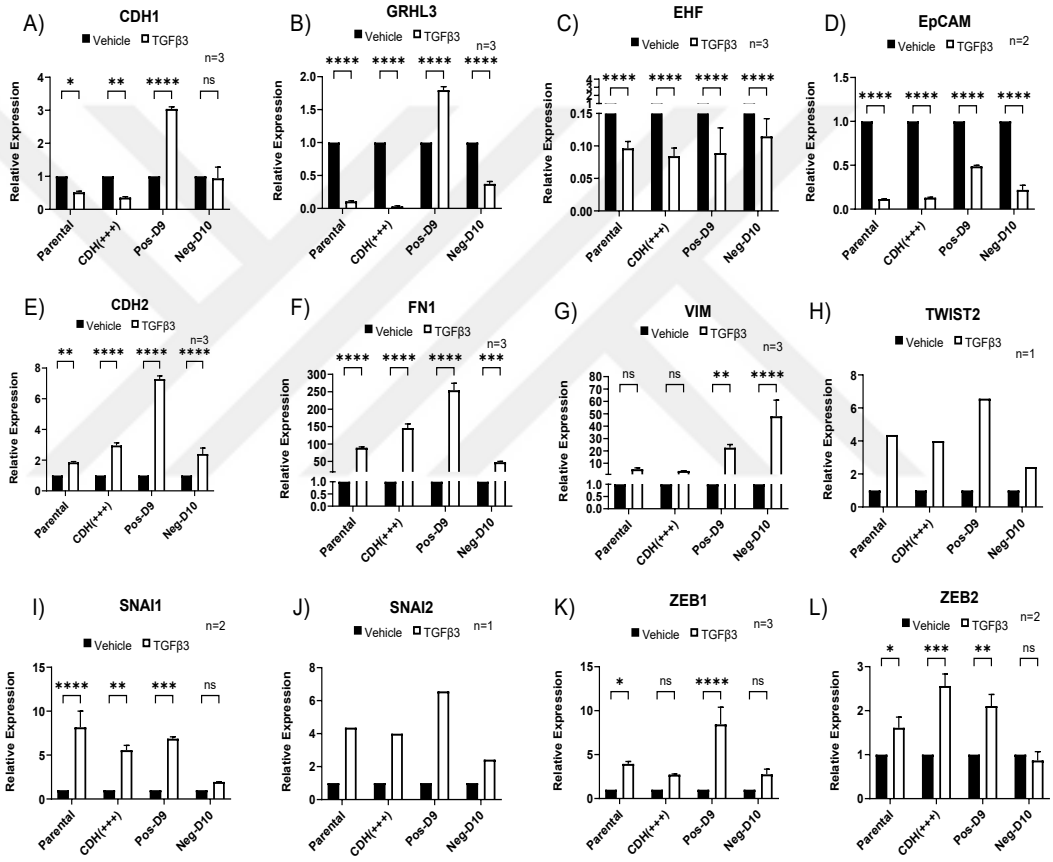

Figure 28. MCF10A Cells Show Persistent Heterogeneity After Clonal Expansion of Cells.
The qPCRs showing the expression of A-D) epithelial markers and E-L) mesenchymal markers for parental, bulk sorted (E-Cad (+++) and E-Cad positive and E-Cad negative single cell clones. (*p < 0.05, **p < 0.01, ***p < 0.001, ****p < 0.0001)

To analyse if clonal expansion eliminates this inherent heterogeneity on RNA level, we performed qPCR for several EMT-related markers. Among these, CDH1 downregulation was more pronounced in the bulk-sorted cells compared to the parental cells (Figure 28.A). In contrast, several single-cell-derived clones responded differently to TGFβ3. Most interestingly, E-Cad positive-sorted clones showed an unexpected upregulation of CDH1 (Figure 28.A). Among epithelial markers, GRHL3 showed a response pattern similar to CDH1, with increased expression in Pos-D9, while it was downregulated in all other clones (Figure 28.B). EHF and EpCAM were consistently downregulated across all comparisons (Figure 28.C-D). Among mesenchymal markers, CDH2 increased 2-3-fold in parental, bulk, and Neg-D10 cells and showed even stronger induction in Pos-D9 (Figure 28.E). FN1, VIM, TWIST2, SNAI1, SLUG, ZEB1 and ZEB2 (Figure 28.F-L) exhibited strong upregulation in most samples, indicating that EMT-associated transcriptional programs were properly activated. Except, there was no upregulation of ZEB2 and slight changes on FN1 and VIM in Neg-D10 (Figure 28.L, Figure 28.F-G).

These findings indicate that the initial membrane-bound E-Cadherin status does not consistently predict how cells will respond transcriptionally to TGFβ3. For example, the Neg-D10 clone, which was originally sorted as E-Cadherin-negative, expressed CDH1 mRNA and later restored membrane-localized E-Cadherin upon expansion. This clone also showed strong upregulation of VIM and FN1, though changes in other mesenchymal markers were relatively modest.

We reasoned that the heterogeneity of the population and stable expression of E-Cadherin even after TGFβ3 treatment might be related with different signalling conditions because our use of Forskolin on growth medium which was different than routine culture conditions of MCF10A which requires cholera toxin. We next investigated that if the lack of cholera toxin which is a major supplement of regular MCF10A media known to have effects on mammary cell growth, elevating cAMP or Forskolin as its substitute as cAMP signalling inducer has any effects on E-Cad expression, population structure, EMT response and cell growth dynamics [28].

4.9. Forskolin Affects TGFβ3-Induced Epithelial-to-Mesenchymal Transition in MCF10A Cells at Morphological and Molecular Levels

First, we examined the cells to analyse the localization of E-Cad. We used immunostaining to reveal whether E-Cadherin is on the plasma membrane or at cytoplasm for Fsk $^{(-)}$ and Fsk $^{(+)}$ cells after extended, 10 days of TGFβ3 treatment to have a clear understanding. Immunostaining analysis identified E-Cadherin at cytoplasm with reduced number of cells having E-Cadherin expression at plasma membrane for TGFβ3 treated samples for both Fsk $^{(-)}$ and Fsk $^{(+)}$ cells. Furthermore,

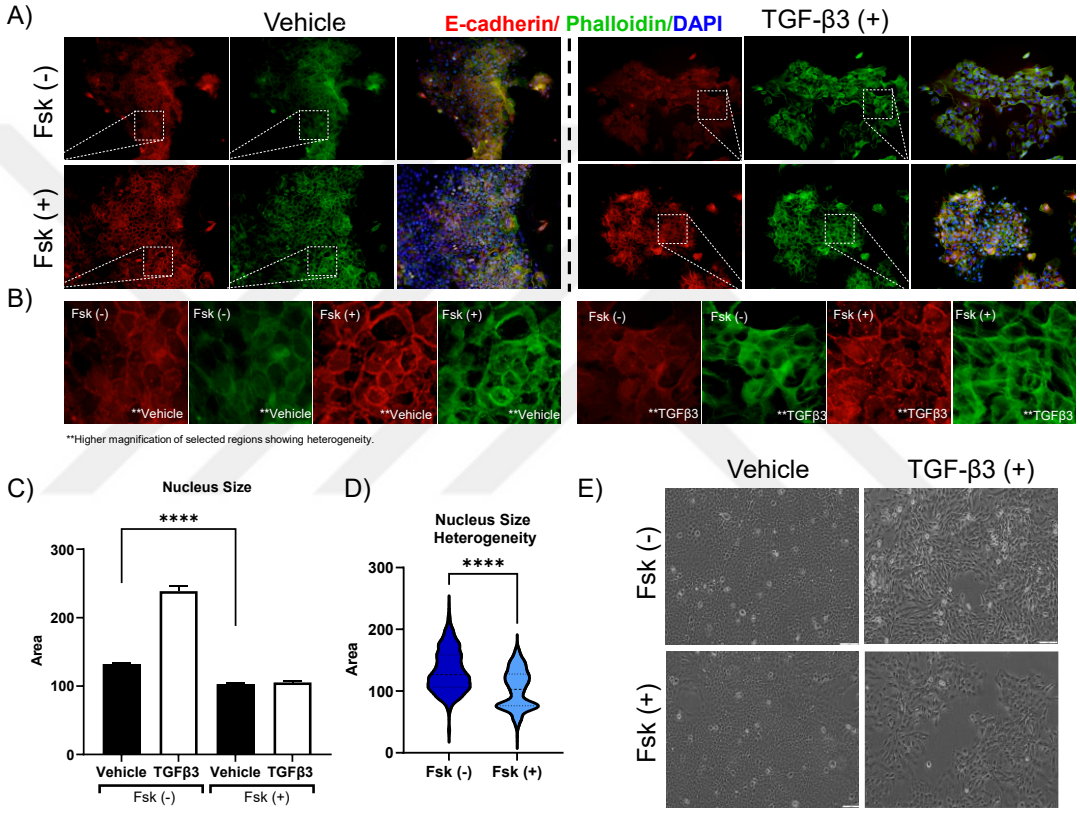

Figure 29. The effect of Fsk treatment on TGFβ3-mediated EMT in MCF10A cells, exploring changes in cellular behaviour and phenotype.
A) Confocal images visualizing morphological changes and localization and levels of E-Cad and actin stress fibres are indicated by phalloidin staining in Fsk $^{(+)}$ and Fsk $^{(-)}$ cells with and without TGF-β3 treatment. B) Magnified images of selected regions indicating the cellular heterogeneity within the slide. C-D) Histogram and Violin plot showing the nucleus size (μm^2) with highly significant pattern (****, $p<0.0001$) of bigger area and higher heterogeneity on Fsk $^{(-)}$ samples calculated by DAPI. E) Phase-contrast images comparing the morphologies of Fsk treated and untreated cells in response to TGFβ3 treatment. (*$p < 0.05$, **$p < 0.01$, ***$p < 0.001$, ****$p < 0.0001$)

results found to be correlating with distribution of F-actin, demonstrated by Phalloidin staining (Figure 29.A-B). Previous research showed that MCF10A cell line contains morphologically more heterogeneous population of cells with higher cell size and shape irregularities [79]. We investigated the differences between cellular size regarding Fsk treatment for both vehicle and TGFβ3 treated cells.

Accordingly, we measured the average nuclear area by Image J software using DAPI staining. Our results showed that Fsk treated cells showing highly significant smaller area with wide range of different nuclear size (Figure 29. C-D). This result indicates that Fsk treatment might be a good candidate for reducing variability thus heterogeneity of the population. Additionally, we confirmed our approach by phase contrast microscopy to assess morphological changes distinguishing the effect of treatment.

Our results showed, slightly different and more epithelial morphology on Fsk treated (Fsk $^{(+)}$) cells and more mesenchymal morphology on TGFβ3 treated Fsk $^{(+)}$ cells compared to Fsk $^{(-)}$ counterparts such as switch from cobblestone to spindle-like morphology and tight to lose cellular contacts (Figure 29.E).

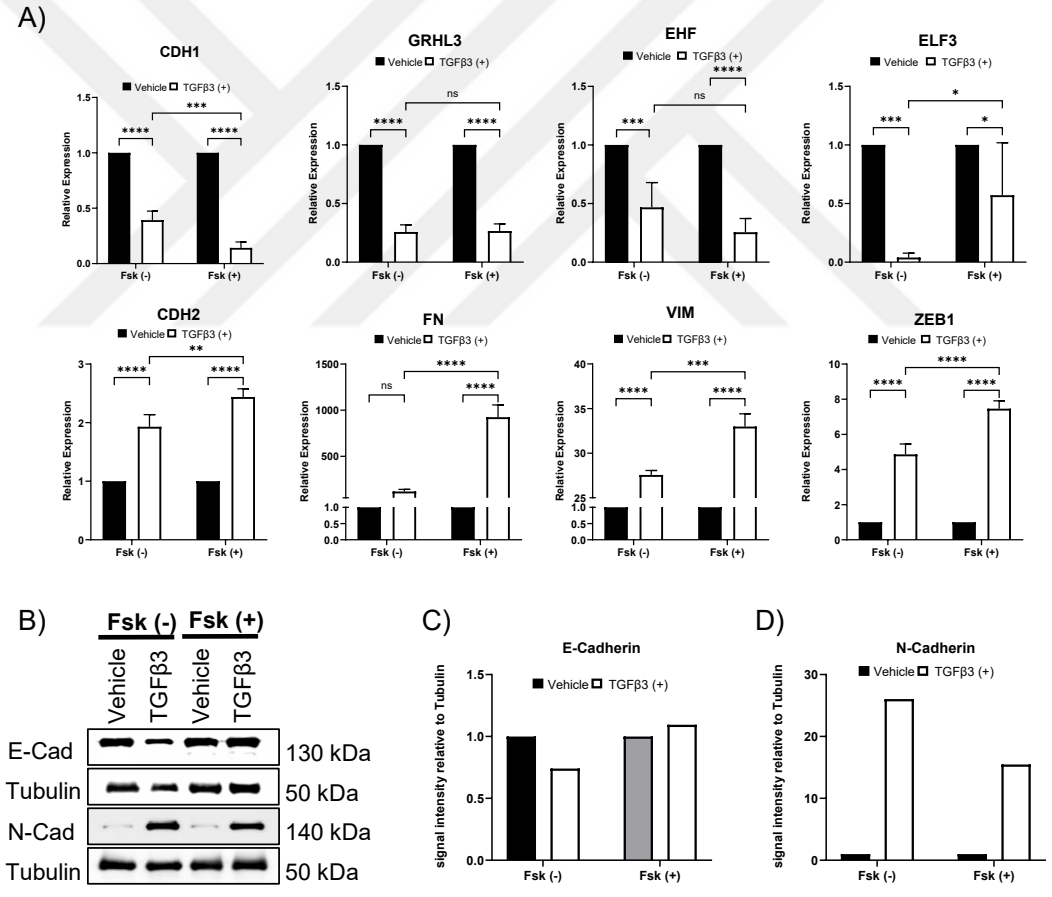

Figure 30. The effect of Fsk treatment on transcriptional and protein level for TGFβ3 mediated EMT in MCF10A cells, exploring changes by qPCR and western blots.
A) qPCR analysis showing the expression of epithelial (CDH1, GRHL3, EHF, ELF3) and mesenchymal (CDH2, FN1, VIM, ZEB1) markers. B) Western blots representing E-Cad and N-Cad expression with and without Fsk treatment after 10 days of EMT by TGFβ3 induction C) Quantified by image-J. (*p < 0.05, **p < 0.01, ***p < 0.001, **** p < 0.0001, where n=3)

Then, we checked the effect of Fsk on mRNA and protein levels for further understanding. Fsk treatment showed slight difference at the basal levels of CDH1, accompanied by a significant difference for Fsk $^{(-)}$ and Fsk $^{(+)}$ cells by approximately 35% higher decrease on Fsk $^{(+)}$ on TGFβ3 induced EMT for mRNA levels with high significance (***, p<0.001).

Additionally, it elevated the percentage of decrease in epithelial markers such as GRHL3 and EHF while ELF3 showed stronger downregulation on Fsk (-) cells. These changes accompanied by the increase on the mesenchymal markers including CDH2, FN1 and ZEB1 (Figure 30.A). Our results showed, higher increase of mesenchymal markers with approximately 5-fold difference for FN while VIM and ZEB1 changing 2-fold from Fsk treated to untreated cells after TGFβ3 treatment (Figure 30.A). Then, we further expanded our research to protein level. Western blots indicated no significant change on E-Cadherin levels while N-Cadherin levels showed higher increase on Fsk $^{(-)}$ cells after TGFβ3 treatment while nearly no N-cadherin protein was detectable at vehicle state for both cells (Figure 30.B).

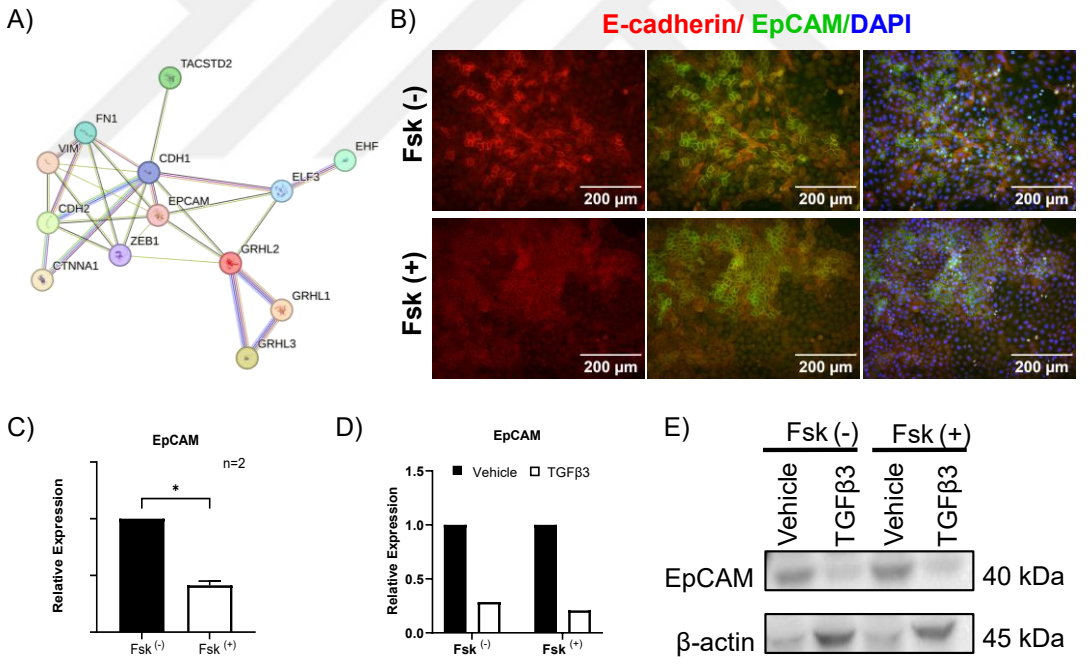

Figure 31. Comprehensive Analysis of EpCAM Expression, EMT Marker Associations, and Cellular Heterogeneity in MCF10A Cells under Fsk Treatment.
A) STRING analysis of protein-protein interactions shows EpCAM related DEGs associated with EMT markers; FN1, VIM, ZEB1, ELF3, EHF, GRHL3. B) Immunofluorescence analysis of EpCAM and E-Cadherin, nuclei were counterstained with DAPI in Fsk $^{(+)}$ and Fsk $^{(-)}$ MCF10A cells. C-D) qPCR analysis measuring the expression of EpCAM, showing a significant downregulation in response to treatment with Fsk (Fsk $^{(+)}$), compared to untreated control (Fsk $^{(-)}$) E) Western blots showing EpCAM expression relative to β-actin on vehicle and TGFβ3 induced cells. (*p < 0.05, **p < 0.01, ***p < 0.001, ****p < 0.0001)

4.10. EpCAM Expression Dynamics Under Forskolin Treatment Reveal Distinct Subpopulations and Their Association with EMT in MCF10A Cells

Based on these observations, we wanted to explore population level differences by using additional surface markers. Among these, we used EpCAM, which is as a key epithelial marker, to gain a more understanding of the changes and level of heterogeneity within the population. Prior to the detailed analysis, we checked protein interaction network by STRING for EpCAM and EMT related genes. Analysis supported that there is strong correlation between EpCAM and EMT-related genes such as CDH1, CDH2, ELF3, FN1, VIM and a sequential relation with GRHL3, EHF and ZEB1 (Figure 31.A).

To evaluate the effect of Fsk treatment on EpCAM, we first analysed by E-Cadherin and F-actin immunostaining to analyse if CDH1 $^{(+)}$ cells are concurrently expressing EpCAM (Figure 31.B). Analysis showed that, our population have multiple different phenotypes in terms of CDH1 and EpCAM positivity. However, although we identified a slight increase in the double positive cell's immunostaining was not enough to conclude the effect of Fsk treatment on EpCAM. To have a better understanding of Fsk treatment on EpCAM levels and EMT process, both Fsk $^{(-)}$ and Fsk $^{(+)}$ cells treated with TGFβ3 (5 ng/ml) for 10 days and subsequently analysed by qPCR for EpCAM expression (Figure 31.C). Our results showed that, there is a significant decrease in EpCAM levels on Fsk $^{(+)}$ cells at basal state, accompanied by a slightly significant decrease of EpCAM expression on Fsk $^{(+)}$ cells compared to Fsk $^{(+)}$ cells after TGFβ3 treatment (Figure 31.C-D). Results were also correlating when it is further extended to protein level by western blots performed by EpCAM antibody for both Fsk $^{(-)}$ and Fsk $^{(+)}$ cells treated with and without TGFβ3 (Figure 31.E).

After we confirmed EpCAM as a good candidate, we conducted a flow cytometry analysis to determine the expression level differences of EpCAM among population. Our results showed that population consists of 61.6% EpCAM (+) cells, while 25.9% of the population doesn't have the expression of EpCAM (Figure 32.A). By using strict gating strategies, cells were sorted as EpCAM (+) and EpCAM (-) and cultured for 4 days with TGFβB, meanwhile another set of cells is collected directly after sorting for qPCR analysis to compare the effect of passaging on EpCAM expression of sorted cells. qPCR cells clearly demonstrated that CDH1 levels are significantly elevated on EpCAM positive cells compared to parental cells with slight decrease following passaging while EpCAM (-) sorted cells didn't show distinct

differences on CDH1 levels (Figure 32.B). We also observed that, although CDH1 levels slightly decrease after passaging in EpCAM (+) cells, membrane-bound EpCAM expression remained stable (Figure 32.C).

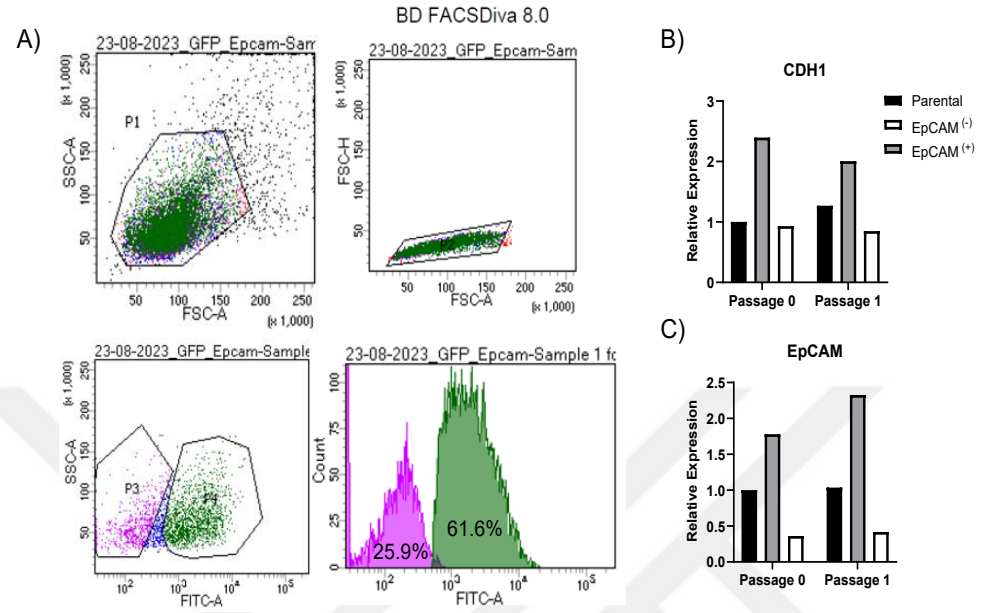

Figure 32. EpCAM Expression Highlights the Presence of Distinct Subpopulations Within the MCF10A Population.
A) Flow cytometry plots representing gating strategy for EpCAM $^{(+)}$ and EpCAM $^{(-)}$ populations using anti-FITC-EpCAM antibody on a BD FACSAria. B) qPCR analysis showing EpCAM and CDH1 expression levels in sorted EpCAM $^{(+)}$ and EpCAM $^{(-)}$ cells following sorting by Anti-EpCAM-FITC directly after sorting and after one passage. C) Flow cytometry results for CDH1 and EpCAM markers for Parental and EpCAM sorted cells under different Fsk conditions.

4.11. Dual CDH1 and EpCAM Sorting Reveals Enhanced Resolution of Epithelial Heterogeneity and EMT Dynamics in MCF10A Cells

Following these results, we wanted to apply a dual sorting strategy with using both E-Cadherin and EpCAM antibodies in parental MCF10A cells before and after treatment with TGFβ3 (Figure 33.A). Analysis revealed that E-Cadherin expression on the plasma membrane is affected with and without Fsk treatment for TGFβ3 induction by 10% higher decrease with Fsk treatment. 4 subgroups were identified that expresses CDH1 and stemness marker EpCAM of different levels. Meanwhile, the results of basal E-Cadherin levels of vehicle cells showed that the heterogeneity of the population have been reduced by Fsk treatment with 90 % of the cells are expressing E-Cadherin on the membrane with Fsk treatment while only 70% is expressing if not treated with Fsk.

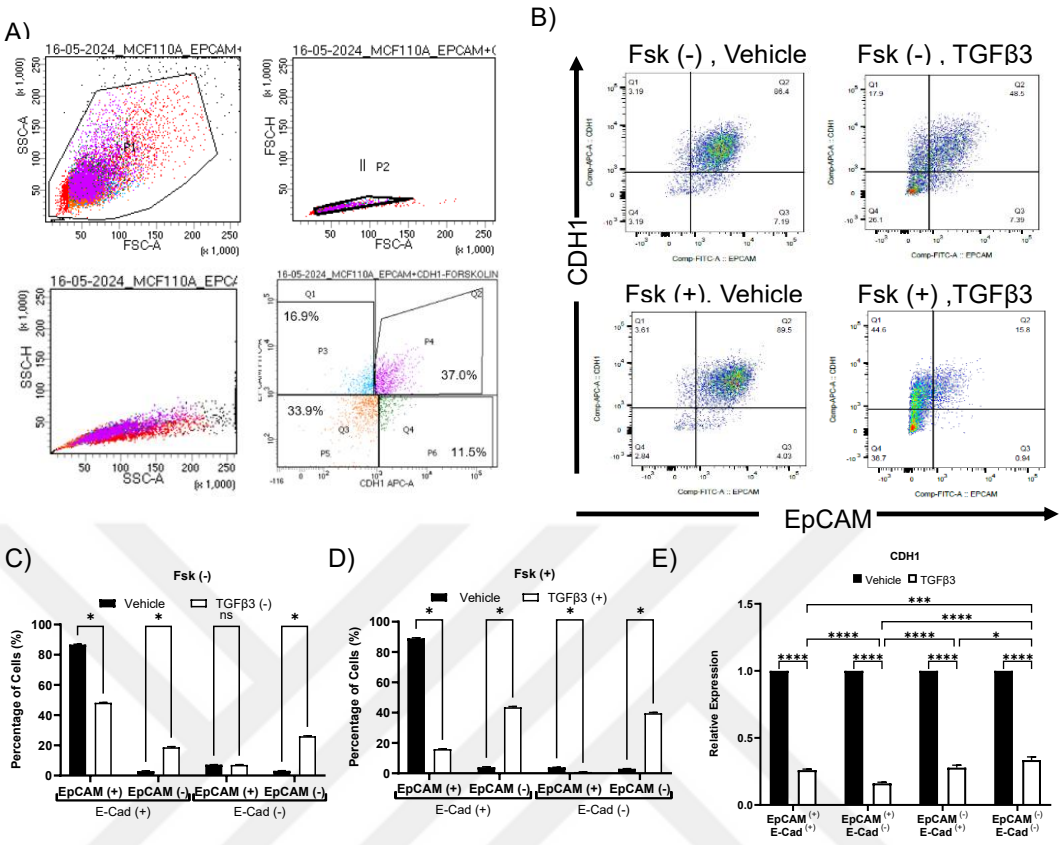

Figure 33. Combined CDH1 and EpCAM Sorting Provides Higher Resolution on Landscape of Cellular Heterogeneity in MCF10A Cells.
A) Flow cytometry plots representing gating strategy for dual sorting with anti APC-Ecadherin and anti-FITC-EpCAM antibodies on a BD FACSAria. C) Flow cytometry results for CDH1 and EpCAM markers for Parental cells under different Fsk conditions with and without TGFβ3 treatment. The cells are stained and compensated with anti-APC-E-Cad and Anti-FITC-EpCAM antibodies. C-D) Summary of population distribution based on CDH1 and EpCAM Expression in Parental Cells under Fsk and TGF-β3 treatment conditions. E) qPCRs representing CDH1 expression upon TGFβ3 treatment for 4 sub-populations. (*p < 0.05, **p < 0.01, ***p < 0.001, ****p < 0.0001)

Among these populations EpCAM$^{(+)}$/E-Cad$^{(+)}$ population decreased from 89.5% to 15.8% following 4 days of TGFβ3 treatment while EpCAM$^{(-)}$/E-Cad$^{(+)}$ and EpCAM$^{(-)}$/E-Cad$^{(-)}$ population increased from 3.61% to 44.6% and 2.84% to 38.7% suggesting an overall decrease of EpCAM (+) population while E-Cad expression changed variably (Figure 33.B-D). Furthermore, we performed qPCR analysis in 4 subpopulations sorted populations following TGFβ3 treatment. Our results showed that all subpopulations showed similar response to TGFβ3 with slight differences including lowest response in EpCAM-/E-Cad- cells and strongest decrease is observed in EpCAM+/E-Cad- group compared to other groups (Figure 33.E).

4.12. MCF10A cells gain increased proliferation rate by Fsk treatment

The effect of Fsk were further studied to evaluate if the decrease of E-Cadherin is sufficient to understand the effect on TGFβ3 induced EMT from the perspective of cells health and growth. To further explore the effects of Fsk treatment on growth profile, we analysed the distribution of cell cycle, based on DNA-content by PI staining. Our results showed that the majority of the cells are distributed at G1 phase with more than 60%, followed by S (>19.3%) and G2/M (>13.5) phases (Figure 34.A-B).

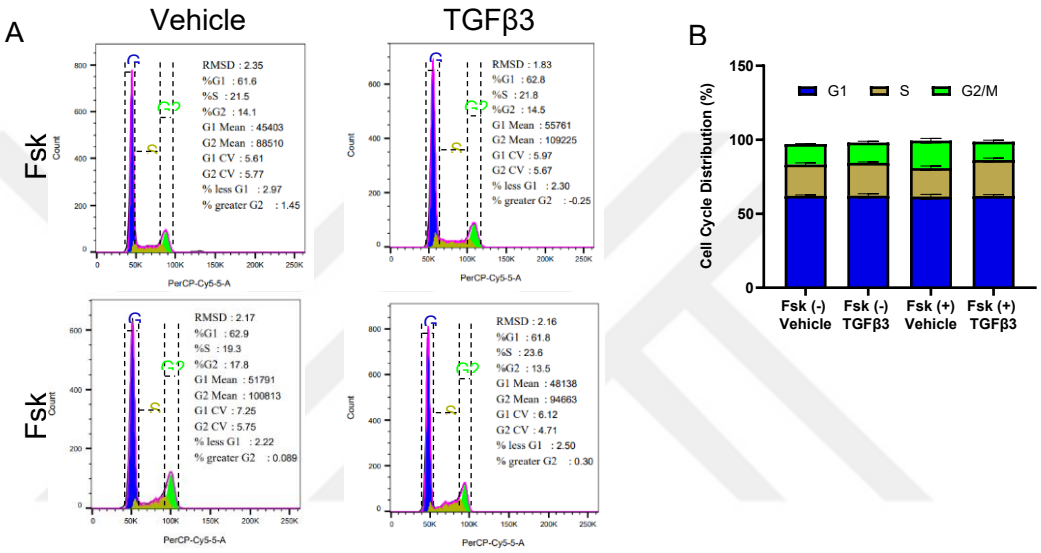

Figure 34. DNA Content Analysis Reveals No Significant Differences in Cell Cycle Distribution Related to Forskolin Treatment.
A) DNA content/cell-cycle analysis of induced EMT and vehicle Fsk $^{(+)}$ and Fsk $^{(-)}$ cells B) Percentage of cell cycle distribution.

However, no significant difference is detected between Fsk treated and untreated samples as well as TGFβ3 induced and vehicle state for both samples. Our growth curve results showed that proliferation of MCF10A cells is enhanced by the presence of Fsk for both vehicle and TGFβ3 treated states predominantly after second day of the experiment. Fsk $^{(+)}$ cells showed significantly faster proliferation rate at vehicle state compared to Fsk $^{(-)}$ cells with similar pattern for both cells after TGFβ3 treatment (Figure 35.A).

To have better understanding of growth kinetics, the population doubling time is calculated for each cell at basal and TGFβ3 induced states. In concordance with growth curve data, proliferation rate of the cells was assessed by SrB assay and showed a similar trend of boosted proliferation rate for Fsk treated cells (Figure 35.B).

Our results showed that Fsk treatment resulted in significantly shortened doubling time, supporting increased growth rate (Figure 35.C).

Given that, we have encountered conflicting result of proliferation and cell cycle assays we further explored the genomic stability of the treated and non-treated groups for further hints of this inconsistency. Since the cells showed higher proliferation rates, which measured the metabolic activity and number of vital cells, without affecting the cell cycle, we hypothesized that this could be due to affected cell viability.

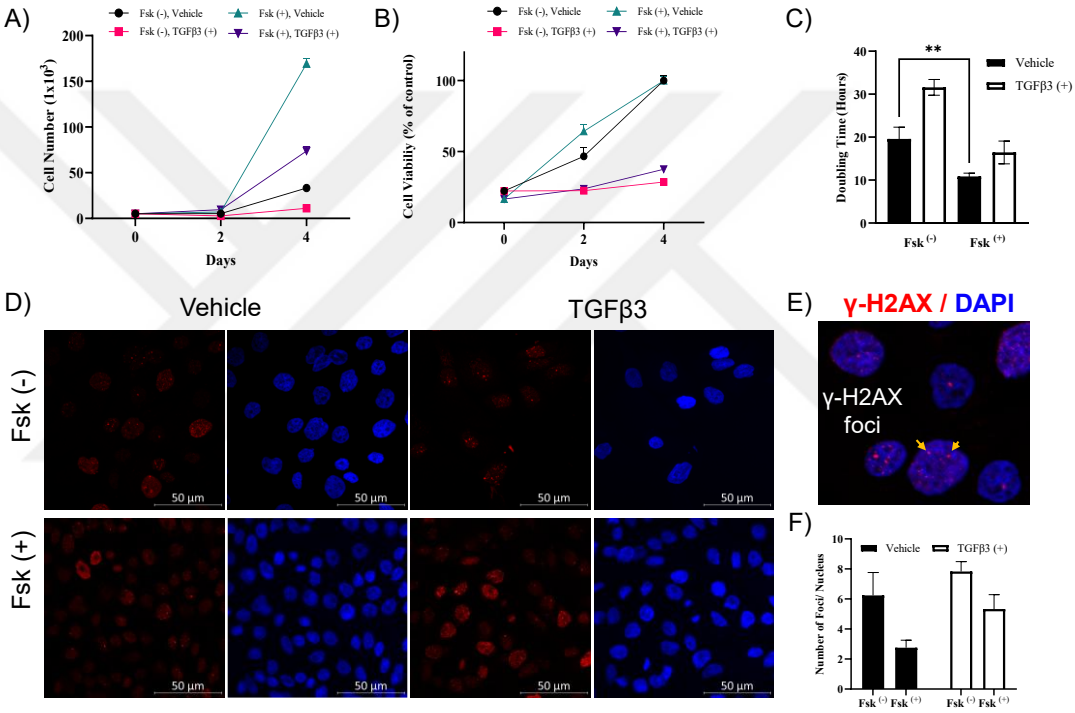

Figure 35. Proliferation and DNA damage analysis of Fsk $^{(+)}$ and Fsk $^{(-)}$ cells with and without TGFβ3 treatment.
A) Detailed representation of growth curves, starting with 5000 cells (1400 cells/cm² seeding density), with cell counts recorded every 2 days over a 4-day period. B) Sulforhodamine B (SrB) assay measuring cellular protein content as an indicator of cell growth over 4 days to assess cell proliferation in Fsk $^{(+)}$ and Fsk $^{(-)}$ MCF10A cells, with and without TGFβ3 treatment. C) Doubling time of Fsk $^{(+)}$ and Fsk $^{(-)}$ cells, demonstrating a significant decrease in doubling time following Fsk treatment, as calculated from growth curve analysis. D) Immunofluorescence analysis of γ-H2AX as an indicator of DNA-damage response, nuclei were counterstained with DAPI in Fsk $^{(+)}$ and Fsk $^{(-)}$ MCF10A cells. E) Representative image of γ-H2AX foci-count in Fsk $^{(-)}$ MCF10A cells. F) Distribution of foci as number of foci/nuclei for Fsk $^{(+)}$ and Fsk $^{(-)}$ MCF10A cell, with and without TGFβ3 treatment. (*p < 0.05, **p < 0.01, ***p < 0.001, ****p < 0.0001)

To explore the possible reasons of affected cell viability, we explored the genomic integrity by quantification of γH2AX positive loci in each group (Figure 35.D-E). Results showed that Fsk (-) cells possessed almost approximately 3 times more increase in the accumulation of γH2AX on vehicle state, indicative of high DNA

damage that might explain the conflicting results showing the increased genomic integrity leading to viability upon Fsk treatment (Figure 35.F). Together, our experiments showed significant variability in phenotypic and cellular responses including proliferation rates, morphological differences, response to DNA damage which shows an intrinsic heterogeneity within population.

4.13. TGFβ3 Treatment Reduces Transcriptomic Heterogeneity and Induces EMT-Associated Gene Expression in MCF10A Cells

To understand if this variability resulted from basal transcriptional differences, we performed RNA-sequencing on three control and two TGFβ3 treated MCF10A samples. Our results showed that according to principal component analysis (PCA), parental MCF10A transcriptomes vary divergently among replicates while TGFβ3 treated cells clustered closely that highlights even though there is baseline

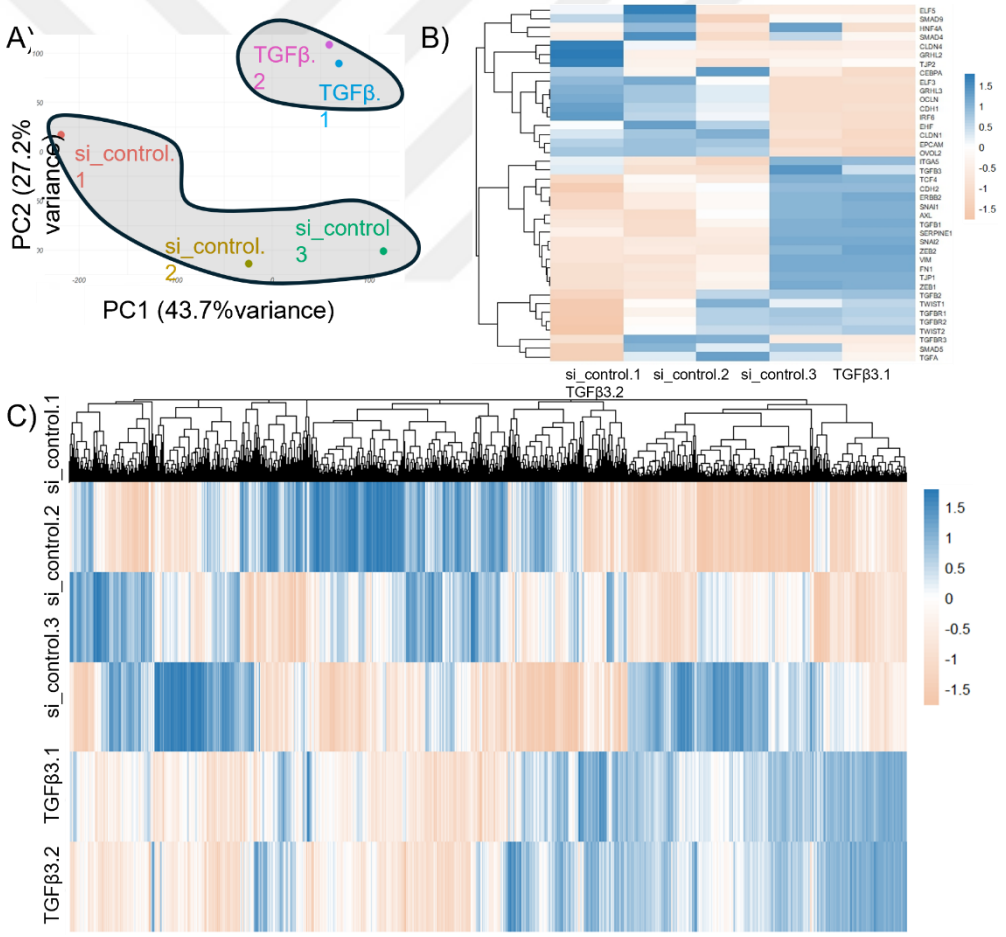

Figure 36. Transcriptomic profiling of parental and TGFβ3-treated MCF10A cells.
(A) Principal component analysis (PCA) of RNA-seq data from three untreated (parental) and two TGFβ3-treated MCF10A samples showing high variability among parental replicates, while TGFβ3-treated samples clustered closely. (B) Heatmap showing expression patterns of EMT-related genes across control and TGFβ3 treated samples. (C) Heatmap representing all DEGs demonstrating reduced heterogeneity following TGFβ3 treatment.

heterogeneity, it did not disrupt the detection of EMT-related effects (Figure 36.A). When, detailed differential analysis is explored in detail by heatmaps for both EMT-related genes (Figure 36,Figure 37.B) and all differentially expressed genes (Figure 36.C), results also demonstrated the decrease of heterogeneity following TGFβ3 treatment. These findings support the conclusion that baseline heterogeneity does not interfere the detection of EMT-related effects confirming the observed changes upon H3.3A depletion reflects specific role of H3.3A in the regulation of EMT.

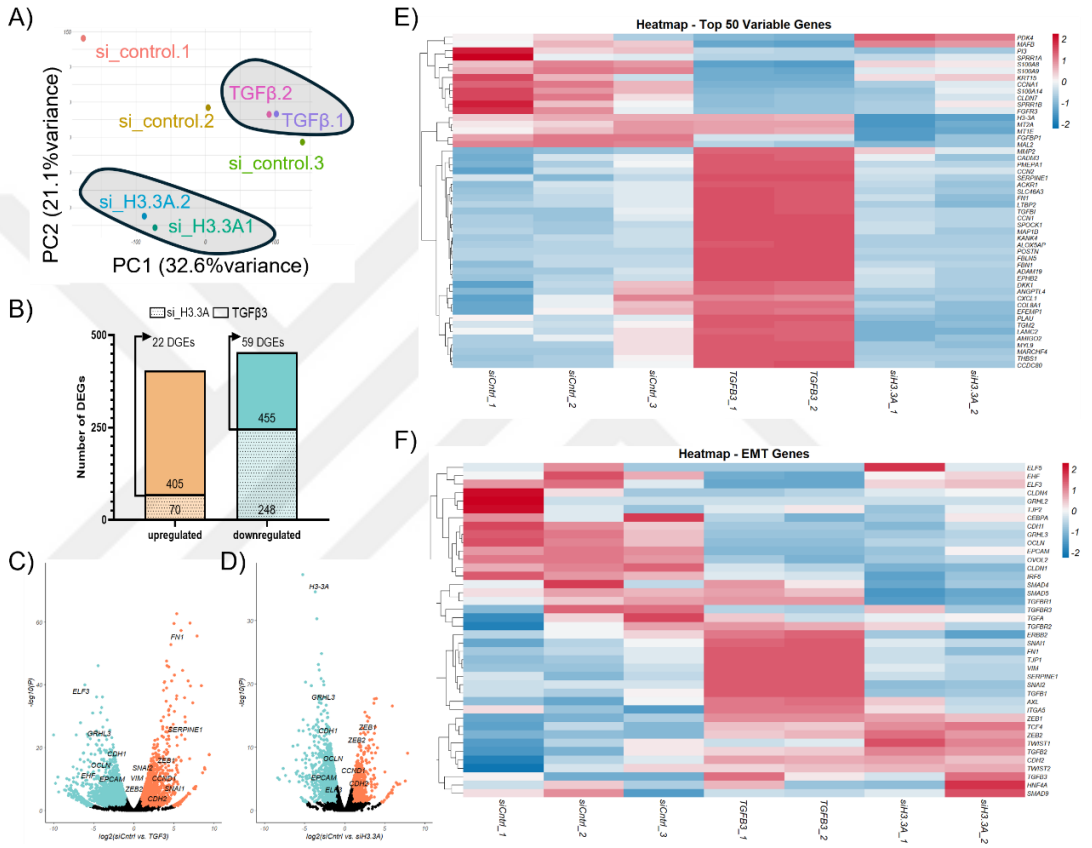

Figure 37. Transcriptomic alterations upon H3.3A knockdown and comparison with TGFβ3-induced EMT.
(A) Principal component analysis (PCA) of RNA-seq data from control, H3.3A knockdown, and TGFβ3-treated MCF10A cells reveals distinct clustering of H3.3A-depleted samples, indicating a unique transcriptional profile compared to other groups. (B) Bar plot showing the number of differentially expressed genes (DEGs) in H3.3A knockdown (442 genes) and TGFβ3 treatment (702 genes) including 22 commonly upregulated and 59 commonly downregulated genes, with selected EMT-related markers highlighted. C-D) Volcano plots displaying significantly upregulated and downregulated genes in H3.3A knockdown and TGFβ3-treated cells. EMT-related markers commonly affected in both conditions are highlighted, including CDH2 and ZEB1. E) Heatmap displaying the top 50 most significantly differentially expressed genes following H3.3A depletion, including EMT-related genes (TGFβ, FN1) and cell cycle regulators. F) Heatmap illustrating the expression profiles of a curated panel of EMT markers (listed in Table 7) in H3.3A knockdown and TGFβ3-treated cells.

4.14. H3.3A Depletion Drives EMT-Like and Cell Cycle Regulatory Changes with Overlapping and Distinct Features with Canonical TGFβ3 Response

Following these results, we further explored the role of H3.3A on transcriptional level following H3.3A knockdown. We first investigated the profile difference between control and H3.3A depleted cells, also by comparing TGFβ3 driven EMT through principal component analysis (Figure 37.A). PCA demonstrated that both H3.3A and TGFβ3 showed tight clusters with highly distinct transcriptional profile of H3.3A compared to other groups (Figure 37.A).

Next, we identified differentially expressed genes (DEGs) for H3.3A depletion and compared with TGFβ3 treatment. A total of 442 and 702 differentially expressed genes were identified for H3.3A knockdown and TGFβ3 treated cells, respectively (Figure 37.B).

Among these, 22 upregulated and 59 downregulated genes were identified as common between H3.3A knockdown and TGFβ3 treated cells including widely accepted mesenchymal and epithelial markers such as CDH2, ZEB1, and CDH1, EpCAM, ELF3, GRHL3, respectively, (Figure 37.C-D). To investigate the transcriptional profile of H3.3A depletion in detailed, a heatmap was generated representing top 50 most significant differentially expressed genes, highlighting transcriptional alterations on EMT markers such as TGFβ, FN1, and also included cell cycle regulation associated markers suggesting possible role of H3.3A not only on EMT but also on cell dynamics (Figure 37.E). To investigate the EMT related transcriptional response in detail, we generated heatmap for a panel of EMT markers listed in Table 1. The resulting heatmap demonstrated highly significant upregulation of CDH2, ZEB1, ZEB2, TWIST1, TWIST2 and downregulation of CDH1, GRHL3, EpCAM, OCLN representing the gain of mesenchymal identity and EMT-like phenotype although there are significant differences in the effected gene sets compared to TGFβ3 treatment which shows strong upregulation in FN1, SERPINE1, SNAI2, AXL while EHF, ELF3, ELF5 are the leading downregulated genes (Figure 37.F).

To have a broader look at the top enriched pathways, we performed Gene Set Enrichment Analysis (GSEA) for H3.3A depleted and TGFβ3 treated samples. Among top 10 most enriched pathways, epidermal cell differentiation, epidermis development and skin development were commonly downregulated for both H3.3A depletion and TGFβ3 induction while pattern specific processes and embryonic tube and epithelial

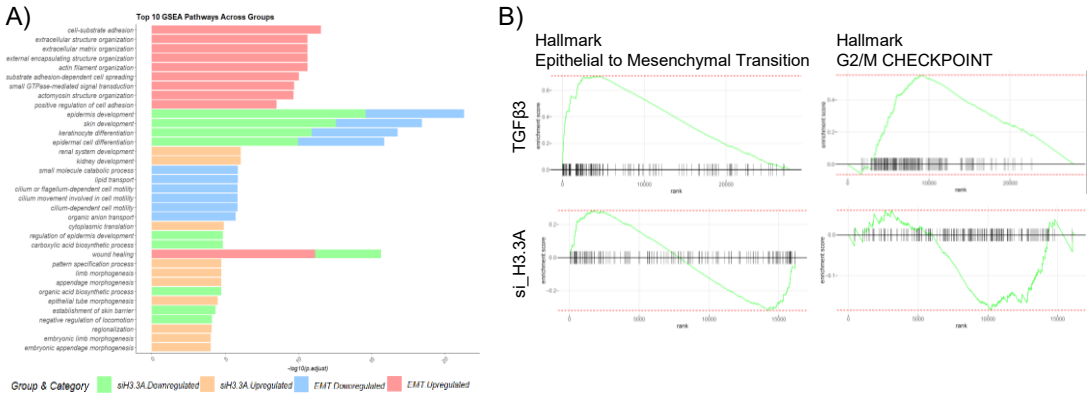

Figure 38. Gene Set Enrichment Analysis (GSEA) reveals distinct pathway enrichment profiles following H3.3A knockdown and TGFβ3 treatment.
A) Bar plot showing the top 35 significantly enriched gene sets (GO biological processes) identified by GSEA for H3.3A-depleted and TGFβ3-treated MCF10A cells. (B) Enrichment plots from the GSEA analysis showing representative hallmark gene sets for EMT, G2/M checkpoint, DNA repair, and TGFβ signalling.

tube morphogenesis were significantly upregulated only by H3.3A depletion while effect of TGFβ3 was more focused on actin filament and extracellular matrix organization motility and cell adhesion (Figure 38.A). To further explore in detail, enrichment plots were generated for hallmarks of EMT, G2/M checkpoint, DNA repair and TGFβ3 signalling highlighting difference in enriched pathways between H3.3A depletion and TGFβ3 induced EMT (Figure 38.B).

4.15. HIRA Knockdown Induces Variable EMT-Like Phenotypes and Transcriptional Reprogramming in MCF10A Cells Similar to H3.3A Depletion

Correspondingly, we investigated whether the observed phenotypic and transcriptional results of H3.3A knockdown is related to the efficient deposition of H3.3 into chromatin by the involvement of HIRA, the major chaperone responsible for H3.3 deposition. To understand this, we performed siRNA mediated knockdown by 4 different siRNA sequences targeting HIRA individually in MCF10A cells.

Results indicated that among 4 different siRNAs, si_07 showed more mesenchymal like phenotype with elongated, spindle-like morphology and reduced cell-cell contact similar to H3.3A depletion while si_08 and si_09 showed mild effects on morphology with increased cell death on si_08. On the other hand, si_10 treated cells showed a distinct morphology of larger, more scattered, and flattened cells not suggesting different mechanism of si_10 than typical EMT or healthy epithelial cells (Figure 39.A). The efficiency of HIRA knockdown then validated through qPCR for the expression of HIRA gene and results showed that all siRNAs significantly reduced HIRA expression by more than 50% with slight differences (Figure 39.B).

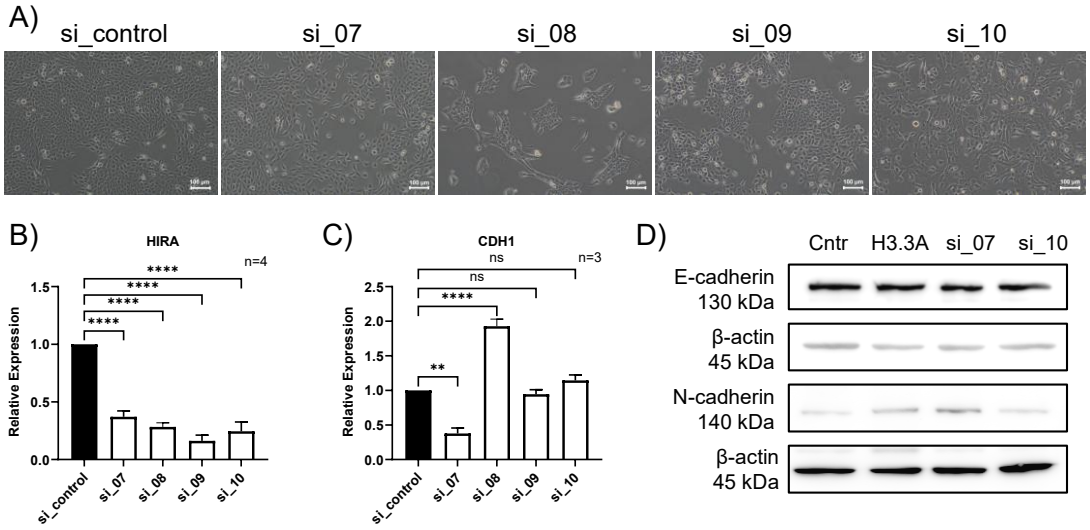

Figure 39. siRNAs mediated knockdown of HIRA reveals variable effects on EMT-associated phenotypes.
A) Phase contrast microscopy images showing morphological changes in MCF10A cells following transfection with four different siRNAs (si_07, si_08, si_09, si_10). B) Quantitative PCR analysis of HIRA expression levels following transfection with four HIRA siRNAs, showing more than 50% knockdown efficiency for all siRNAs with slight variability. C) CDH1 expression levels determined by qPCR in the same samples. D) Western blot analysis of E-Cad and N-cad levels in control, H3.3A and HIRA knockdown. (*p < 0.05, **p < 0.01, ***p < 0.001, ****p < 0.0001)

On the other hand, CDH1 expression showed distinct results among four siRNAs as si_07 led to a significant downregulation of CDH1 gene suggesting a similar EMT-like response like we identified following H3.3A depletion. Unexpectedly, si_08 resulted in increased CDH1 expression which might be caused by the loss of interested cells due to cell death. si_09 showed no significant difference which correlates with the morphological observations. Finally, si_10 showed no difference on CDH1 expression, supporting the idea of the morphological difference is independent of EMT but an alternative off-target effect of siRNA (Figure 39.C). Based on the morphological observations and qPCR results, we excluded si_08 and si_09 from further analysis. Next, we performed western analysis for si_07 and si_10 along with control and H3.3A knockdown samples. Consistently with earlier western blot results, E-Cad levels did not show any clear differences among samples. On the other hand, strong upregulation of N-Cad levels observed in si_07 treated cells similar to H3.3A knockdown. In contrast, si_10 treatment did not induce any changes in N-Cad levels, further supporting qPCR and distinct morphology (Figure 39.D). Next, immunofluorescence staining performed to further characterise the effect of HIRA depletion for two different siRNAs. Results demonstrated that the downregulation of CDH1 on mRNA level haven't been reflected as reduction of E-Cadherin signal, rather

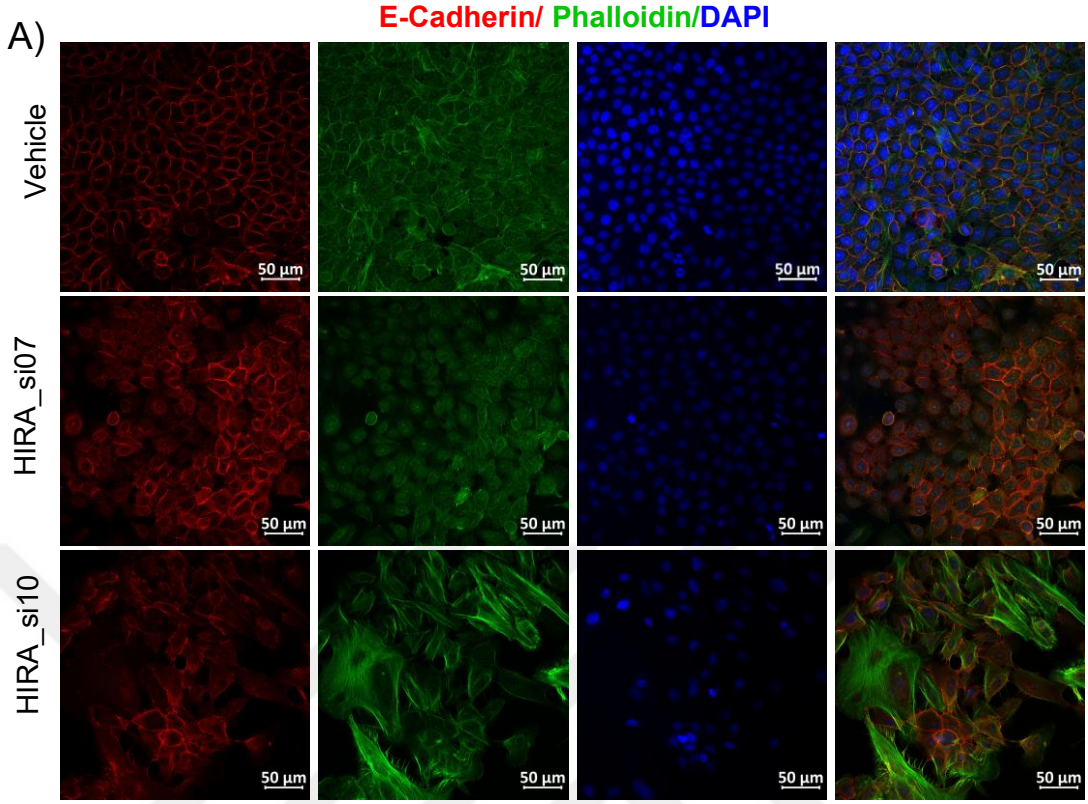

Figure 40. Immunofluorescence staining of E-Cadherin and actin stress fibers (phalloidin) in MCF10A cells for vehicle and cells with HIRA knockdown using si07 or si10. Nuclei were counterstained with DAPI and images were acquired using confocal microscope.

showed minor changes and redistribution of E-Cad from membrane to cytoplasm accompanied with moderate differences on actin stress fibres with slightly dispersed cells following si_07 treatment. In contrast, si_10 treatment resulted in enlarged and elongated cells with significant actin stress fibres with strong cytoplasmic E-Cadherin (Figure 40).

Given the distinct non-correlating results of si_10 transfection, we excluded from further analysis and performed qPCR analysis for EMT-related genes in si_07 treated cells. Our results showed significant downregulation of epithelial genes including CDH1, EHF, OVOL2, ELF3 and GRHL3 and upregulation of mesenchymal markers including CDH2, FN1, VIM, ZEB2 and SNAI1 suggesting depletion of HIRA promoters EMT-like transcriptional reprogramming (Figure 41).

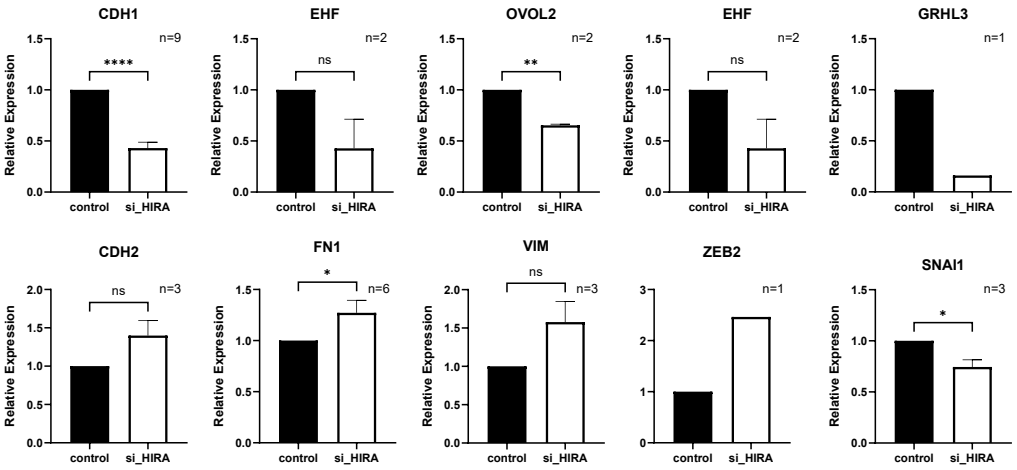

Figure 41. HIRA depletion induces EMT-like transcriptional reprogramming.
Quantitative real-time PCR (qPCR) analysis of epithelial and mesenchymal marker gene expression in si_07-transfected cells. Epithelial genes (CDH1, EHF, OVOL2, ELF3, and GRHL3) were significantly downregulated, while mesenchymal markers (CDH2, FN1, VIM, ZEB2, and SNAI1) were upregulated following HIRA knockdown. Statistical significance was determined using unpaired t-tests; (*p < 0.05, **p < 0.01, ***p < 0.001, ****p < 0.0001)

4.16. H3.3A Depletion Disrupts G1/S Transition and Decreases Cell Proliferation in MCF10A Cells

Our previous heatmap analysis represented that the expression of cell cycle related genes was changing upon H3.3A knockdown (Figure 37.A). It is also noted that, based on our observations through phase contrast microscopy and culturing the cells, proliferation and cell dynamics might be also affected by H3.3A and HIRA depletion. Based on these observations, we wanted to further examine the effect on cell cycle and growth behaviour first by examining differential expression data of H3.3A depletion compared with TGFβ3 treatment. To understand the effect of H3.3A knockdown on cell cycle we used publicly available GO terms panel of cell cycle genes (GOBP_CELL_CYCLE, MSigDB v. 2025.1. Hs) to generate heatmap. Heatmap data demonstrated that following H3.3A depletion there were a widespread downregulation of genes controlling G1/S phase (Figure 42.A) further confirmed by detailed analysis of RNA-seq data as significant downregulation of critical G1 phase regulators such as CCND1, CDK4, CDK6, RB1 and CDKN1C (Figure 42.B). It is also observed that S-phase associated genes such as PCNA, MCM2, RRM1 and RRM2 were downregulated, together suggesting an impaired G1/S transition (Figure 42.C).

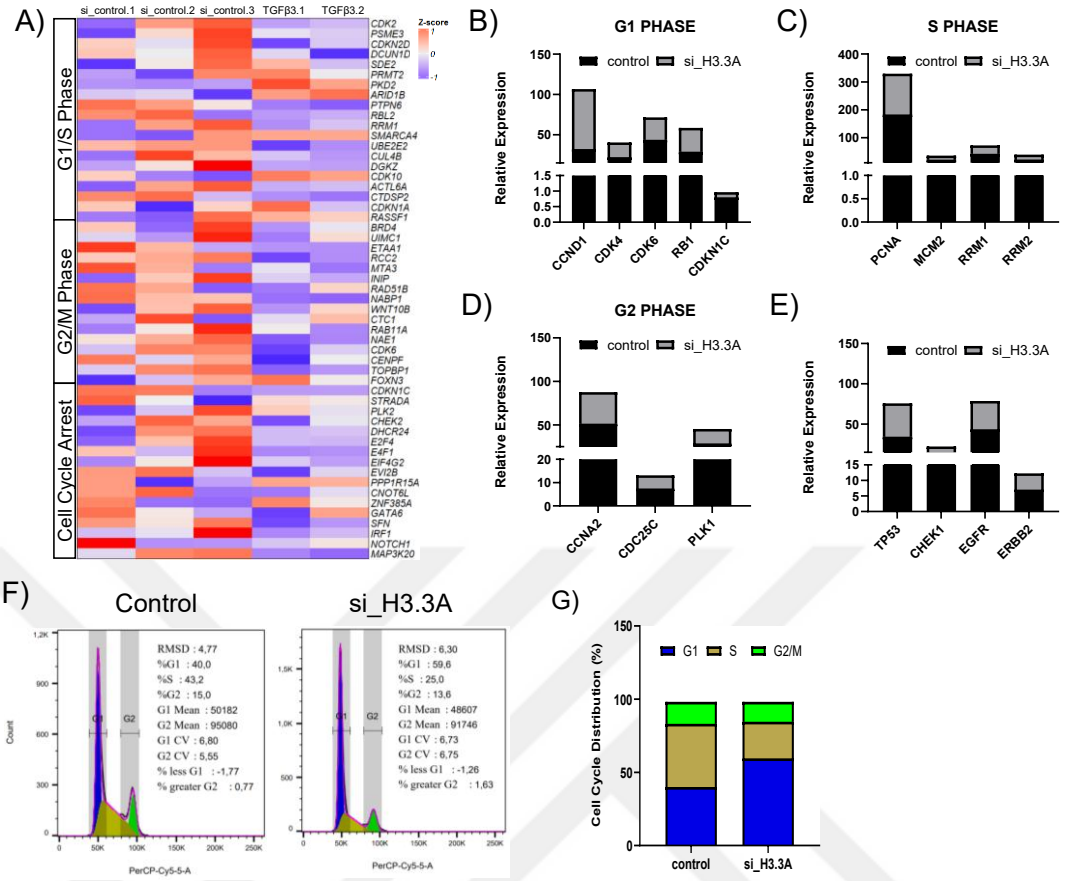

Figure 42. H3.3A depletion impairs G1/S transition and alters cell cycle progression.
(A) Heatmap showing expression changes of cell cycle related genes in si_H3.3A cells compared to control, highlighting widespread downregulation particularly in G1/S regulators. B) Bar plot showing significant downregulation of G1 phase regulators CCND1, CDK4, CDK6, RB1, and CDKN1C upon H3.3A knockdown. C) Expression levels of key S-phase–associated genes (PCNA, MCM2, RRM1, RRM2) are reduced, indicating impaired S-phase entry. D) G2/M phase genes (CCNA2 and PLK1) showed only modest changes in expression following H3.3A depletion. E) Heatmap showing moderate downregulation of cell cycle checkpoint genes including TP53 and CHEK1, suggesting that transcriptional alterations are more prominent in early cell cycle phases. F) Cell cycle distribution analysis by flow cytometry using PI staining in control and si_H3.3A-treated cells. G) Quantification of cell cycle phases shows a marked increase in G1-phase population (from 40.0% to 59.6%) and a corresponding decrease in S-phase (from 43.2% to 25.0%), while G2/M phase showed a modest decrease (from 15.0% to 13.6%).

In addition G2/M genes such as CCNA2 and PLK1 showed minor changes (Figure 42.D) while overall cell cycle checkpoint markers are significantly effected according to heatmap and showed moderate downregulation of checkpoint regulators such as TP53 and CHEK1 suggesting the transcriptional effects of H3.3A depletion occurs during earlier stages of cell cycle (Figure 42.E). Then, a detailed analysis of cell cycle was performed by flow cytometry using PI staining. The results of flow cytometry showed consistent changes with the gene expression data which showed a strong shift in G1 phase increasing from 40.0% (control) to 59.6% (si_H3.3A) while S-phase

is decreased from 43.2% to 25.0%. On the other hand, shift in G2/M phase were modest as it decreased from 15.0% to 13.6 upon H3.3A depletion (Figure 42.F-G).

Overall, these changes in cell cycle, supported by RNA-seq and flow cytometry suggests G1 phase arrest highlighting possible role of H3.3A in maintaining cell cycle regulation along with EMT particularly through G1/S transition.

Following our observations on cell cycle impairments, we next examined the effect of H3.3A and HIRA depletions from cell proliferation perspective. To assess cell viability, which reflects the proliferation rate and growth kinetics of the cells, Sulforhodamine B (SrB) assays was performed following H3.3A and HIRA knockdown. Consistent with previously defined impaired G1/S transition, H3.3A knockdown resulted in significant reduction in proliferation (Figure 43.A) which also further supported by a similar decrease on TGFβ3 treatment further supporting EMT-like phenotype (Figure 43.B). On the other hand, HIRA knockdown exhibited no significant difference in proliferation compared to control cells (Figure 43.A).

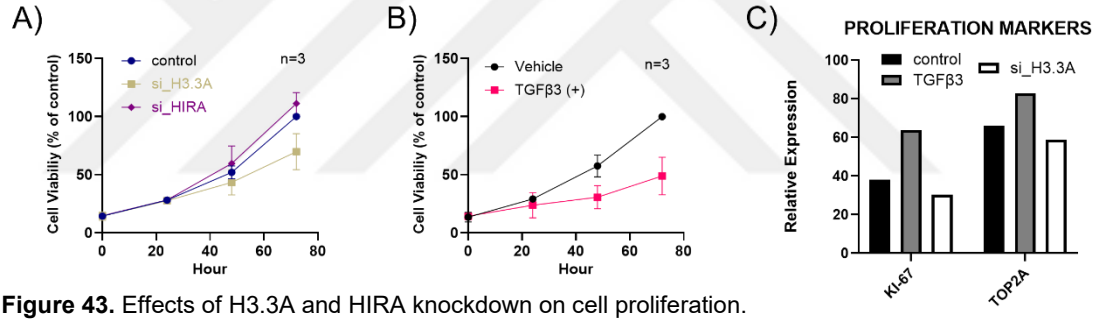

Figure 43. Effects of H3.3A and HIRA knockdown on cell proliferation.
A) SrB assay showing relative cell viability following knockdown of H3.3A or HIRA. H3.3A knockdown significantly reduced cell proliferation compared to control, consistent with impaired G1/S transition. HIRA knockdown had no significant effect on proliferation. B) SrB assay comparing proliferation of H3.3A knockdown cells with and without TGFβ3 treatment. A further reduction in proliferation upon TGFβ3 stimulation supports an EMT-like phenotype.

4.17. HIRA Knockdown Impairs H3.3 and ELF3 Deposition at Epithelial Gene Regulatory Regions

To further investigate the mechanisms behind the role of H3.3 in transcriptional regulation of EMT, we performed chromatin immunoprecipitation experiments by using HIRA knockdown followed by H3.3 and ELF3 enrichment for CHIP pulldown. H3.3A antibodies used as expected to understand if the deposition of H3.3 exists at key EMT related gene loci. Additionally, since the change in GRHL3 was highly significant upon H3.3A treatment, we used ELF3, which is a known regulator of GRHL3.

As described in Figure 29.A chromatin was isolated following HIRA knockdown and incubated for micrococcal nuclease (MNAse) digestion overnight to generate mono-nucleosome sized fragments for ChIP. The suitability of the acquired nucleosomes is then investigated by agarose gel electrophoresis, showing successful digestion and nucleosome resolution around 200 bp (Figure 44.B). Following MNAse digestion, antibodies against H3.3 and ELF3, along with IgG as control were used in control, HIRA depleted and TGFβ3 treated cells. qPCR experiments performed with acquired enriched DNA by primers designed to amplify upstream (-1) and downstream (+1) of transcriptional start sites of CDH1 and GRHL3 genes. Our results showed that, H3.3 occupancy was relatively stable for both HIRA depleted and TGFβ3 treated cells, while a slight decrease was observed for ELF3 enrichment in TGFβ3 treated cells (Figure 44.C). In contrast GRHL3 (-1/+1) results showed a significant reduction following H3.3 enrichment in HIRA knockdown, supporting critical role of HIRA as chaperon to deposit H3.3 at this promoter while TGFβ3 treated cells showed a strong reduction in both H3.3 and ELF3 occupancy (Figure 44.D). Together these findings support a functional link between HIRA-H3.3 and ELF3-mediated regulation of GRHL3 transcription and EMT-like association with CDH1 transcription.

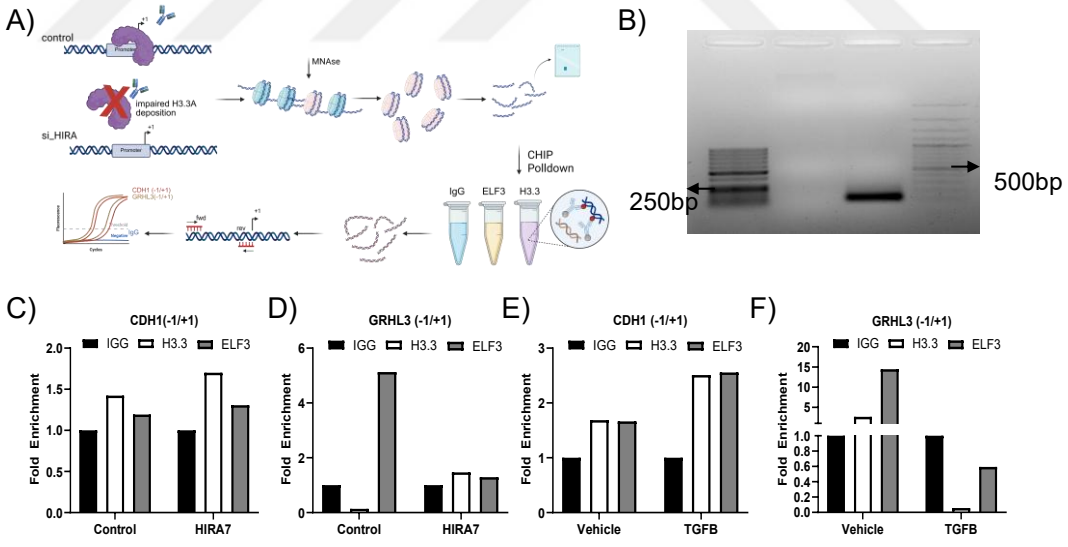

Figure 44. A) Schematic representation of the ChIP-qPCR workflow following HIRA knockdown and pulldown by IgG, H3.3 and ELF3 enrichment. B) Agarose gel confirming mononucleosome enrichment of chromatin that was digested using micrococcal nuclease. C-F) qPCRs showing enrichment at the transcription start site (+1) and upstream regulatory region (−1) of CDH1 and GRHL3 genes.

5. DISCUSSION

In this study, we investigated the role of histone variant H3.3 in epithelial to mesenchymal transition. Our results show that depletion of H3.3 induces EMT-like phenotypes in MCF10A cell line.

We used two epithelial cell lines to understand the effects of H3.3 depletion from a broader species-independent view. However, we identified that while H3.3A depletion in MCF10A cells resulted in EMT-like phenotype, no comparable response is detected in NMuMG cells.

MCF10A epithelial cell line is a non-tumorigenic human breast epithelial cell line derived from non-malignant proliferative breast tissue and one of the most used models for EMT studies [30].

When we performed a more comprehensive analysis of the response of MCF10A to TGFβ3 stimulation we realized that the heterogeneity of population creates a challenge to understand the underlining factors that are regulating major developmental processes such as EMT. Although MCF10A cells are widely used, the extend of research on the characteristics of MCF10A cell line especially its response to TGFβ3 and EMT processes is very limited.

Mammary gland cells are organized by two major epithelial components as basal and luminal layers [80, 81]. These different layers can be identified by their expression of Epithelial cell adhesion molecule (EpCAM), as reported as the luminal cells express EpCAM while it's expressed on normal epithelial cells at intercellular basolateral interfaces [82, 83]. MCF10A cells have basal like gene expression but also expressing luminal and progenitor markers exhibiting stem cell properties and several features of mesenchymal cell lines representing an abnormal mammary epithelial cell phenotype [31].

With this study, we demonstrated that MCF10A is a heterogenous population with 86.5 % E-Cad $^{(+)}$ cells with a significant population of E-Cad $^{(-)}$ cells. This heterogeneity of MCF10A creates challenges to use as a uniform model for EMT studies, because of the misrepresentative results by the presence of pre-existing CDH1 (-) cells. Loss of E-Cadherin alone has been shown to be insufficient to induce the EMT, but its loss has been associated with the activation of several EMT transcription factors, as previously mentioned [13]. Remarkably, Fsk treatment also led to improved F-actin localization at the membrane, with a reduction in the formation of stress fibres on vehicle cells compared to their Fsk (-) counterparts. This suggests

that Fsk may play a role in modulating the actin cytoskeleton, which is crucial for maintaining cell-cell adhesion.

Although, the change in the expression of CDH1 on mRNA level was significant, we could not identify any significant decrease on E-Cadherin at protein level but observed its localization to cytoplasm which may be indicative of acting of Wnt/β-catenin signalling by trans localization of β-catenin into nucleus enhancing the EMT process. Similarly, the expression level of N-Cadherin on mRNA as well as protein levels were significantly increased which is correlating with previous reports. Previous studies have shown that E-Cadherin protein levels are tightly regulated at both the transcriptional and post-transcriptional levels, and its stability can be influenced by many factors including interaction with cytoskeletal proteins[13, 84]. Additionally, it has been reported that E-Cadherin may be localized in the cytoplasm by chaperone proteins or regulatory proteins, including β-catenin, p120-catenin or tyrosine kinase receptors and phosphatases, and protected from degradation without significant changes in mRNA levels[85]. This suggests that the difference between CDH1 expression on mRNA levels and E-Cadherin protein levels could be due to post-transcriptional regulatory mechanisms such as stabilization of E-Cadherin protein in the cytoplasm, interference with protein degradation pathways and delayed protein turnover [84, 86]. Previous studies showed that media supplements and culture conditions are critical for MCF10A cells growth and improper maintenance of the cells can be indicated by morphological changes [87]. Several groups have identified, cAMP has important roles in many fundamental processes including cell growth and proliferation. As a cAMP inducer, our results showed comprehensive results that Fsk has significantly enhanced proliferation [36]. We identified fastened growth and proliferation profile that we supported by growth curve, duplication time and SrB analysis. The latter observation helps us to understand that lack of Ctx is disruptive, and cells health might be improved by substitution of Fsk. Our findings suggest that substituting Ctx with Fsk not only supports proliferation but also helps maintain the epithelial characteristics of MCF10A cells, ensuring their suitability for downstream applications.

It is also previously stated that cAMP regulates the balance of proliferation and differentiation of MCF10A cells. This regulatory function of cAMP is particularly important in the context of maintaining cellular homeostasis, cell proliferation and differentiation[31, 88, 89]. This expression of progenitor markers supporting our statement of decreased heterogeneity by the influence of cAMP signalling on

proliferative and differentiation potential of these cells considering MCF10A cells expressing progenitor markers unlike normal mammary epithelial profile [31, 88]. The cAMP pathway is a fundamental process that regulates many biological processes, such as cell proliferation, differentiation, and apoptosis [90].

Cholera toxin (Ctx) secreted by Vibrio cholera gram-negative bacteria is a widely used addition to culture media to induce cAMP pathway and boost cell proliferation [91]. It has been demonstrated through several studies that the presence of Ctx in MCF10A culture media, enables the formation of tight junctions, efficient ion transport and formation of epithelial barrier integrity and crucial for growth and differentiation of epithelial phenotype [92, 93]. However, its pathogenicity of life-threatening infectious disease characterised by such as severe diarrhoea, hypotension and shock causes risks of safety for cell culture practices and not allowed for certain countries [91, 94].

Forskolin, derived from *Coleus forskohlii*, is commonly used as cAMP activator by directly stimulating adenylyl cyclase. Although the mechanisms of Ctx and Fsk have differences on the entry of the cell, binding to adenylate cyclase and activation mechanisms, they are known to have similar effects as both are activators of c-AMP pathway that is through different mechanisms [94]. In another study it was reported that the supplementation of forskolin in culture media was sufficient to protect cells from UVB induced apoptosis and DNA damage[95]. Similar to our result, decrease of H2AX positive foci upon forskolin treatment and increase in number of viable cells and metabolic activity might be indicative of forskolin mediated protection of DNA damage and elevated survival.

We also observed better F-actin localization on the membrane with considerably less stress fibres on Fsk treated samples. We reasoned that Fsk is a good candidate as replacement to Chx seeing that it plays significant roles in the levels of F-actin due to elevated cAMP levels as previously suggested by Oh et.al. 2023, [96] either through the activation of protein kinase A, alteration of expression levels of transcription factors or changes in cell adhesion.

The results highlighted that the heterogeneity of the MCF10A cell line and the limitations of using as a uniform model in EMT studies. Our findings indicates that MCF10A cells contain a high fraction of E-Cad $^{(-)}$ cells, which may lead to misinterpretations of EMT-related processes. We demonstrated that TGFβ3 treatment induces EMT-like morphological changes, although cells couldn't undergo proper EMT. The use of forskolin as a substitute for cholera toxin results in enhanced cell proliferation and maintenance of epithelial characteristics, thus improving the

consistency of EMT-related experiments with MCF10A cell line. Overall, these findings contribute to further understanding the influencing factors affecting the behaviour of the MCF10A cells and offer insights for optimizing culture conditions for EMT and other developmental studies.

Although MCF10A is a non-tumorigenic human mammary breast epithelial cell line, it is isolated by Soule et.al. 1990 [97] from fibrocystic breast tissue of a patient. There is also increasing number of evidence that these cells exhibit tumorigenic potential when co-cultured with tumorigenic cells such as MCF7 by the disruption of their apical-basal polarity [79, 81, 98].

Furthermore, it has been shown that MCF10A cells exhibit chromosomal abnormalities such as introduced Myc oncogene and deletion of senescence related locus and comparable responses to growth factor signalling and stress to normal mammary epithelial cells [87, 99, 100]. Additionally, it is reported that it expresses different markers compared to normal breast tissues including hormone dependant proliferation and survival, lack of oestrogen receptor expression and tumour formation capacity [30, 31]. Considering all, we reasoned that the difference between our model systems might be causing not only because of species difference but also intrinsic heterogeneity and cancer prone nature of MCF10A cells.

H3.3 is a key histone variant in epigenetic regulation especially with its link with transcriptionally active regions results in widespread effects in nucleosome stability and chromatin accessibility [51, 55, 61]. Considering the different effects on MCF10A and NMuMG cells, we reasoned that epigenetically poised cell types like MCF10A may exhibit phenotypic changes upon H3.3A depletion because other histone variations and chromatin remodelers may decrease the effects of H3.3 loss in more stable epithelial cell lines like NMuMG cells [62, 101], suggesting H3.3 regulates epithelial stability and EMT in context-dependent manner. These findings are consistent with previous studies showing that the impact of H3.3 loss varies depending on cellular differentiation status and chromatin landscape [102, 103].

Although its context-dependent features, our results on H3.3A in MCF10A cells displayed strong evidence of EMT. Several studies reported that mutations or loss of H3.3 cause many pathologies including bone tumours. H3.3 has important roles in genome stability during mitosis and post-mitotic cells. It is also reported that H3.3A is more closely associated with proliferation associated [104] . EMT is closely associated with the regulation of cell cycle and characterized by cell cycle arrest and

disruption of proliferation [105]. Our results suggest an EMT-like phenotype on cell cycle with reduced S phase and G1 arrest.

MCF10A cells have distinct characteristics when compared to normal epithelial cell lines regarding the characteristics of the tissue it is derived. Studies also showed that its EMT process is regulated differently from the classical SNAI and ZEB controlled pathway, instead JUNB dependence takes place which is an important factor for cancer patient survival [106].Considering the literature of minor effects of SNAI1 and ZEB1 regulation and our results that no significant increase of mRNA expression following H3.3A depletion, we also reasoned that H3.3A might also have a role specifically in MCF10A cells due to its epigenetically poised and cancer-prone characteristics.

In correlation with our results, recent studies showed that HIRA can regulate EMT programs, regulate cell cycle and supress proliferation causing decreased oncogenic transformation. On the other hand, the study reported this induction might be through chromatin independent mechanisms and loss of HIRA induces both EMT and MyC and E2F programs regardless of the changes in H3.3 deposition[67].

6. CONCLUSIONS AND SUGGESTIONS

We demonstrated that H3.3A depletion induces EMT-like phenotypes in MCF10A human mammary epithelial cells, while no comparable response was observed in other cells. These findings highlighted a potential context-dependent role of H3.3 in the epigenetic regulation of EMT.

Our findings suggest that intrinsic cellular heterogeneity plays important role in partial EMT phenotype observed in MCF10A cells. The transcriptional, post-transcriptional, and signalling pathways behind is controlled by a complex interplay that shapes the dynamic character of epithelial cell plasticity during EMT. By combining gene expression, clonal expansion, and cell sorting, we show that intrinsic heterogeneity and dynamic transition is maintained even in clonally derived cells, proving that E-Cadherin membrane expression is not a reliable indicator of EMT potential. Additionally, we demonstrate that GRHL3 expression can cause some clones to diverge from the standard EMT pathway, suggesting context-specific resistance to EMT.

Moreover, we demonstrated that Fsk, a cAMP inducer, can serve as an effective substitute for cholera toxin Ctx in MCF10A culture media. Fsk enhanced epithelial characteristics, improved cell proliferation, and reduced culture variability, potentially offering a safer alternative for MCF10A for EMT studies.

Association of H3.3 with transcriptionally active chromatin and genome stability may explain the phenotypic outcomes of its depletion. The EMT-like characteristics and altered cell cycle progression observed in H3.3A-depleted MCF10A cells point to a critical role for H3.3 in regulating proliferation and differentiation programs, consistent with previous reports linking H3.3 to proliferation in cancer cells. Our data suggest that epigenetically dynamic cells such as MCF10A are more vulnerable to depletions in H3.3 levels, while cells like NMuMG may compensate by alternative mechanisms.

The mechanistic role of H3.3A in EMT should be further studied, especially in relation to how its depletion affects transcription factor accessibility and chromatin structure at important EMT-associated gene loci. ATAC-seq, ChIP-seq for histone marks, and RNA-seq may be able to shed light on H3.3A's function from chromatin perspective and the epigenetic landscape that e promotes EMT, as our results indicate that H3.3A depletion causes EMT-like changes in MCF10A cells but not in NMuMG cells.

Given the correlation that has been found between H3.3A depletion and changes in the cell cycle, specifically G1 arrest and S-phase reduction, it would be helpful to investigate whether these changes are a direct result of EMT or a side effect of epigenetic disruption.

Lastly, by disrupting epithelial identity and allowing partial EMT, our research suggests that H3.3A loss could be a factor in early tumorigenic events. Tissue-specific H3.3A knockout models in development or tumour initiation settings should be used to validate this theory in vivo. Assessing whether H3.3A depletion, along with other genetic changes commonly observed in breast cancer, drives cells to oncogenic transformation or metastatic behaviour would also be instructive.

Taken together, our findings contribute to better understand the role of H3.3 in EMT. We also highlighted the importance of cellular context and cell line heterogeneity in studying histone variant function.

7. REFERENCES

1. Dongre, A. & Weinberg, R. A. (2019) New insights into the mechanisms of epithelial-mesenchymal transition and implications for cancer, *Nat Rev Mol Cell Biol.* **20**, 69-84.
2. Zheng, H. & Kang, Y. (2014) Multilayer control of the EMT master regulators, *Oncogene.* **33**, 1755-63.
3. Hodge, D. Q., Cui, J., Gamble, M. J. & Guo, W. (2018) Histone variant MacroH2A1 plays an isoform-specific role in suppressing epithelial-mesenchymal transition, *Scientific Reports.* **8**, 841.
4. Pei, D., Shu, X., Gassama-Diagne, A. & Thiery, J. P. (2019) Mesenchymal-epithelial transition in development and reprogramming, *Nat Cell Biol.* **21**, 44-53.
5. Ribatti, D., Tamma, R. & Annese, T. (2020) Epithelial-Mesenchymal Transition in Cancer: A Historical Overview, *Transl Oncol.* **13**, 100773.
6. Domaschenz, R., Kurscheid, S., Nekrasov, M., Han, S. & Tremethick, D. J. (2017) The Histone Variant H2A.Z Is a Master Regulator of the Epithelial-Mesenchymal Transition, *Cell Rep.* **21**, 943-952.
7. Weyemi, U., Redon, C. E., Choudhuri, R., Aziz, T., Maeda, D., Boufraqech, M., Parekh, P. R., Sethi, T. K., Kasoji, M., Abrams, N., Merchant, A., Rajapakse, V. N. & Bonner, W. M. (2016) The histone variant H2A.X is a regulator of the epithelial-mesenchymal transition, *Nat Commun.* **7**, 10711.
8. Yukawa, M., Akiyama, T., Franke, V., Mise, N., Isagawa, T., Suzuki, Y., Suzuki, M. G., Vlahovicek, K., Abe, K., Aburatani, H. & Aoki, F. (2014) Genome-wide analysis of the chromatin composition of histone H2A and H3 variants in mouse embryonic stem cells, *PLoS One.* **9**, e92689.
9. Thiery, J. P., Acloque, H., Huang, R. Y. & Nieto, M. A. (2009) Epithelial-mesenchymal transitions in development and disease, *Cell.* **139**, 871-890.
10. Nieto, M. A., Huang, R. Y.-J., Jackson, R. A. & Thiery, J. P. (2016) EMT: 2016, *Cell.* **166**, 21-45.
11. Pastushenko, I. & Blanpain, C. (2019) EMT transition states during tumor progression and metastasis, *Trends Cell Biol.* **29**, 212-226.
12. Lu, W. & Kang, Y. (2019) Epithelial-mesenchymal plasticity in cancer progression and metastasis, *Developmental cell.* **49**, 361-374.
13. Loh, C.-Y., Chai, J. Y., Tang, T. F., Wong, W. F., Sethi, G., Shanmugam, M. K., Chong, P. P. & Looi, C. Y. (2019) The E-cadherin and N-cadherin switch in epithelial-to-mesenchymal transition: signaling, therapeutic implications, and challenges, *Cells.* **8**, 1118.
14. Aiello, N. M., Maddipati, R., Norgard, R. J., Balli, D., Li, J., Yuan, S., Yamazoe, T., Black, T., Sahmoud, A. & Furth, E. E. (2018) EMT subtype influences epithelial plasticity and mode of cell migration, *Developmental cell.* **45**, 681-695. e4.
15. Lamouille, S., Xu, J. & Derynck, R. (2014) Molecular mechanisms of epithelial–mesenchymal transition, *Nature reviews Molecular cell biology.* **15**, 178-196.
16. Wheelock, M. J., Shintani, Y., Maeda, M., Fukumoto, Y. & Johnson, K. R. (2008) Cadherin switching, *Journal of cell science.* **121**, 727-735.
17. Yang, J., Antin, P., Berx, G., Blanpain, C., Brabletz, T., Bronner, M., Campbell, K., Cano, A., Casanova, J., Christofori, G., Dedhar, S., Derynck, R., Ford, H. L., Fuxe, J., Garcia de Herreros, A., Goodall, G. J., Hadjantonakis, A. K., Huang, R. Y. J., Kalcheim, C., Kalluri, R., Kang, Y., Khew-Goodall, Y., Levine, H., Liu, J., Longmore, G. D., Mani, S. A., Massague, J., Mayor, R., McClay, D., Mostov, K. E., Newgreen, D. F., Nieto, M. A., Puisieux, A., Runyan, R., Savagner, P., Stanger, B., Stemmler, M. P., Takahashi, Y., Takeichi, M., Theveneau, E., Thiery, J. P., Thompson, E. W., Weinberg, R. A., Williams, E. D., Xing, J., Zhou, B. P., Sheng, G. & Association, E. M.

T. I. (2020) Guidelines and definitions for research on epithelial-mesenchymal transition, *Nat Rev Mol Cell Biol.* **21**, 341-352.
18. Kalluri, R. & Weinberg, R. A. (2010) The basics of epithelial-mesenchymal transition, *The Journal of clinical investigation.* **120**, 1786-1786.
19. Massagué, J. (2008) TGFβ in cancer, *Cell.* **134**, 215-230.
20. Lavin, D. P. & Tiwari, V. K. (2020) Unresolved complexity in the gene regulatory network underlying EMT, *Front Oncol.* **10**, 554.
21. Fazilaty, H., Rago, L., Kass Youssef, K., Ocaña, O. H., Garcia-Asencio, F., Arcas, A., Galceran, J. & Nieto, M. A. (2019) A gene regulatory network to control EMT programs in development and disease, *Nature communications.* **10**, 5115.
22. Kim, Y.-S., Yi, B.-R., Kim, N.-H. & Choi, K.-C. (2014) Role of the epithelial–mesenchymal transition and its effects on embryonic stem cells, *Exp Mol Med.* **46**, e108-e108.
23. Acloque, H., Adams, M. S., Fishwick, K., Bronner-Fraser, M. & Nieto, M. A. (2009) Epithelial-mesenchymal transitions: the importance of changing cell state in development and disease, *The Journal of clinical investigation.* **119**, 1438-1449.
24. Yao, W., Wang, Z., Ma, H., Lin, Y., Liu, X., Li, P. & He, X. (2024) Epithelial-mesenchymal plasticity (EMP) in wound healing: Exploring EMT mechanisms, regulatory network, and therapeutic opportunities, *Heliyon.* **10**.
25. Chuang, K.-T., Chiou, S.-S. & Hsu, S.-H. (2023) Recent advances in transcription factors biomarkers and targeted therapies focusing on epithelial–mesenchymal transition, *Cancers (Basel).* **15**, 3338.
26. Min, C., Eddy, S. F., Sherr, D. H. & Sonenshein, G. E. (2008) NF-κB and epithelial to mesenchymal transition of cancer, *Journal of cellular biochemistry.* **104**, 733-744.
27. Migault, M., Sapkota, S. & Bracken, C. P. (2022) Transcriptional and post-transcriptional control of epithelial-mesenchymal plasticity: why so many regulators?, *Cellular and Molecular Life Sciences.* **79**, 182.
28. Crawford, A. T., Desai, D., Gokina, P., Basak, S. & Kim, H. A. (2008) E-cadherin expression in postnatal Schwann cells is regulated by the cAMP-dependent protein kinase a pathway, *Glia.* **56**, 1637-1647.
29. Sayan, A. E., Griffiths, T. R., Pal, R., Browne, G. J., Ruddick, A., Yagci, T., Edwards, R., Mayer, N. J., Qazi, H. & Goyal, S. (2009) SIP1 protein protects cells from DNA damage-induced apoptosis and has independent prognostic value in bladder cancer, *Proceedings of the National Academy of Sciences.* **106**, 14884-14889.
30. Goh, J. J. H., Goh, C. J. H., Lim, Q. W., Zhang, S., Koh, C.-G. & Chiam, K.-H. (2022) Transcriptomics indicate nuclear division and cell adhesion not recapitulated in MCF7 and MCF10A compared to luminal A breast tumours, *Scientific Reports.* **12**, 20902.
31. Qu, Y., Han, B., Yu, Y., Yao, W., Bose, S., Karlan, B. Y., Giuliano, A. E. & Cui, X. (2015) Evaluation of MCF10A as a Reliable Model for Normal Human Mammary Epithelial Cells, *PLoS One.* **10**, e0131285.
32. Xie, L., Law, B. K., Aakre, M. E., Edgerton, M., Shyr, Y., Bhowmick, N. A. & Moses, H. L. (2003) Transforming growth factor beta-regulated gene expression in a mouse mammary gland epithelial cell line, *Breast Cancer Res.* **5**, R187.
33. Piek, E., Moustakas, A., Kurisaki, A., Heldin, C.-H. & Dijke, P. t. (1999) TGF-β type I receptor/ALK-5 and Smad proteins mediate epithelial to mesenchymal transdifferentiation in NMuMG breast epithelial cells, *Journal of cell science.* **112**, 4557-4568.
34. Takahashi, K. & Yamanaka, S. (2006) Induction of pluripotent stem cells from mouse embryonic and adult fibroblast cultures by defined factors, *Cell.* **126**, 663-676.

35. <[48] Keller et.al.2010-Mapping the cellular and molecular heterogeneity of normal and malignant breast tissues and cultured cell lines.pdf>.
36. Chen, B., Lin, T., Yang, X., Li, Y., Xie, D. & Cui, H. (2016) Intermittent parathyroid hormone (1-34) application regulates cAMP-response element binding protein activity to promote the proliferation and osteogenic differentiation of bone mesenchymal stromal cells, via the cAMP/PKA signaling pathway, *Experimental and Therapeutic Medicine.* **11**, 2399-2406.
37. Luger, K., Mäder, A. W., Richmond, R. K., Sargent, D. F. & Richmond, T. J. (1997) Crystal structure of the nucleosome core particle at 2.8 Å resolution, *Nature.* **389**, 251-260.
38. Wong, L. H. & Tremethick, D. J. (2025) Multifunctional histone variants in genome function, *Nat Rev Genet.* **26**, 82-104.
39. Libertini, L., Ausio, J., Van Holde, K. & Small, E. (1988) Histone hyperacetylation. Its effects on nucleosome core particle transitions, *Biophysical journal.* **53**, 477-487.
40. Krietenstein, N. & Rando, O. J. (2020) Mesoscale organization of the chromatin fiber, *Curr Opin Genet Dev.* **61**, 32-36.
41. Lieberman-Aiden, E., Van Berkum, N. L., Williams, L., Imakaev, M., Ragoczy, T., Telling, A., Amit, I., Lajoie, B. R., Sabo, P. J. & Dorschner, M. O. (2009) Comprehensive mapping of long-range interactions reveals folding principles of the human genome, *Science.* **326**, 289-293.
42. Fudenberg, G., Imakaev, M., Lu, C., Goloborodko, A., Abdennur, N. & Mirny, L. A. (2016) Formation of chromosomal domains by loop extrusion, *Cell reports.* **15**, 2038-2049.
43. Dubochet, J., Adrian, M., Schultz, P. & Oudet, P. (1986) Cryo-electron microscopy of vitrified SV40 minichromosomes: the liquid drop model, *EMBO.* **5**, 519-528.
44. Fussner, E., Strauss, M., Djuric, U., Li, R., Ahmed, K., Hart, M., Ellis, J. & Bazett-Jones, D. P. (2012) Open and closed domains in the mouse genome are configured as 10-nm chromatin fibres, *EMBO Rep.* **13**, 992-996.
45. Nishino, Y., Eltsov, M., Joti, Y., Ito, K., Takata, H., Takahashi, Y., Hihara, S., Frangakis, A. S., Imamoto, N. & Ishikawa, T. (2012) Human mitotic chromosomes consist predominantly of irregularly folded nucleosome fibres without a 30-nm chromatin structure, *EMBO.* **31**, 1644-1653.
46. Maeshima, K., Ide, S. & Babokhov, M. (2019) Dynamic chromatin organization without the 30-nm fiber, *Current opinion in cell biology.* **58**, 95-104.
47. Miyazaki, K. & Miyazaki, M. (2021) The interplay between chromatin architecture and lineage-specific transcription factors and the regulation of rag gene expression, *Front Immunol.* **12**, 659761.
48. Dixon, J. R., Jung, I., Selvaraj, S., Shen, Y., Antosiewicz-Bourget, J. E., Lee, A. Y., Ye, Z., Kim, A., Rajagopal, N. & Xie, W. (2015) Chromatin architecture reorganization during stem cell differentiation, *Nature.* **518**, 331-336.
49. Liu, Z., Lee, D.-S., Liang, Y., Zheng, Y. & Dixon, J. R. (2023) Foxp3 orchestrates reorganization of chromatin architecture to establish regulatory T cell identity, *Nature Communications.* **14**, 6943.
50. Nie, Y. & Wang, M. (2024) Dynamic Changes in Histone Modifications Are Associated with Differential Chromatin Interactions, *Genes.* **15**, 988.
51. Henikoff, S. & Ahmad, K. (2005) Assembly of variant histones into chromatin, *Annu Rev Cell Dev Biol.* **21**, 133-153.
52. van Holde, K. E. (1989) The proteins of chromatin. I. Histones in *Chromatin* pp. 69-180, Springer.
53. Hake, S. B., Garcia, B. A., Duncan, E. M., Kauer, M., Dellaire, G., Shabanowitz, J., Bazett-Jones, D. P., Allis, C. D. & Hunt, D. F. (2006) Expression patterns and post-

translational modifications associated with mammalian histone H3 variants, *Journal of Biological Chemistry.* **281**, 559-568.
54. Buschbeck, M. & Hake, S. B. (2017) Variants of core histones and their roles in cell fate decisions, development and cancer, *Nature reviews Molecular cell biology.* **18**, 299-314.
55. Goldberg, A. D., Banaszynski, L. A., Noh, K.-M., Lewis, P. W., Elsaesser, S. J., Stadler, S., Dewell, S., Law, M., Guo, X. & Li, X. (2010) Distinct factors control histone variant H3. 3 localization at specific genomic regions, *Cell.* **140**, 678-691.
56. Talbert, P. B. & Henikoff, S. (2017) Histone variants on the move: substrates for chromatin dynamics, *Nature reviews Molecular cell biology.* **18**, 115-126.
57. Boulard, M., Bouvet, P., Kundu, T. K. & Dimitrov, S. (2007) Histone variant nucleosomes, *Chromatin and Disease*, 73-92.
58. Ridgway, P., Brown, K. D., Rangasamy, D., Svensson, U. & Tremethick, D. J. (2004) Unique Residues on the H2A. Z Containing Nucleosome Surface Are Important for Xenopus laevis Development*♦, *Journal of Biological Chemistry.* **279**, 43815-43820.
59. Faast, R., Thonglairoam, V., Schulz, T. C., Beall, J., Wells, J. R., Taylor, H., Matthaei, K., Rathjen, P. D., Tremethick, D. J. & Lyons, I. (2001) Histone variant H2A. Z is required for early mammalian development, *Current Biology.* **11**, 1183-1187.
60. Chang, C. J., Chao, C. H., Xia, W., Yang, J. Y., Xiong, Y., Li, C. W., Yu, W. H., Rehman, S. K., Hsu, J. L., Lee, H. H., Liu, M., Chen, C. T., Yu, D. & Hung, M. C. (2011) p53 regulates epithelial-mesenchymal transition and stem cell properties through modulating miRNAs, *Nat Cell Biol.* **13**, 317-23.
61. Szenker, E., Ray-Gallet, D. & Almouzni, G. (2011) The double face of the histone variant H3.3, *Cell Res.* **21**, 421-34.
62. Martire, S. & Banaszynski, L. A. (2020) The roles of histone variants in fine-tuning chromatin organization and function, *Nature reviews Molecular cell biology.* **21**, 522-541.
63. Chen, P., Zhao, J., Wang, Y., Wang, M., Long, H., Liang, D., Huang, L., Wen, Z., Li, W. & Li, X. (2013) H3. 3 actively marks enhancers and primes gene transcription via opening higher-ordered chromatin, *Genes Dev.* **27**, 2109-2124.
64. Talbert, P. B. & Henikoff, S. (2010) Histone variants—ancient wrap artists of the epigenome, *Nature reviews Molecular cell biology.* **11**, 264-275.
65. Arfè, S., Karagyozova, T., Forest, A., Bingham, D., Hmidan, H., Mazaud, D., Garnier, M., Le Baccon, P., Meshorer, E. & Quivy, J.-P. (2025) H3. 3 deposition counteracts the replication-dependent enrichment of H3. 1 at chromocenters in embryonic stem cells, *Nature Communications.* **16**, 5138.
66. Behjati, S., Tarpey, P. S., Presneau, N., Scheipl, S., Pillay, N., Van Loo, P., Wedge, D. C., Cooke, S. L., Gundem, G. & Davies, H. (2013) Distinct H3F3A and H3F3B driver mutations define chondroblastoma and giant cell tumor of bone, *Nat Genet.* **45**, 1479-1482.
67. Valcarcel-Jimenez, L., Rogerson, C., Yong, C., Schmidt, C., Yang, M., Cremades-Rodelgo, M., Harle, V., Offord, V., Wong, K. & Mora, A. (2022) HIRA loss transforms FH-deficient cells, *Science advances.* **8**, eabq8297.
68. Ray-Gallet, D., Quivy, J.-P., Scamps, C., Martini, E. M.-D., Lipinski, M. & Almouzni, G. (2002) HIRA is critical for a nucleosome assembly pathway independent of DNA synthesis, *Molecular cell.* **9**, 1091-1100.
69. Ray-Gallet, D., Ricketts, M. D., Sato, Y., Gupta, K., Boyarchuk, E., Senda, T., Marmorstein, R. & Almouzni, G. (2018) Functional activity of the H3. 3 histone chaperone complex HIRA requires trimerization of the HIRA subunit, *Nature communications.* **9**, 3103.

70. Lorain, S. p., Quivy, J.-P., Monier-Gavelle, F. d. r., Scamps, C., Lécluse, Y., Almouzni, G. v. & Lipinski, M. (1998) Core histones and HIRIP3, a novel histone-binding protein, directly interact with WD repeat protein HIRA, *Molecular and cellular biology.* **18**, 5546-5556.
71. Tagami, H., Ray-Gallet, D., Almouzni, G. & Nakatani, Y. (2004) Histone H3. 1 and H3. 3 complexes mediate nucleosome assembly pathways dependent or independent of DNA synthesis, *Cell.* **116**, 51-61.
72. Xiong, C., Wen, Z., Yu, J., Chen, J., Liu, C.-P., Zhang, X., Chen, P., Xu, R.-M. & Li, G. (2018) UBN1/2 of HIRA complex is responsible for recognition and deposition of H3. 3 at cis-regulatory elements of genes in mouse ES cells, *BMC biology.* **16**, 110.
73. Loppin, B., Bonnefoy, E., Anselme, C., Laurençon, A., Karr, T. L. & Couble, P. (2005) The histone H3. 3 chaperone HIRA is essential for chromatin assembly in the male pronucleus, *Nature.* **437**, 1386-1390.
74. Schoberleitner, I., Bauer, I., Huang, A., Andreyeva, E. N., Sebald, J., Pascher, K., Rieder, D., Brunner, M., Podhraski, V. & Oemer, G. (2021) CHD1 controls H3. 3 incorporation in adult brain chromatin to maintain metabolic homeostasis and normal lifespan, *Cell reports.* **37**.
75. Choi, J., Kim, T. & Cho, E.-J. (2024) HIRA vs. DAXX: the two axes shaping the histone H3. 3 landscape, *Exp Mol Med.* **56**, 251-263.
76. Tafessu, A., O'Hara, R., Martire, S., Dube, A. L., Saha, P., Gant, V. U. & Banaszynski, L. A. (2023) H3. 3 contributes to chromatin accessibility and transcription factor binding at promoter-proximal regulatory elements in embryonic stem cells, *Genome biology.* **24**, 25.
77. Bibel, M., Richter, J., Lacroix, E. & Barde, Y.-A. (2007) Generation of a defined and uniform population of CNS progenitors and neurons from mouse embryonic stem cells, *Nature protocols.* **2**, 1034-1043.
78. Lone, I. N., Sekeroglu, E. O., Kafaz, G. I., Al Haija, A. A. H. A., Turker, E., Batur, T. & Diril, M. K. (2025) Cost-Effective Production of Biologically Active Leukemia Inhibitory Factor for Mouse Embryonic Stem Cell Culture, *Mol Biotechnol*.
79. McLaughlin, A. J., Kaniski, A. J., Matti, D. I. & Xhabija, B. (2023) Comparative Morphological Analysis of MCF10A and MCF7 Cells Using Holographic Time-lapse Microscopy, *Anticancer Res.* **43**, 3891-3896.
80. Forster, N., Saladi, S. V., van Bragt, M., Sfondouris, M. E., Jones, F. E., Li, Z. & Ellisen, L. W. (2014) Basal cell signaling by p63 controls luminal progenitor function and lactation via NRG1, *Dev Cell.* **28**, 147-60.
81. Li, Z. D., Yu, X., Mei, Z., Zeng, T., Chen, L., Xu, X. L., Li, H., Huang, T. & Cai, Y. D. (2022) Identifying luminal and basal mammary cell specific genes and their expression patterns during pregnancy, *PLoS One.* **17**, e0267211.
82. Keller, P. J., Lin, A. F., Arendt, L. M., Klebba, I., Jones, A. D., Rudnick, J. A., DiMeo, T. A., Gilmore, H., Jefferson, D. M. & Graham, R. A. (2010) Mapping the cellular and molecular heterogeneity of normal and malignant breast tissues and cultured cell lines, *Breast Cancer Res.* **12**, R87.
83. Martowicz, A., Rainer, J., Lelong, J., Spizzo, G., Gastl, G. & Untergasser, G. (2013) EpCAM overexpression prolongs proliferative capacity of primary human breast epithelial cells and supports hyperplastic growth, *Mol Cancer.* **12**, 56.
84. Ramirez Moreno, M., Stempor, P. & Bulgakova, N. (2021) Interactions and feedbacks in E-cadherin transcriptional regulation. Front Cell Dev Biol. 2021; 9: 701175 in
85. Niño, C. A., Sala, S. & Polo, S. (2019). When ubiquitin meets E-cadherin: plasticity of the epithelial cellular barrier. Paper presented at the *Semin Cell Dev Biol*.

86. Segelle, A., Nunez-Alvarez, Y., Oldfield, A. J., Webb, K. M., Voigt, P. & Luco, R. F. (2022) Histone marks regulate the epithelial-to-mesenchymal transition via alternative splicing, *Cell Rep.* **38**, 110357.
87. Debnath, J., Muthuswamy, S. K. & Brugge, J. S. (2003) Morphogenesis and oncogenesis of MCF-10A mammary epithelial acini grown in three-dimensional basement membrane cultures, *Methods.* **30**, 256-268.
88. Nedvetsky, P. I., Kwon, S. H., Debnath, J. & Mostov, K. E. (2012) Cyclic AMP regulates formation of mammary epithelial acini in vitro, *Mol Biol Cell.* **23**, 2973-81.
89. Ahmed, M. B., Alghamdi, A. A., Islam, S. U., Lee, J.-S. & Lee, Y.-S. (2022) cAMP signaling in cancer: a PKA-CREB and EPAC-centric approach, *Cells.* **11**, 2020.
90. Henry, C., Wilcox, M. & Asirvatham, A. L. (2024) Forskolin-mediated cAMP activation upregulates TNF-α expression despite NF-κB downregulation in LPS-treated Schwann cells, *PLoS One.* **19**, e0302223.
91. Ghoubay-Benallaoua, D., Pécha, F., Goldschmidt, P., Fialaire-Legendre, A., Chaumeil, C., Laroche, L. & Borderie, V. M. (2012) Effects of isoproterenol and cholera toxin on human limbal epithelial cell cultures, *Current Eye Research.* **37**, 644-653.
92. Wang, G. G., Allis, C. D. & Chi, P. (2007) Chromatin remodeling and cancer, Part I: Covalent histone modifications, *Trends Mol Med.* **13**, 363-372.
93. Park, S., Mazina, O., Kitagawa, A., Wong, P. & Matsumura, F. (2004) TCDD causes suppression of growth and differentiation of MCF10A, human mammary epithelial cells by interfering with their insulin receptor signaling through c-Src kinase and ERK activation, *J Biochem Mol Toxicol.* **18**, 322-31.
94. Snider, R. M., McKenzie, J. R., Kraft, L., Kozlov, E., Wikswo, J. P. & Cliffel, D. E. (2010) The effects of cholera toxin on cellular energy metabolism, *Toxins (Basel).* **2**, 632-48.
95. Passeron, T., Namiki, T., Passeron, H. J., Le Pape, E. & Hearing, V. J. (2009) Forskolin protects keratinocytes from UVB-induced apoptosis and increases DNA repair independent of its effects on melanogenesis, *Journal of investigative dermatology.* **129**, 162-166.
96. Oh, M., Batty, S., Banerjee, N. & Kim, T. H. (2023) High extracellular glucose promotes cell motility by modulating cell deformability and contractility via the cAMP-RhoA-ROCK axis in human breast cancer cells, *Mol Biol Cell.* **34**, ar79.
97. Soule, H. D., Maloney, T. M., Wolman, S. R., Peterson Jr, W. D., Brenz, R., McGrath, C. M., Russo, J., Pauley, R. J., Jones, R. F. & Brooks, S. (1990) Isolation and characterization of a spontaneously immortalized human breast epithelial cell line, MCF-10, *Cancer Res.* **50**, 6075-6086.
98. Kenny, P. A., Lee, G. Y., Myers, C. A., Neve, R. M., Semeiks, J. R., Spellman, P. T., Lorenz, K., Lee, E. H., Barcellos-Hoff, M. H. & Petersen, O. W. (2007) The morphologies of breast cancer cell lines in three-dimensional assays correlate with their profiles of gene expression, *Molecular oncology.* **1**, 84-96.
99. Comaills, V., Kabeche, L., Morris, R., Buisson, R., Yu, M., Madden, M. W., LiCausi, J. A., Boukhali, M., Tajima, K. & Pan, S. (2016) Genomic instability is induced by persistent proliferation of cells undergoing epithelial-to-mesenchymal transition, *Cell reports.* **17**, 2632-2647.
100. Kietzman, W., Riegel, A. T. & Ory, V. (2017) Early-stage progression of breast cancer, *Breast cancer-from biology to medicine*.
101. Banaszynski, L. A., Wen, D., Dewell, S., Whitcomb, S. J., Lin, M., Diaz, N., Elsässer, S. J., Chapgier, A., Goldberg, A. D. & Canaani, E. (2013) Hira-dependent histone H3. 3 deposition facilitates PRC2 recruitment at developmental loci in ES cells, *Cell.* **155**, 107-120.

102. Elsässer, S. J., Noh, K.-M., Diaz, N., Allis, C. D. & Banaszynski, L. A. (2015) Histone H3. 3 is required for endogenous retroviral element silencing in embryonic stem cells, *Nature.* **522**, 240-244.
103. Jang, C.-W., Shibata, Y., Starmer, J., Yee, D. & Magnuson, T. (2015) Histone H3. 3 maintains genome integrity during mammalian development, *Genes Dev.* **29**, 1377-1392.
104. Klein, R. H. & Knoepfler, P. S. (2023) Knockout tales: the versatile roles of histone H3. 3 in development and disease, *Epigenetics & Chromatin.* **16**, 38.
105. Schuhwerk, H. & Brabletz, T. (2023). Mutual regulation of TGFβ-induced oncogenic EMT, cell cycle progression and the DDR. Paper presented at the *Semin Cancer Biol*.
106. Antón-García, P., Haghighi, E. B., Rose, K., Vladimirov, G., Boerries, M. & Hecht, A. (2023) TGFβ1-Induced EMT in the MCF10A mammary epithelial cell line model is executed independently of SNAIL1 and ZEB1 but relies on JUNB-coordinated transcriptional regulation, *Cancers (Basel).* **15**, 558.

8. APPENDIX

8.1. Ethics Approval

İZMİR BİYOTIP VE GENOM MERKEZİ
GİRİŞİMSEL OLMAYAN ARAŞTIRMALAR ETİK KURULU (İBG-GOEK)
KARARI

Toplantı Tarihi	: 25/11/2022	**Toplantı Günü**	: Cuma
Toplantı Sayısı	: 15	**Toplantı Saati**	: 10:30

Sayın None Hani ALOTAIBI,

2022-039 Protokol No'lu; sorumlusu olduğunuz "Epitelyalden Mezenkimale geçişin H3.3 histon varyantı ile epigenetik regulasyonu" başlıklı araştırmanın uygulanmasında etik açıdan sakınca olmadığına oy birliği ile karar verilmiştir.

Bilgilerinizi ve gereğini rica ederiz.

Prof. Dr. H. Alper BAĞRIYANIK **Başkan**	**Dr. Serap ERKEK ÖZHAN** **Başkan Yardımcısı**
Prof. Dr. Sedef AKGÜNGÖR **Üye** (Katılmadı)	**Prof. Dr. İnci ALACACIOĞLU**
Prof. Dr. Gülgün OKTAY **Üye**	**Prof. Dr. Hilmi ORHAN** **Üye**
Prof. Dr. Şermin[illegible] **Üye**	**Doç. Dr. Canan Aslı YILDIRIM** **Üye** (Katılmadı)
Doç. Dr. Can KÜÇÜK **Üye** (Katılmadı)	**Dr. Öğr. Üyesi Yavuz OKTAY** **Üye**

8.2. Publications

Molecular Biotechnology
https://doi.org/10.1007/s12033-025-01478-6

ORIGINAL PAPER

Cost-Effective Production of Biologically Active Leukemia Inhibitory Factor for Mouse Embryonic Stem Cell Culture

Imtiaz Nisar Lone[1] · Esin Ozkuru Sekeroglu[1,2] · Gkamze Impraimoglou Kafaz[1,2] · Abed Alkarem Hani Abu Al Haija[1] · Esra Turker[1] · Tugce Batur[1] · M. Kasim Diril[1,2]

Received: 19 March 2025 / Accepted: 26 June 2025
© The Author(s), under exclusive licence to Springer Science+Business Media, LLC, part of Springer Nature 2025

Abstract
Leukemia inhibitory factor (LIF), a glycoprotein in the interleukin-6 family, is essential for maintaining the pluripotency and self-renewal of mouse embryonic stem cells (mESCs) by activating the JAK/STAT pathway and preventing spontaneous differentiation. Despite its critical role in maintaining the undifferentiated state of ES cells, the high cost of commercially available LIF poses a considerable financial challenge for research laboratories. This financial strain can limit the accessibility and feasibility of high-quality stem cell research, thereby impacting the overall progress in this field. Here, we present an efficient and cost-effective method for recombinant expression and purification of biologically active, non-glycosylated mouse LIF in *Escherichia coli*, which retains full functionality in mESC culture. Utilizing an N-terminal glutathione S-transferase (GST) tag enhances the solubility of LIF, facilitating rapid purification via glutathione-agarose affinity chromatography. Following purification, LIF is cleaved from the GST tag using HRV 3C protease, resulting in a product ready for direct application in mESC culture. Homemade LIF (HM-LIF) prepared with this protocol effectively maintains mESCs in an undifferentiated state, showing comparable efficacy to commercial LIF. Furthermore, mESCs cultured with HM-LIF retain pluripotency and can differentiate into glutamatergic neurons. This streamlined approach significantly reduces the cost of mESC culture while providing a reliable, high-quality alternative to commercial LIF.

Keywords Recombinant HM-LIF · Mouse embryonic stem cell · Affinity chromatography · Pluripotency · Neuronal differentiation

Introduction

Leukemia inhibitory factor (LIF) is a glycoprotein cytokine that belongs to the interleukin-6 (IL-6) superfamily and plays a crucial role in various biologic processes, including cell differentiation, neural development, bone formation, embryogenesis, and inflammation [1–6]. Following its initial translation into a 202 amino acid precursor mRNA, LIF undergoes post-translational processing to produce a mature 20 kDa form, achieved by cleaving 22 amino acids from its N terminus. It derives its name from its ability to inhibit the proliferation of myeloid leukemia cells in culture. In addition to its role in leukemia inhibition, LIF supports the self-renewal and pluripotency of embryonic stem cells (ESCs) by preventing spontaneous differentiation [2]. It acts by binding to its receptor, LIFR, which associates with the glycoprotein 130 (gp130) to form a ternary signaling complex. This complex activates multiple downstream pathways, including JAK/STAT, MAPK, and PI(3)K [7, 8], that sustain ESC pluripotency, self-renewal, and proliferation by engaging core stem cell transcriptional networks [9–11].

Mouse embryonic stem cells (mESCs), isolated from the inner cell mass (ICM) of the preimplantation blastocyst [12], have become a valuable tool in both basic research and regenerative medicine. They are capable of differentiating into all cell types of the body, including germ-line tissues. Since their establishment in the 1980s, a number of advancements have been made in the field of transgenic technology. For example, ESCs can be easily modified by introducing

Imtiaz Nisar Lone and Esin Ozkuru Sekeroglu have contributed equally to this work.

✉ Imtiaz Nisar Lone
imtiaznisar.lone@gmail.com

[1] Izmir Biomedicine and Genome Center, 35340 Izmir, Turkey

[2] Izmir International Biomedicine and Genome Institute, Dokuz Eylül University, Izmir, Turkey

Published online: 08 July 2025

genetic modifications and characterized and selected in vitro before their incorporation in vivo for producing chimeric animals [13]. A critical parameter for using the mESCs for the production of chimeric animals is the ability to isolate and culture murine embryonic stem (ES) cells in vitro. Over the years, ES cell culturing conditions have undergone significant modifications. The objective always being to retain the three basic and characteristic properties of ES cells: pluripotency, self-renewal, and high proliferation. Initially, mESCs were cultured on mouse embryonic fibroblasts (MEFs) in media containing fetal calf serum (FCS) and were shown to differentiate into a larger variety of tissues in solid tumors [14]. However, it was challenging to retain a homogeneous population of fully pluripotent mESCs due to the unknown composition of FCS. Next, the FCS containing medium was conditioned by Buffalo rat liver cells to prevent spontaneous differentiation of mESCs [15]. Later, it was discovered that LIF, secreted by conditioned media from Buffalo rat liver cells, was responsible for preventing the spontaneous differentiation of mESCs [16]. Since then, LIF is routinely added to the culture medium of mESCs and the removal of LIF results in exit from the pluripotency state and rapid differentiation of mESCs. LIF is now recognized to be critical for the regulation of self-renewal and pluripotency in mESCs [2], even though the beneficial effects seem to depend on the genetic background of the mES cells and culture conditions. Recently, further improvements were made in ES cell culture where ES cells are cultured in a medium free from feeders, FCS and LIF. Instead, a combination of small-chemical molecules, which inhibit the MAPK/ERK1/2 and the GSK3 (3i: PD184353, PD173074/SU5402, and CHIR99021) or GSK3 and MEK1/2 (2i: CHIR99021 and PD0325901) are used. The use of these inhibitors in the culture medium (2i or 3i) supports the self-renewal of mESCs in serum-free media and in the absence of LIF [17]. However, the addition of the LIF to the 2i culture further promotes and maximizes the self-renewal of mESCs, highlighting once more the importance of LIF in ESC maintenance [17].

LIF's role in maintaining ESC pluripotency extends beyond basic research; it holds immense potential in regenerative medicine. Pluripotent stem cells, including ESCs and induced pluripotent stem cells (iPSCs), can differentiate into virtually any cell type, offering exciting possibilities for treating previously incurable diseases, such as spinal cord injury, neurological disorders, blindness, and type 1 diabetes [18]. Furthermore, pluripotent stem cells enable the development of patient-specific cell therapies and are instrumental in drug discovery and disease modeling. However, the cost of maintaining ESCs in culture remains a challenge, primarily due to the expensive cytokines and growth factors required for their upkeep, with LIF being one of the costliest components.

To address this issue, recombinant LIF is commonly produced in *Escherichia coli* (*E. coli*), but the protein often misfolds into inclusion bodies [19]. To overcome this, LIF is typically expressed as a fusion protein with glutathione S-transferase (GST), which enhances the solubility of the recombinant protein [20]. Here, we present a simple affinity-based purification method to isolate biologically active recombinant LIF from *E. coli*. By expressing LIF as a fusion product with an N-terminal GST tag, we improve its solubility and avoid the formation of inclusion bodies. The GST-LIF fusion protein can be easily purified using glutathione-agarose beads, and LIF is subsequently cleaved from the tag using HRV 3C protease. The purified non-glycosylated LIF, referred to as homemade (HM-LIF), is biologically active and can be used directly for mESC culture without further purification. We demonstrate that 40 ng/mL of HM-LIF is sufficient to maintain mESCs in an undifferentiated state and that it is as effective as commercially available ESGRO-LIF (1000 U/mL). Furthermore, mESCs cultured with HM-LIF remain pluripotent and are capable of differentiating into glutamatergic neurons, mouse embryonic fibroblasts [21], and laryngeal glands (un published data).

Materials and Methods

Cloning of Mouse LIF into the Bacterial Expression Vector pGEX-6P-1

To generate a LIF expression plasmid, total RNA was isolated from normal murine mammary gland cells (NMuMG) using the NucleoSpin RNA extraction kit (Macherey–Nagel). cDNA synthesis was performed using the Maxima First-Strand cDNA Synthesis Kit (Thermo Scientific). To amplify the coding region for mouse LIF (aa 24–203), we used the primers HM-LIF-F and HM-LIF-R (Table 1), which introduced BamHI and XhoI restriction sites, respectively. The resulting PCR product was digested with BamHI and XhoI and then ligated into the pGEX-6P-1 expression vector between BamHI and XhoI sites, resulting in an N-terminal GST-tagged fusion protein. The recombinant plasmid was transformed into *E. coli* strain BL21 (DE3) for protein expression.

Expression and Purification of GST-HM-LIF

The GST-HM-LIF fusion protein was expressed in *E. coli* BL21(DE3) cells transformed with the pGEX-6P-1-HM-LIF plasmid. Overnight cultures were diluted into fresh LB medium supplemented with ampicillin (100 µg/mL) and grown at 37 °C until OD_{600} reached 0.8. Protein expression was induced with 500 µM IPTG, and cultures were incubated overnight at 16 °C with shaking. Cells were harvested

Table 1 List of primers used in this study

Target Gene	Forward 5' to 3'	Reverse 5' to 3'	Expected Fragment Size (bp)
OCT-4	TCTTTCCCCAGGCCCCCGGCTC	TGCGGGCGGACATGGGGAGATCC	223
SOX-2	CGCGGCGGAAAACCAAGACG	GCCGGCGCCCACCCCAACC	110
NANOG	CCTTCCCTCGCCATCACACT	AGAGGAAGGGCGAGGAGAGG	194
MAP2	GCCAGCCTCGGAACAAACA	GCTCAGCGAATGAGGAAGGA	101
DCX	ATGCAGTTGTCCCTCCATTC	ATGCCACCAAGTTGTCATCA	182
TUJ1	TAGACCCCAGCGGCAACTAT	GTTCCAGGTTCCAAGTCCACC	127
GAPDH	TTCACCACCATGGAGAAGGC	GGCATGGACTGTGGTCATGA	237
mLIF	GATCGGATCCCCTCTTCCCATCACCCCTGTA	GATCCTCGACCTAGAAGGCCTGGACCACCA	552

The primer pairs used for quantitative PCR analysis of pluripotency and neuronal marker genes, along with the expected amplicon sizes. The primer pair used to amplify the LIF gene from mouse cDNA is also shown

by centrifugation, resuspended in lysis buffer (20 mM Tris pH 8.0, 1-M NaCl, 0.1% β-mercaptoethanol, 0.2% Triton X-100, 1-mM EDTA, 2 mM DTT, 1-mM PMSF, 25 µg/mL lysozyme, and protease inhibitor cocktail), and then lysed by sonication. The lysate was treated with universal nuclease (Pierce) in the presence of 1 mM $MgCl_2$ to reduce viscosity and then clarified by centrifugation at 14,000 g for 30 min at 4 °C. The cleared lysate was then transferred to a column containing equilibrated glutathione-agarose beads (Thermo Scientific, Cat# 16100) for 2 h at 4 °C with rotation. An aliquot was taken for SDS gel analysis (SN). After two hours, the binding buffer was allowed to flow through, and an aliquot of flow through (FT) was collected for analysis on an SDS gel (Fig. 1C lane 3). The beads were washed four times, each time with 10 mL of wash buffer (50 mM Tris–Cl pH 8.0, 150-mM NaCl, 1-mM PMSF, 2-mM DTT, 1% Triton X-100) for 10 min on a rotating wheel.

After extensive washing, an aliquot (pre-cleavage, PC) was taken for SDS gel analysis and the remaining bound fusion protein was cleaved on-bead using 20 units of HRV 3C protease (Thermo Scientific) in cleavage buffer (500-mM Tris–HCl, pH 7.5, 1.5-M NaCl) overnight at 4 °C. The eluate containing cleaved HM-LIF was dialyzed against PBS at 4 °C and concentrated using a 10 kDa molecular weight cutoff centrifugal concentrator (Amicon). The final protein purity was assessed by 12% SDS-PAGE. The typical yield of purified HM-LIF was approximately 0.8 mg per 100 mL of bacterial culture.

Culturing Mouse Embryonic Stem Cells (mESCs)

Mouse embryonic stem cells (B6/BLU, ATCC, SCRC-1019) were cultured on gelatin-coated plates in 2i medium (50% DMEM/F-12, 50% Neurobasal medium, 1% FBS, 0.5X B27, 0.5X N2, 0.0025% BSA, 1X penicillin–streptomycin, 55 µM β-mercaptoethanol, 3 µM CHIR99021, and 1 µM PD0325901). The media were supplemented with either commercial ESGRO-LIF (1000 U/mL) or HM-LIF at varying concentrations (20, 40, 60, and 100 ng/mL). The cells were maintained at 37 °C with 5% CO_2, and the growth medium was refreshed daily while passaging was performed every 2–3 days.

Immunofluorescence and Pluripotency Marker Expression

To assess pluripotency, mESCs were cultured on gelatin-coated coverslips for 2 days in 2i media supplemented with either ESGRO-LIF or HM-LIF. Cells were fixed with 3% paraformaldehyde, permeabilized with 0.5% Triton X-100, and blocked with a solution of 1% BSA and 22.5 mg/mL glycine in PBST. The cells were then incubated with primary antibodies against pluripotency markers Sox2 (Cell Signaling Cat#14942), Oct4 (Cell Signaling, Cat# 75463), and Nanog (Cell Signaling, Cat#4903) and subsequently with Alexa Fluor-conjugated secondary antibodies (Invitrogen, Cat# A32742, A11008) (Table 2). Nuclei were stained with DAPI, and images were captured using confocal microscopy (Zeiss LSM880).

Quantitative PCR (qPCR) for Pluripotency Markers

Total RNA was extracted from mESCs cultured in 2i medium supplemented with either ESGRO-LIF or HM-LIF using the RNA purification kit (Macherey–Nagel). cDNA was synthesized with the Maxima First-Strand cDNA Synthesis Kit. qPCRs were performed to measure the expression of pluripotency markers (Sox2, Oct4, and Nanog) using RealQ Plus 2 × Master Mix (Ampliqon) and the Applied Biosystems 7500 Fast Real-Time PCR System. Data were analyzed using the ΔΔCt method to compare relative expression levels and plotted using GraphPad Prism (v.10.2.3). Statistical analysis of qPCRs was evaluated by one-way Anova with Tukey's multiple comparison test where significance represented as ($p < 0.05$, $^{**}p < 0.01$, $^{***}p < 0.001$, $^{****}p < 0.0001$).

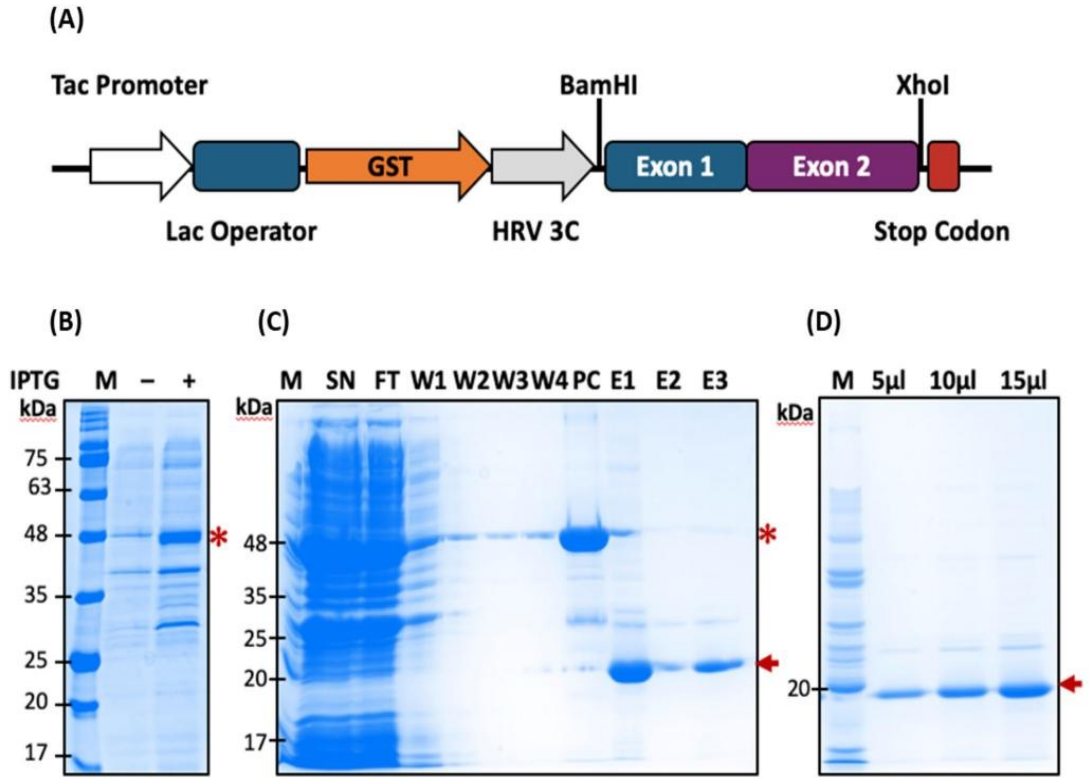

Fig. 1 Cloning and purification of GST-LIF fusion protein. **A** Cloning of mouse LIF into pGEX-6P-1 expression vector. To amplify the coding region of mouse LIF (aa 24–203), we used the primers HM-LIF-F and HM-LIF-R (Table 1), which introduced BamHI and XhoI restriction sites, respectively. The PCR product was then digested with BamHI and XhoI and ligated into the pGEX-6P-1 expression vector between BamH1 and Xho1. **B** Induction of GST-LIF fusion protein analyzed by SDS-PAGE: GST proteins were expressed in *E. coli* BL21 cells and induced with 5 mM IPTG. M: Protein Marker; Lane 1: Uninduced cell lysate; Lane 2: Induced cell lysate. The * indicates GST-tagged LIF (~46 kDa). **C** Glutathione-Agarose purification of GST-LIF. M: Protein Marker; SN: Cleared supernatant following cell lysis (0.2% v/v); FT: Flow-through (0.2% v/v); W1–W4: Wash fractions collected after sequential washes (0.2% v/v). PC: GST-LIF fusion protein pre-cleavage with HRV 3C protease (0.6% v/v); E1–E3: Elution fractions collected after cleavage with HRV 3C protease (1% v/v). Elution fractions E1–E3 were pooled together and concentrated using a 10 kDa molecular weight cutoff centrifugal concentrator. The released LIF protein (~20 kDa) is indicated by an arrowhead and the percentages in the brackets indicate amounts loaded on the gel. **D** SDS analysis of the purified and concentrated HM-LIF

Table 2 List of antibodies used in this study

Antibody	Catalogue No.	Company	Host	MW (kDa)
Anti-Oct4	75463	Cell Signalling	Mouse	45 kDa
Anti-Sox2	14962	Cell Signalling	Rabbit	35 kDa
Anti-Nanog	4903	Cell Signalling	Mouse	42 kDa
Anti-Map2	Ab32454	Abcam	Rabbit	70 kDa
Alexa 594	A32742	Invitrogen	Mouse	
Alexa 488	A11008	Invitrogen	Rabbit	

The information on the antibody target, catalog numbers, host species, and the molecular weight (kDa) of the recognized target protein is shown

Growth Curve Analysis

To assess the impact of HM-LIF on the proliferation of mESCs, we compared the growth rates of the cells cultured in HM-LIF with the mESC cultured in commercial ESGRO-LIF. Briefly, 30,000 cells were plated on a gelatinized 12-well plate in triplicate either in the media prepared with HM-LIF or with ESGRO-LIF. The proliferation rate of the cells was monitored for six days. The cells were collected every day using trypsin and subsequently counted using a Neubauer chamber to assess cell proliferation. These cell counts were used to plot the growth curve. The experiment was repeated three times for reliability and reproducibility. Doubling time was calculated as a critical parameter for evaluating cell growth, during the exponential growth phase,

between 48 and 72 h by the formula of $DT = \Delta t \times \ln(2)/\ln(C48h/C72h)$, where Δt represents the time interval and C indicates the number of cells at the respective time points.

Cell Cycle Analysis

The experimental protocol was performed as previously described [22]. Briefly, Cells were collected at 80% confluency and the supernatant of the culture was collected into a tube. The adherent cells were detached using trypsin and then added to the same tube containing the supernatant. Samples were centrifuged at 2500 rpm for 5 min. The resulting cell pellets were washed with PBS, resuspended in PBS, and fixed by slowly adding ice-cold 100% ethanol (to a final concentration of 70%) while vortexing. Cells were first incubated on ice for 15 min, followed by overnight incubation at − 20 °C. On the following day, cells were washed three times with PBS and stained with a propidium iodide (PI) solution containing 50 µg/mL PI, 1-mg/mL RNase A, and 0.05% Triton X. PI fluorescence was detected using the PerCP-Cy5.5 channel on a BD LSR Fortessa flow cytometer (BD Biosciences, San Jose, CA, USA). Data analysis was conducted using FlowJo software (version 10; FlowJo, OH, USA) with the Watson Pragmatic model.

Neuronal Differentiation

Mouse ES cells (B6-Blu) were differentiated into glutamatergic neurons according to Bibel et al. [23]. Briefly, cells were cultured on mouse embryonic fibroblasts (MEFs) in ES cell media (DMEM-High Glucose, 15% FCS. 1 × NEAA, 55-µM 2-Mercaptoethanol, 1 × Pyruvate, 1 × Penicillin–Streptomycin) supplemented with 40 ng/mL HM-LIF for three passages. Differentiation was started by resuspending the mES cells in differentiation media (DMEM-High Glucose (# 41965039) supplemented with 10% fetal bovine serum (FBS, Gibco, #10500064), 1X Sodium Pyruvate (Panbio, #43100), 1X MEM Non-Essential Amino Acid Solution (Thermo Fisher Scientific, #11140035), 1X Penicillin–Streptomycin (Thermo Fisher Scientific, 15-140-122), and 110 µM 2-Mercaptoethanol (Sigma-Aldrich, #M3148)) and cultured in suspension using non-adherent plates (Griener Bacteriological Petri Dish, #633102) to promote the formation of embryoid bodies. On day 4, retinoic acid (5 µM) was added to the medium and the embryoid bodies were further cultured for another four days in the presence of retinoic acid. On day 8, the embryoid bodies were dissociated using trypsin and plated in Poly-d-lysine hydrobromide (Sigma-Aldrich, #P8638) and laminin (Roche, #11243217001)-precoated plates in N2 medium (DMEM-High Glucose (#41965-039) and DMEM F-12 (#31330038) medium at 1:1 ratio supplemented with 1X N2 supplement (#17502-001), 1X Pyruvate (#Panbio 43100), 0.0025% BSA, 1% Pen-Strep (#15140-122)). Medium was changed after 2 h and 24 h to fresh N2 medium and 2 days after the dissociation to complete medium (DMEM-High Glucose (#41965-039) and Neurobasal medium (#21103049) at 1:1 ratio supplemented with 1X N2 supplement (#17502-001), 1X B27 supplement (#17504044), 1X Pyruvate (#Panbio 43100), 0.0025% BSA, 1% Pen-Strep (#15140-122)). Five days after plating, neurons were analyzed by bright-field microscopy and confocal microscopy and by qPCR for embryonic and neuronal markers. The sequences of the primers used for RT-qPCR are listed in Table 1.

Histologic Analysis of Embryoid Bodies

Histologic analysis was performed by the IBG histology core facility. Day 8 embryoid bodies (EBs) derived from mESCs cultured with HM-LIF were collected, fixed in formalin and embedded into paraffin. Formalin-fixed and paraffin-embedded embryoid bodies were sectioned at 5 µm thickness. For staining, sections were deparaffinized in xylene and rehydrated through a graded ethanol series. Hematoxylin was applied to visualize nuclei, followed by a brief differentiation and bluing step. Subsequently, eosin was used to counterstain cytoplasmic and extracellular matrix components. After dehydration and clearing, slides were cover-slipped using a permanent mounting medium. Bright-field images were acquired using an Olympus BX61 microscope.

Results

Bacterial Expression and Purification of GST-HM-LIF

We successfully expressed GST-tagged HM-LIF in *E. coli* BL21(DE3) using the pGEX-6P-1 expression vector (Fig. 1A). Protein expression was induced with IPTG at mid-log phase, and cells were harvested after overnight incubation at 16 °C. Analysis of whole-cell lysates by SDS-PAGE confirmed the presence of an induced protein band of the expected size for GST-HM-LIF (Fig. 1B, red asterisk).

The clarified bacterial lysate was incubated with glutathione-agarose beads to isolate the GST-tagged fusion protein. SDS-PAGE analysis of the bound fractions and subsequent washes revealed efficient binding and retention of GST-HM-LIF on the affinity matrix (Fig. 1C, lanes 2–7). Following cleavage with HRV 3C protease, a distinct lower-molecular-weight band corresponding to tag-free HM-LIF (~ 20 kDa) was observed in the eluate (Fig. 1C, arrowhead), confirming successful proteolytic removal of the GST tag. The purified protein was further dialyzed and concentrated, and final purity was assessed by SDS-PAGE (Fig. 1D), indicating that the protocol yields highly enriched HM-LIF suitable for downstream applications.

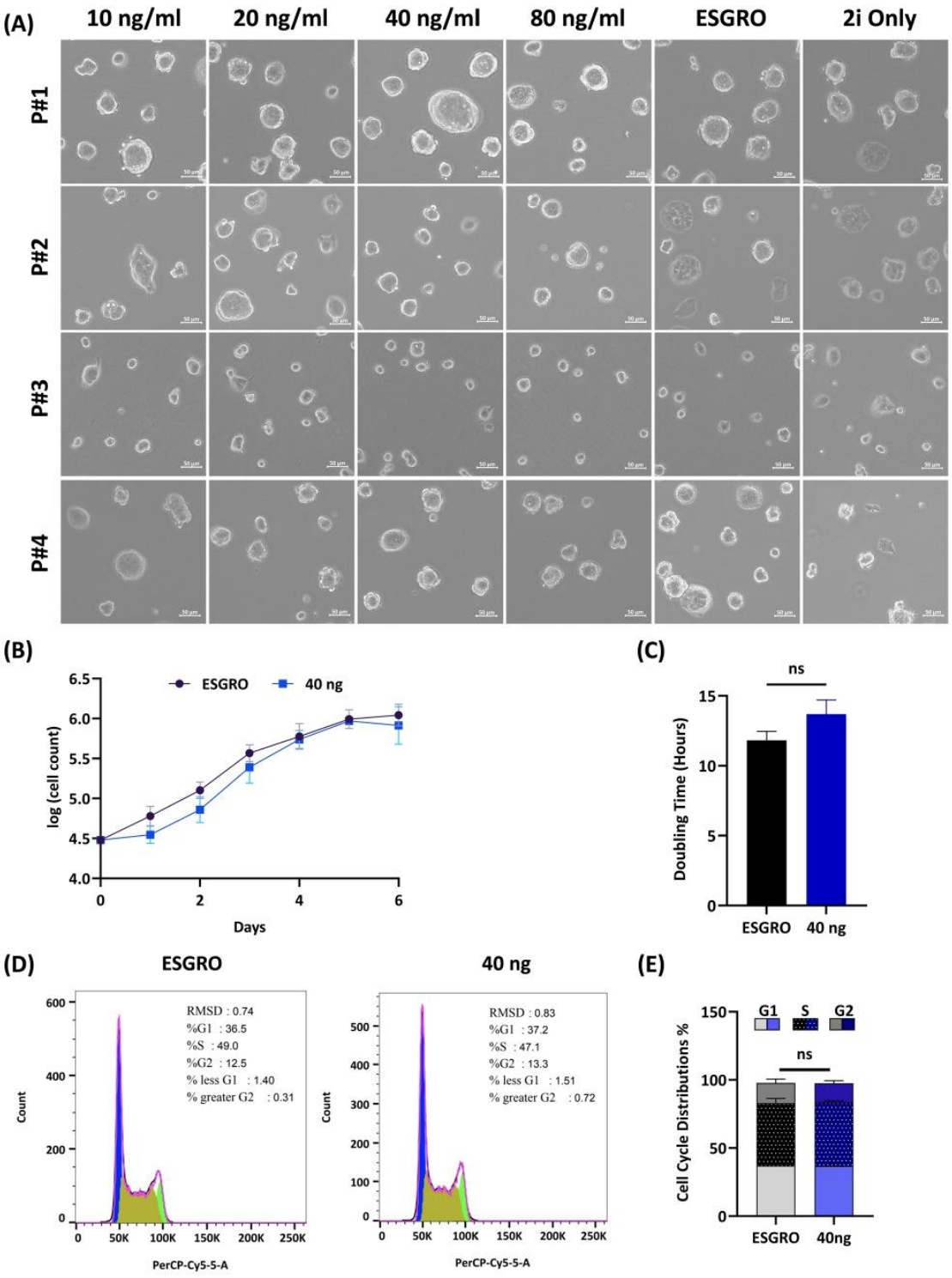
(A)
10 ng/ml
20 ng/ml
40 ng/ml
80 ng/ml
ESGRO
2i Only
P#1
P#2
P#3
P#4
(B)
ESGRO
40 ng
log (cell count)
Days
(C)
ns
Doubling Time (Hours)
ESGRO
40 ng
(D)
ESGRO
RMSD : 0.74
%G1 : 36.5
%S : 49.0
%G2 : 12.5
% less G1 : 1.40
% greater G2 : 0.31
40 ng
RMSD : 0.83
%G1 : 37.2
%S : 47.1
%G2 : 13.3
% less G1 : 1.51
% greater G2 : 0.72
Count
PerCP-Cy5-5-A
(E)
G1
S
G2
ns
Cell Cycle Distributions %
ESGRO
40ng

◂**Fig. 2** Morphology, proliferation, and growth profiles of mESCs cultured on HM-LIF. **A** Bright-field images depicting the effect of LIF concentrations on mouse ESC colonies at different passages (P#1 to P#4). The cells were cultured in a medium supplemented with varying amounts of HM-LIF (20, 40, 60, 80 ng/mL) and compared to cells either cultured in media with 2i only or 2i media supplemented with ESGRO-LIF (1000 U/mL). Healthy mESC colonies are characterized by circular, smooth borders, and a homogeneous pattern, with minimal presence of elongated or flattened cells. Scale bar 50 µM. Note: While only four passages are shown here, HM-LIF is routinely used in our lab for extended culture (up to 10 passages) without adverse effects on cell health or pluripotency. **B** Line graph of the cell growth comparison between cells cultured in 40 ng/mL HM-LIF and ESGRO-LIF, 1000 U/ml. Data represent the average of three independent experiments ($n=3$). **C** Comparison of doubling time of the cells cultured either in ESGRO (1000 U/mL) or HM-LIF (40 ng/mL) during the exponential growth phase, between 48 and 72 h. Data represent the average of three independent experiments ($n=3$). **D** Cell cycle analysis of ESCs treated with either ESGRO (1000 U/mL) or 40 ng/mL HM-LIF. **E** Quantification of cell cycle distribution, expressed as percentages

Optimizing HM-LIF Concentration for B6 Blu mES Cell Culture

To find the optimal concentration of HM-LIF for mESC culture, we cultured B6/BLU mouse embryonic stem cells (mESC) in mESC culture medium containing different concentrations of HM-LIF (0, 20, 40, 60, 80 ng/mL) at 37 °C and 5% CO_2 for four passages. In general, 100,000 cells were plated on 0.2% gelatin-coated 6-well plates. Media was changed every 24 h and cells were passaged every 48 h at around 80% confluence. The cells were washed once with PBS and treated with accutase (Sigma Cat no: A6964) for 3 min to dissociate mESC colonies into single cells and replated at 1:5 passaging ratio. Cells were monitored for their morphology using bright-field microscopy. Healthy mES cells form dome-shaped 3D colonies with highly refractive outer edges (Fig. 2A). Imaging of cells was performed every 24 h from multiple locations for each LIF concentration to analyze the morphological characteristics of mESC colonies. The image acquisition was performed by Olympus CKX41 Inverted Phase Contrast Microscope using two objective magnifications, 4× and 10×. Bright-field imaging demonstrated that cells cultured in media supplemented with either ESGRO-LIF (1000 U/mL) or HM-LIF formed dome-shaped 3D colonies with highly refractive outer edges and exhibited minimal presence of elongated or flattened cells. The cells showed robust proliferation and growth, achieving high confluency. No significant differences were observed between ESGRO-LIF and HM-LIF. Among the tested concentrations, 40 ng/mL of HM-LIF was identified as the optimal concentration for maintaining mESCs, as it consistently supported ideal colony morphology across multiple passages. Although this study focuses on early passage validation, it is worth noting that we routinely culture mESCs with HM-LIF for up to 10 passages in our laboratory without observing any loss of viability, changes in proliferation, or differentiation, indicating sustained efficacy of the recombinant protein over longer-term use.

HM-LIF Maintains the Pluripotency and Proliferation in mESCs Comparable to Commercial ESGRO-LIF

After optimizing the concentration of HM-LIF for mESC culture, we further investigated whether HM-LIF influenced cell proliferation and health differently from ESGRO-LIF. To assess proliferation, a growth curve analysis was performed over 6 days using both ESGRO-LIF and HM-LIF (40 ng/mL). The results showed a slight reduction in the growth rate for HM-LIF during the first 4 days; however, no significant difference was observed between ESGRO-LIF and 40 ng/mL HM-LIF, as both conditions exhibited similar overall growth trends (Fig. 2B). To further analyze growth kinetics, we calculated the doubling time for both conditions based on the growth curve data. This analysis revealed a marginally shorter doubling time for ESGRO-LIF, although no statistically significant difference was detected between the two conditions (Fig. 2C). We investigated the status of the cell cycle, as shown in Fig. 2D and E, both the ESGRO and HM-LIF-supplemented groups exhibited nearly identical phase distributions, indicating that HM-LIF, a cost-effective alternative, is sufficient to support healthy growth and colony formation.

Next, we examined whether mESCs cultured in 2i media supplemented with HM-LIF-expressed pluripotency markers. We compared the expression of these markers in cells cultured with HM-LIF to those cultured in 2i media supplemented with ESGRO-LIF. Immunofluorescence staining was first performed using antibodies against three key pluripotency markers: Sox2, Oct4, and Nanog, which are widely recognized indicators of pluripotency. Our observations revealed that cells cultured with HM-LIF exhibited similar expression levels of these markers compared to cells cultured with ESGRO-LIF (Fig. 3A). Immunofluorescence staining further confirmed the expression and nuclear localization of all three markers. The anti-Sox2 antibody recognizes an epitope around the beginning of the C-terminal domain (CTD) of Sox2 and reveals strong nuclear staining. The anti-Oct4 antibody targets the residues surrounding Phe38 of human Oct4 protein and shows clear nuclear localization, consistent with its role as a transcription factor. Similarly, the anti-Nanog antibody binds to the N-terminal region of Nanog and displays robust nuclear localization. These staining patterns confirm the undifferentiated and pluripotent state of mESCs cultured with HM-LIF.

To further validate these findings, we performed quantitative PCR (qPCR) to assess the gene expression of these pluripotency markers at the molecular level. The

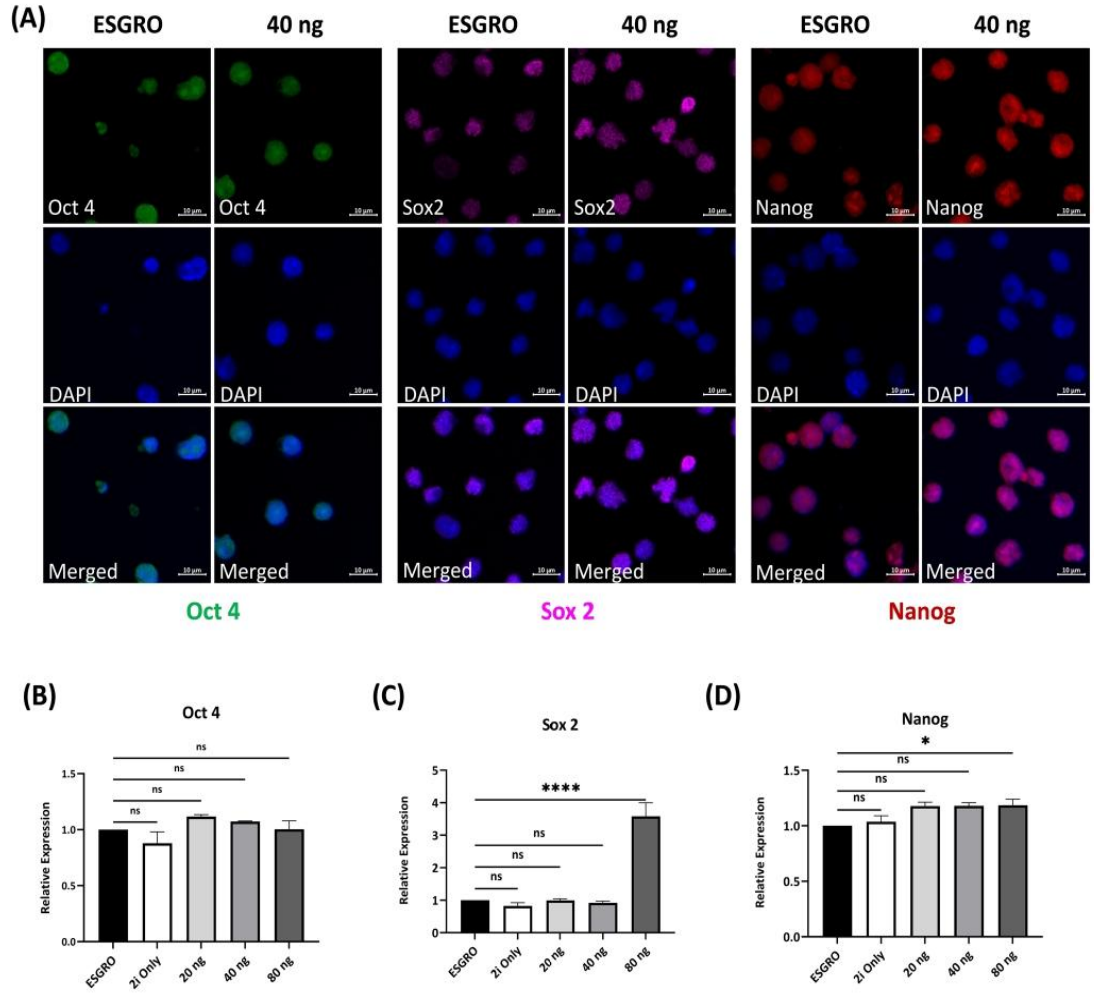

Fig. 3 Analysis of pluripotency marker expression in mESCs cultured with HM-LIF. **A** Immunofluorescence analysis of murine embryonic stem cells (mESCs) showing the expression of pluripotency markers Oct4, Sox2, and Nanog in cells cultured with either ESGRO- LIF or 40 ng/mL HM-LIF. Nuclei were counterstained with DAPI. Scale bar 10 μM. **B** Quantitative PCR (qPCR) analysis of pluripotency marker expression levels (Oct4, Sox2, and Nanog) in mESCs cultured with ESGRO-LIF (1000 U/ml) or with increasing concentrations of HM-LIF (20, 40, and 80 ng/mL). Data represent the average of three independent experiments ($n=3$). (*$p<0.05$, **$p<0.01$, ***$p<0.001$, ns is non-significant)

qPCR results confirmed our immunofluorescence data, showing that the expression of Oct4, Sox2, and Nanog was consistent with what we would expect for pluripotent cells (Fig. 3B). These combined results—both qualitative (immunofluorescence) and quantitative (qPCR)—strongly suggest that the pluripotency of mESCs cultured with HM-LIF is comparable to that of cells cultured with ESGRO-LIF. In conclusion, our data provide compelling evidence that HM-LIF is as effective as ESGRO-LIF in supporting the maintenance of pluripotency in mESCs.

Neuronal Differentiation of the B6/BLU mES Cells Cultured Using Homemade HM-LIF

Once we established that mESCs cultured in 2i media supplemented with HM-LIF formed typical round 3D colonies with refractive outer edges and expressed pluripotency markers, indicating healthy and undifferentiated cells, we then investigated whether these cells could be differentiated to neurons. To assess the potential for neuronal differentiation, B6/BLU mESCs were differentiated into

glutamatergic neurons. The mESCs were initially cultured on mouse embryonic fibroblasts (MEFs) in ES cell media supplemented either with ESGRO-LIF (1000 U/mL) or with 40 ng/mL HM-LIF for three passages (Fig. 4A, panel 1), followed by three passages without feeders. Neuronal differentiation was induced by resuspending the mESCs in differentiation media and culturing them in suspension on non-adherent plates to promote the formation of embryoid bodies (Fig. 4A, panel 2). On day 4 of differentiation, retinoic acid (5 µM) was added to the medium to facilitate neural patterning, and the embryoid bodies were cultured in the presence of retinoic acid for an additional four days. On day 8, the embryoid bodies were dissociated with trypsin and plated on Poly-D-lysine and laminin-coated plates. Neuronal differentiation was evaluated after five days in culture using bright-field microscopy (Fig. 4A, panel 3), immunofluorescence staining for the mature neuronal marker MAP2 (Fig. 4A, panel 4), and qPCR analysis of gene expression (Fig. 4B), including embryonic markers (Oct4, Sox2, Nanog) and neuronal markers (Dcx for postmitotic migrating neurons, and Map2 and Tuj1 for mature neurons). Immunofluorescence for Map2 showed the expected localization in the dendrites of the differentiated neurons, consistent with its known role as a marker of mature neuronal morphology. Similarly, the observed expression profiles from qPCR align well with these roles: Dcx and Tuj1 were upregulated during early neuronal differentiation, while Map2 expression increased at later stages, consistent with progression toward neuronal maturation. Our results demonstrated that B6/BLU mESCs could be successfully differentiated into neurons, with appropriate neuronal markers such as MAP2 being expressed. Additionally, embryonic markers were significantly downregulated during differentiation, confirming the transition from pluripotent to neuronal fates. In addition, we also performed histologic analysis of day 8 embryoid bodies (EBs) generated from mESCs cultured with HM-LIF. Hematoxylin and eosin staining of day 8 EBs revealed the presence of neural rosette-like structures, a hallmark of early neuroectoderm specification. These findings indicate that mESCs maintained in HM-LIF retain the capacity to differentiate into organized neural structures under defined in vitro conditions.

Discussion

In this study, we developed a cost-effective and efficient protocol for the recombinant expression and purification of biologically active mouse leukemia inhibitory factor (LIF) in *Escherichia coli* and demonstrated its application in maintaining the pluripotency of mouse embryonic stem cells (mESCs). Our approach significantly reduces the financial burden associated with LIF, a critical cytokine for mESC culture. By employing a GST-tagged fusion strategy, we ensured high yields and solubility of LIF, facilitating its purification via glutathione affinity chromatography. It is worth noting that while murine LIF is naturally a glycoprotein, the HM-LIF used in our experiments is produced in *E. coli* and is therefore non-glycosylated. Previous studies have demonstrated that glycosylation is not essential for LIF's ability to maintain mESC pluripotency [20, 23, 24]. Consistent with these findings, we show that HM-LIF effectively supports the undifferentiated state of mESCs, with comparable expression of key pluripotency markers and morphology to those maintained with ESGRO-LIF. Thus, HM-LIF represents a functionally competent and cost-effective alternative for mESC culture.

In addition to maintaining pluripotency, we validated the biologic activity of recombinant HM-LIF by demonstrating its ability to support directed neuronal differentiation of mESCs under defined conditions. While neuronal differentiation serves as a representative lineage, our previous work also showed that mESCs cultured with HM-LIF can differentiate into MEF-like cells [21]. This broader differentiation potential highlights the versatility of HM-LIF in supporting lineage commitment across distinct cellular fates. To further complement our in vitro neuronal differentiation assay, we performed histologic analysis of embryoid bodies formed from mESCs cultured in HM-LIF. The observation of neural rosette-like structures, an established marker of early neuroectoderm specification, further validates the ability of HM-LIF to support both self-renewal and differentiation into organized, lineage-specific structures. These findings reinforce the utility of HM-LIF as a reliable reagent for defined in vitro stem cell culture applications.

Taken together, our results demonstrate that non-glycosylated, *E. coli*-derived HM-LIF retains the essential biologic functions of native LIF. It is sufficient to support mESC self-renewal, maintain pluripotency, and enable directed differentiation in vitro, making it a robust and cost-effective alternative to commercially available LIF formulations for basic stem cell research. While glycosylation may contribute to increased stability, in vivo half-life, and reduced immunogenicity, factors important for therapeutic applications. Our results demonstrate that the non-glycosylated form is sufficient and functionally competent for in vitro applications related to stem cell maintenance and directed differentiation.

Previous efforts to produce recombinant mouse LIF in *E. coli*, such as the study by Guo et al. [25], employed an MBP (maltose-binding protein) fusion strategy. While this approach yielded soluble protein, the MBP tag (~43 kDa) was not removed, which may affect LIF's bioactivity and downstream applications. In contrast, our strategy uses a smaller GST tag (~26 kDa), which is efficiently cleaved post-purification, yielding tag-free, bioactive HM-LIF. Our protocol yields ~8 mg/L of purified protein, and

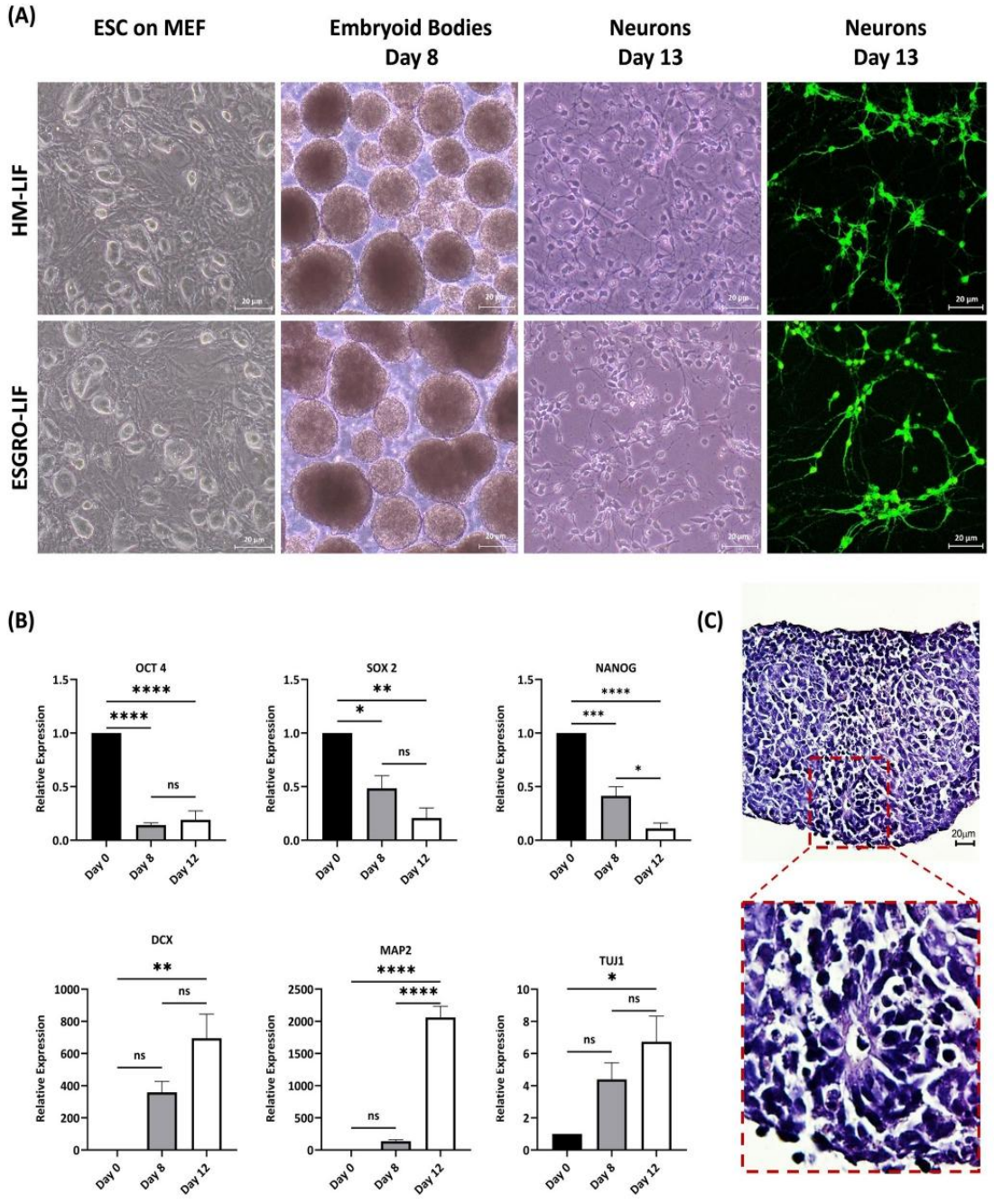

given that only 40 ng/mL is required to support mESC self-renewal, this translates to enough LIF to prepare approximately 40 L of culture medium from a single liter of bacterial culture. The total cost of production, including expression, purification, and cleavage, is estimated at 100–200 EUR. In comparison, purchasing an equivalent amount of ESGRO recombinant mouse LIF costs approximately 8 times more. This clearly underscores the economic advantage of our approach. These improvements in yield, purification, and application offer a practical and scalable alternative to existing protocols.

◂**Fig. 4** Neuronal differentiation of the mESCs cultured on HM-LIF. Morphology of the mES cells at different stages of neuronal differentiation: **A** mES cells were first cultured on MEF feeder cells supplemented with either HM-LIF (40 ng/mL) or ESGRO-LIF (1000 U/mL). Undifferentiated mESCs grown on MEF feeder layers exhibit characteristic dome-shaped colonies with bright, refractive edges. By day 8 of differentiation, cells form embryoid body-like aggregates, before dissociation and plating of neural progenitors. Bright-field images from day 13 show extensive neurite outgrowth and formation of dense neural networks. Immunofluorescence analysis confirms neuronal differentiation by MAP2 expression in both conditions. Scale bar: 20 µm. **B** qPCR analysis of pluripotency and neuronal markers, including Oct4, Sox2, Nanog and Dcx, Tuj1, and Map2, respectively, in mESC cultured 40 ng/mL HM-LIF (*$p < 0.05$, **$p < 0.01$, ***$p < 0.001$, ns is non-significant). **C** Histologic analysis of day 8 embryoid bodies (EBs) derived from mESCs cultured with HM-LIF. Representative hematoxylin and eosin (H&E)-stained sections of day 8 EBs demonstrate the presence of neural rosette-like structures (indicated by square), characteristic of early neural ectoderm differentiation. Scale bar = 20 µm

The ability to generate recombinant LIF at a fraction of the cost of commercial products is a major advantage, particularly for laboratories with limited resources. Using *E. coli* expression systems and affinity chromatography with a GST tag, we were able to obtain high-quality, biologically active LIF in a straightforward and reproducible manner. This streamlined approach not only reduces costs but also improves accessibility for researchers studying pluripotency, differentiation, and regenerative medicine.

In conclusion, our study provides a robust and economical solution for producing high-quality recombinant LIF, which can be used as an effective alternative to ESGRO-LIF in mESC culture. The reproducibility and cost-effectiveness of this method have the potential to democratize stem cell research, making it more accessible to a wider range of laboratories, especially those in resource-limited settings.

Acknowledgements This work was supported by TÜBITAK within the framework of the bilateral cooperation between TÜBİTAK and the Bulgarian Academy of Sciences (BAS), project number 122N046 to I.N.L.

Author Contributions Conceptualization, I.N.L. and K.D.; Methodology, I.N.L, E.O.S, G.I.K, A.A.K, E.T, and T.B; Writing – Original Draft Preparation, I.N.L.; Writing – Review & Editing, I.N.L., E.O.S., and K. D; Supervision, I.N.L.; Project Administration, I.N.L

Data Availability Not applicable.

Declarations

Conflict of interest The authors declare no conflict of interest.

Ethical Approval Not applicable.

Informed Consent Not applicable.

Consent for Publication Not applicable.

References

1. Ohtsuka, S., Nakai-Futatsugi, Y., & Niwa, H. (2015). LIF signal in mouse embryonic stem cells. *Jak-Stat, 4*, 1–9.
2. Williams, R. L., Hilton, D. J., Pease, S., Willson, T. A., Stewart, C. L., Gearing, D. P., Wagner, E. F., Metcalf, D., Nicola, N. A., & Gough, N. M. (1988). Myeloid leukaemia inhibitory factor maintains the developmental potential of embryonic stem cells. *Nature, 336*(6200), 684–687.
3. Murphy, M., Reid, K., Hilton, D. J., & Bartlett, P. F. (1991). Generation of sensory neurons is stimulated by leukemia inhibitory factor. *Proceedings of the National Academy of Sciences, 88*, 3498–3501.
4. Walker, E. C., McGregor, N. E., Poulton, I. J., Solano, M., Pompolo, S., Fernandes, T. J., Constable, M. J., Nicholson, G. C., Zhang, J. G., Nicola, N. A., & Gillespie, M. T. (2010). Oncostatin M promotes bone formation independently of resorption when signaling through leukemia inhibitory factor receptor in mice. *The Journal of Clinical Investigation, 120*(2), 582–592.
5. Stewart, C. L., Kaspar, P., Brunet, L. J., Bhatt, H., Gadi, I., Köntgen, F., & Abbondanzo, S. J. (1992). Blastocyst implantation depends on maternal expression of leukaemia inhibitory factor. *Nature, 359*, 76–79.
6. Banner, L. R., Patterson, P. H., Allchorne, A., Poole, S., & Woolf, C. J. (1998). Leukemia inhibitory factor is an anti-inflammatory and analgesic cytokine. *Journal of Neuroscience, 18*, 5456–5462.
7. Graf, U., Casanova, E. A., & Cinelli, P. (2011). The role of the leukemia inhibitory factor (LIF)—pathway in derivation and maintenance of murine pluripotent stem cells. *Genes, 2*, 280–297.
8. Nicola, N. A., & Babon, J. J. (2015). Leukemia inhibitory factor (LIF). *Cytokine & Growth Factor Reviews, 26*, 533–544.
9. Tang, Y., & Tian, X. (2013). JAK-STAT3 and somatic cell reprogramming. *Jak-Stat, 2*, Article e24935.
10. Chen, X., Xu, H., Yuan, P., Fang, F., Huss, M., Vega, V. B., Wong, E., Orlov, Y. L., Zhang, W., Jiang, J., & Loh, Y. H. (2008). Integration of external signaling pathways with the core transcriptional network in embryonic stem cells. *Cell, 133*, 1106–1117.
11. Niwa, H., Burdon, T., Chambers, I., & Smith, A. (1998). Self-renewal of pluripotent embryonic stem cells is mediated via activation of STAT3. *Genes & Development, 12*, 2048–2060.
12. Evans, M. J., & Kaufman, M. H. (1981). Establishment in culture of pluripotential cells from mouse embryos. *Nature, 292*, 154–156.
13. Bradley, A., Evans, M., Kaufman, M. H., & Robertson, E. (1984). Formation of germ-line chimaeras from embryo-derived teratocarcinoma cell lines. *Nature, 309*, 255–256.
14. Suemori, H., & Nakatsuji, N. (1987). Establishment of the embryo-derived stem (ES) cell lines from mouse blastocysts: Effects of the feeder cell layer. *Development, Growth & Differentiation, 29*, 133–139.
15. Smith, A. G., & Hooper, M. L. (1987). Buffalo rat liver cells produce a diffusible activity which inhibits the differentiation of murine embryonal carcinoma and embryonic stem cells. *Developmental Biology, 121*, 1–9.
16. Moreau, J.-F., Donaldson, D. D., Bennett, F., Witek-Giannotti, J., Clark, S. C., & Wong, G. G. (1988). Leukaemia inhibitory factor is identical to the myeloid growth factor human interleukin for DA cells. *Nature, 336*, 690–692.
17. Ying, Q. L., Wray, J., Nichols, J., Batlle-Morera, L., Doble, B., Woodgett, J., Cohen, P., & Smith, A. (2008). The ground state of embryonic stem cell self-renewal. *Nature, 453*, 519–523.
18. Avior, Y., Sagi, I., & Benvenisty, N. (2016). Pluripotent stem cells in disease modelling and drug discovery. *Nature Reviews Molecular Cell Biology, 17*, 170–182.

19. Samal, B. B., Arakawa, T., Boone, T. C., Jones, T., Prestrelski, S. J., Narhi, L. O., Wen, J., Stearns, G. W., Crandall, C. A., Pope, J., & Suggs, S. (1995). High level expression of human leukemia inhibitory factor (LIF) from a synthetic gene in *Escherichia coli* and the physical and biological characterization of the protein. *Biochimica et Biophysica (BBA) Acta Gene Structure and Expression, 1260*(1), 27–34.
20. Gearing, D. P., Nicola, N. A., Metcalf, D., Foote, S., Willson, T. A., Gough, N. M., & Williams, R. L. (1989). Production of leukemia inhibitory factor in *Escherichia coli* by a novel procedure and its use in maintaining embryonic stem cells in culture. *Bio/Technology, 7*, 1157–1161.
21. Abu Alhaija, A. A., Lone, I. N., Sekeroglu, E. O., Batur, T., Angelov, D., Dimitrov, S., Hamiche, A., Firat Karalar, E. N., Ercan, M. E., Yagci, T., & Alotaibi, H. (2024). Development of a mouse embryonic stem cell model for investigating the functions of the linker histone H1–4. *FEBS Open Bio, 14*(2), 309–321.
22. Batur, T., Argundogan, A., Keles, U., Mutlu, Z., Alotaibi, H., Senturk, S., & Ozturk, M. (2021). AXL knock-out in SNU475 hepatocellular carcinoma cells provides evidence for lethal effect associated with G2 arrest and polyploidization. *International Journal of Molecular Sciences, 22*(24), 13247.
23. Bibel, M., Richter, J., Lacroix, E., & Barde, Y.-A. (2007). Generation of a defined and uniform population of CNS progenitors and neurons from mouse embryonic stem cells. *Nature Protocols, 2*, 1034–1043.
24. Schmelzer, C., Harris, R., Butler, D., Yedinak, C., Wagner, K., & Burton, L. (1993). Glycosylation pattern and disulfide assignments of recombinant human differentiation-stimulating factor. *Archives of Biochemistry and Biophysics, 302*, 484–489.
25. Guo, Y., Yu, M., Jing, N., & Zhang, S. (2018). Production of soluble bioactive mouse leukemia inhibitory factor from *Escherichia coli* using MBP tag. *Protein Expression and Purification, 150*, 86–91.

Publisher's Note Springer Nature remains neutral with regard to jurisdictional claims in published maps and institutional affiliations.

Springer Nature or its licensor (e.g. a society or other partner) holds exclusive rights to this article under a publishing agreement with the author(s) or other rightsholder(s); author self-archiving of the accepted manuscript version of this article is solely governed by the terms of such publishing agreement and applicable law.

8.3. Poster Presentations

8.3.1. 14th EMBO Young Scientists' Forum

Optimization of Cell Culture Media for MCF10A Cells by Forskolin Mediated cAMP Regulation for EMT Studies

Esin OZKURU SEKEROGLU[1], Tuğçe BATUR[2], Şeyma Nur YILDIZ[1], Gkanze IMPRAIMOGLOU KAFAZ[1], Stefan DIMITROV[2], Hani ALOTAIBI[1,2*]

[1]Dokuz Eylul University, Izmir Biomedicine and Genome Institute, Izmir, Turkey
[2]Izmir Biomedicine and Genome Center, Izmir, Turkey
*Correspondence: hani.alotaibi@ibg.edu.tr

IZMIR BIOMEDICINE AND GENOME CENTER

EMBO 14th EMBOYoung Scientists' Forum

BACKGROUND & AIM

Choleratoxin(Ctx) is an essential reagent for the culture medium of MCF10A cells that are characterized by heterogenous levels of epithelial and mesenchymal properties. Ctx induces cyclic-AMP(c-AMP), suggested to have direct effects on epithelial cell growth and integrity [2,4]. By the restrictions on the import of Ctx, absence of the reagent prevents an efficient epithelial to mesenchymal transition(EMT) for MCF10A cells which is a highly complex and critical biological process [1,3]. To overcome, we optimized our culture media using forskolin(Fsk), which is another stimulator, inducing c-AMP pathway.

MATERIALS & METHODS

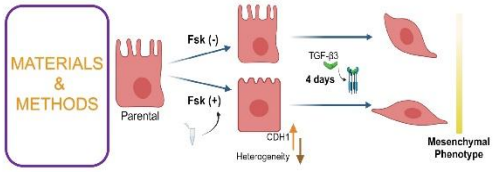

Cells were treated with 1 uM Fsk and the effect on TGFβ3 treatment analysed for Fsk(+) and Fsk(-) cells. Both cells were treated with TGFβ3(5 ng/ml) for 4 days and the expression of EMT-related genes analysed by qPCR. The effect of treatment is also observed morphologically by phase-contrast imaging and immunostaining with E-cadherin and actin antibodies. To adress the localization of E-cadherin as an indicator of proper EMT, we performed flow-cytometry analysis by membrane antibodies Anti-CDH1 and Anti-EpCAM.
Cells also characterised by SrB assay by measurement of the total protein content in the cells after 72h and cell cycle assay by PI staining measured by BD FACSCanto II.

RESULTS & DISCUSSION

Our results suggest that Fsk treatment shows similar effect with Ctx; important for polarization, adhesion and proliferation of epithelial cells. Fsk(+) culture medium, resulted in acquiring epithelial properties such as increased cell-cell junctions, gain of cobblestone characteristics, CDH1(+) cell surface marker profile, decreased actin stress fibers and expression of mesenchymal markers such as CDH2, Fibronectin, Vimentin.

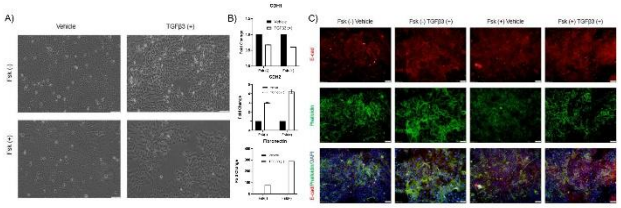

Fig.1. The effect of Forskolin treatment during TGFβ3 mediated EMT on MCF10A cells. A) Phase contrast images of Fsk(+) and Fsk(-) MCF10A cells with TGFβ3 and without (vehicle) TGFβ3 treatment (5 ng/ml) for 4 days. B) The RT-QPCRs showing the expression of CDH1, CDH2 and Fibronectin. C) Immunofluorescence analysis of E-cadherin, actin stress fibres are indicated by phalloidin staining and nuclei were counterstained with DAPI in MCF10A cells with and without TGFβ3 treatment.

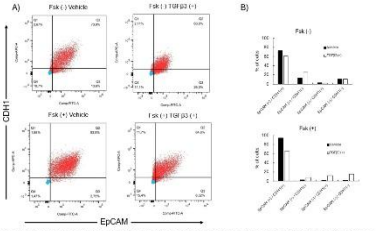

Fig.2. Flow cytometry results for CDH1 and EpCam markers for Parental cells under different Fsk conditions. A) Dot plots of CDH1 and EpCAM Fsk (+) and Fsk (-) cells are shown before and after 4 days of TGFB treatment B) Summary of population analysis

Our results indicated that our population shows heterogeneity and is divided into four groups by EpCAM and CDH1. By the use of Forskolin, CDH1(-) population occilates towards CDH(+) which causes better EMT for MCF10A cells.

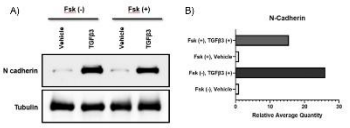

Our results showed that there is increased expression levels of N-cadherin (Fig.3) after the induction of EMT by TGFβ3 showed an efficient transition and an EMT phenotype for both Fsk(+) and Fsk(-) MCF10A cells. Results were also correlated with qPCR experiments (Fig.1.B) as N-cadherin expression is positively related with the expression of mesenchymal makers such as fibronectin while negatively related with the expression of epithelial marker E-cadherin with slight changes on the profile between mRNA and protein level.

Fig.3. Western blot analysis of N-cadherin with and without TGFβ3 treatment for Fsk(+) and Fsk(-) MCF10A cells A) Expression of N-cadherin after 4 days of TGFβ3 treatment. Tubulin was used as loading control . B) Quantification of signal intensity using ImageJ.

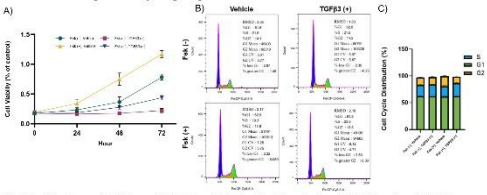

Fsk (+) cells showed higher proliferation rates that is correlating with the morphological data showing healthier profile as characterised by lower actin stress fibres and increased cell-cell junctions.

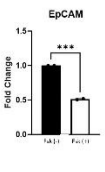

Results also showed that Fsk treatment led to decreased stemness characterized by decreased levels of EpCAM on epithelial population which might be important for th homogenization of cell-line.

Fig.4. Proliferation and Cell Cyce of Fsk (+) and Fsk (-) cells with and without TGFβ3 treatment. A) SrB assay of B) DNA content/cell-cycle analysis of induced EMT and vehicle Fsk (+) and Fsk (-) cells. C) Percentage of cell cycle distribution.

Fig.5. Expression of EpCAM for Fsk (+) and Fsk (-) showed by RT-QPCR.

CONCLUSION

Our study suggests the effect of forskolin on MCF10A cells as an efficient treatment with increasing CDH1(+) cells. Although, further experiments need to be done to validate and better understand the effect of forskolin, results showed optimized culture conditions for both cells' health, maintenance and proper EMT. .

REFERENCES

1. Dongre A. and Weinberg RA. 2019 New insights into the mechanisms of epithelial-mesenchymal transition and implications for cancer. Nat Rev Mol Cell Biol Feb;20(2):69-84. doi: 10.1038/s41580-018-0080-4. PMID: 30459476.
2. Nedvetsky, P.I., Kogan, S. H., Debreath, J., & Mostov, K. E. (2012). Cyclic AMP regulates formation of mammary epithelial acini in vitro. *Molecular biology of the cell*, 23(15), 2973-2981.
3. Pattabiraman, D. R., Bierie, B., Kober, K. I., Thiru, P., Krall, J. A., Zill, C., ... & Weinberg, R. A. (2016). Activation of PKA leads to mesenchymal-to-epithelial transition and loss of tumor-initiating ability. *Science*, 351(6277), aad3680.
4. Wang, Q., & Schulze, B. D. (2014). Cholera toxin enhances Na+ absorption across MCF10A human mammary epithelia. *American Journal of Physiology-Cell Physiology*, 306(5), C471-C484.

iBG-izmir

Acknowledgements: *The study was supported by The Scientific and Technological Research Council of Turkey (TUBITAK) with the project number of 118C354.*

www.ibg.edu.tr

8.3.2. TBS International Biochemistry Congress

Histone Variant H3.3 Associated Regulation of Epithelial to Mesenchymal Transition In Human and Mouse Breast Cell Lines

Esin OZKURU [1], Şeyma Nur YILDIZ [1], Hani ALOTAIBI [1,2], Stefan DIMITROV [2,*]

[1]Dokuz Eylul University, Izmir Biomedicine and Genome Institute, Izmir, Turkey
[2]Izmir Biomedicine and Genome Center, Izmir, Turkey
*Correspondence: stefan.dimitrov@ibg.edu.tr

IZMIR BIOMEDICINE AND GENOME CENTER

BACKGROUND & AIM

EMT is a highly complex process in which epithelial cells lose their polarity, cell-cell junctions and gains mesenchymal properties like increased motility, invasiveness and morphological changes [1,2]. EMT and its regulation has significant importance in cancer and metastasis. Among their important functions in different processes, mutations in histone variant H3.3 are also found in several cancer types. However, the role of histone variants in tumorigenesis and epigenetic regulation of EMT remains elusive. Recent publications showed that the depletion of histone variants such as H2A.Z downregulated epithelial and upregulated mesenchymal markers resulting in an EMT-like phenotype [3,4]. With the overlapping functions of H2A.Z on control of nuclear homeostasis, gene expression and mitosis, histone variant H3.3 might have significant implications on EMT [5,6]. Here, we used loss of function approach to study the effect of H3.3 on EMT progression by comparing two EMT models; MCF10A and NMuMG.

MATERIALS & METHODS

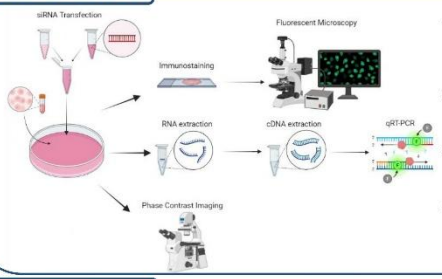

- Human non-tumorigenic breast cell line MCF10A cells and normal murine mammary gland cells NMuMG were transfected with 20 nM siRNA targeting human H3.3A gene using Lipofectamine RNAi Max (13778150, Invitrogen) for 72h.
- Total RNA was isolated from control and H3.3A knock-down cells and converted to cDNA using the Maxima First Strand cDNA Synthesis Kit (K1642, Thermo Scientific).
- cDNA used for qPCR analysis performed to analyse the expression of H3.3A and E-cadherin genes with the AMPIGENE® qPCR Probe Mix (ENZ-NUC107-1000) and Universal Probe Library probes (Roche) and quantified using the ΔΔCt method.
- Immunostaining experiments were also performed with antibodies against E-cadherin (610181, BD Bioscience) and actin (Phalloidin (A12379, Invitrogen)) and nuclei were visualized with DAPI (62248,Invitrogen) by fluorescent microscopy.

RESULTS & DISCUSSION

The transfection of MCF10A cells with siRNA for H3.3A knockdown resulted in a morphological change that can be observed by phase contrast imaging while no significant change is detected on NMuMG cells (Fig.1).

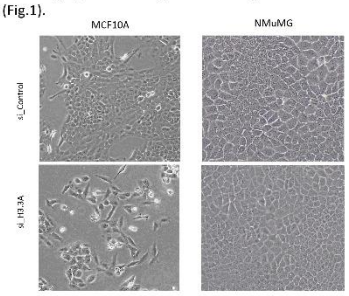

Fig.1. Phase contrast visualizing morphological changes on MCF10A and NMuMG cells.

In correlation, fluorescent images of H3.3A knockdown cells revealed a significant decrease in E-cadherin expression and the presence of actin stress fibers reminiscent of EMT only on MCF10A cells (Fig.2.) .

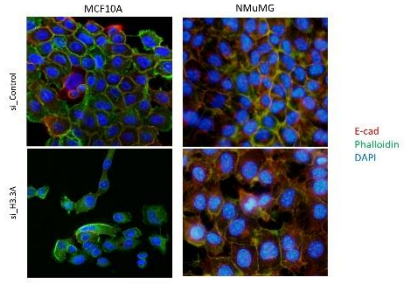

Fig.2. Fluorescent images visualizing morphological changes and localization and levels of E-cad and actin.

The decrease in the loss of RNA expression of H3.3A gene after the depletion of H3.3A showed an efficient knockdown for both MCF10A and NMuMG cells. However, only MCF10A cells showed decreased RNA expression levels of E-cadherin which is a well-characterized marker to analyze epithelial to mesenchymal transition representing an EMT-like phenotype (Fig.3).

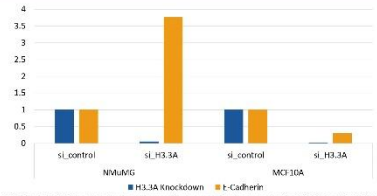

Fig.3. The RT PCRs showing the knockdown efficiency and E-cad expression for MCF10A and NMuMG cells.

CONCLUSION

Our results suggest that H3.3A knockdown leads to EMT-like phenotype in MCF10A while no significant change was detected in NMuMG cells. This novel insight into the epigenetic regulation of EMT by histone variants need to be further studied to understand the contradictory effects in different cells.

REFERENCES

1. Hodge et al. (2018) Histone variant macroH2A1 plays an isoform-specific role in suppressing epithelial-mesenchymal transition. Scientific reports 8.1: 1-11.
2. Dongre A. and Weinberg RA. 2019 New insights into the mechanisms of epithelial-mesenchymal transition and implications for cancer. Nat Rev Mo Cell Biol.Feb;20(2):69-84. doi: 10.1038/s41580-018-0080-4. PMID: 30459476.
3. Domaschenz et.al. (2017) The histone variant H2A.Z is a master regulator of the epithelial-mesenchymal transition. Cell reports 21, 943-952.
4. Weyemi et al. 2016 The histone variant H2A.X is a regulator of the epithelial-mesenchymal transition. Nat Commun 7, 10711.
5. Lone et.al. 2020. The Role of Histone Variants in the Epithelia-To-Mesenchymal Transition. Cells 9, no. 11: 2499.
6. Yukawa et al.(2014. Genome-Wide Analysis of the Chromatin Composition of Histone H2A and H3 Variants in Mouse Embryonic Stem Cells. PLOS ONE 9(3): e92688.

Acknowledgements: *The study was supported by The Scientific and Technological Research Council of Turkey (TUBITAK) with the project number of 118C354.*

www.ibg.edu.tr

8.3.3. MolBiyoKon 2022

IZMIR BIOMEDICINE AND GENOME CENTER

EPIGENETIC REGULATION OF EPITHELIAL TO MESENCHYMAL TRANSITION BY HISTONE VARIANT H3.3A

Esin OZKURU [1], Şeyma Nur YILDIZ [1], N. Kaan KUTLU [1], Gökhan KARAKULAH [1,2], Stefan DIMITROV [2], Hani ALOTAIBI [1,2,*]

[1]Dokuz Eylul University, Izmir Biomedicine and Genome Institute, Izmir, Turkey
[2]Izmir Biomedicine and Genome Center, Izmir, Turkey
*Correspondence: hani.alotaibi@ibg.edu.tr

BACKGROUND & AIM

The epithelial to mesenchymal transition (EMT) is a highly complex and critical biological process playing key roles in developmental and pathological processes characterised by loss of polarity, cell-cell junctions and gain of mesenchymal properties like increased motility, invasiveness and morphological changes [1,2]. Although there are several studies on the function and regulation of EMT by transcription factors, the epigenetic regulation of EMT and especially the role of histone variants is far from being understood. Recent publications showed that the depletion of histone variants such as H2A.Z downregulated epithelial and upregulated mesenchymal markers resulting in an EMT-like phenotype [3,4]. With the overlapping functions of H2A.Z on control of nuclear homeostasis, gene expression and mitosis, histone variant H3.3 might have significant implications on EMT [5,6]. Considering these, we aim to provide an understanding of the epigenetic regulation of EMT by the histone variant H3.3 in human non-tumorigenic breast cell line MCF10A.

MATERIALS & METHODS

Human non-tumorigenic breast cell line MCF10A cells were transfected with 20 nM siRNA targeting human H3.3A gene using Lipofectamine RNAi Max (13778150, Invitrogen) for 72h.

Total RNA was isolated from control and H3.3A knock-down cells and converted to cDNA using the Maxima First Strand cDNA Synthesis Kit (K1642, Thermo Scientific). cDNA used for qPCR analysis performed to analyse the expression of H3.3A and E-cadherin genes with the TaqMan™ Universal Master Mix and Universal Probe Library probes (Roche) and quantified using the ΔΔCt method.

Immunostaining experiments were also performed with antibodies against E-cadherin (610181, BD Bioscience) and actin (Phalloidin (A12379, Invitrogen)) and nuclei were visualized with DAPI (62248,Invitrogen) by confocal microscopy.

RNA sequencing was performed from isolated RNA and used for differential gene expression analysis using R packages. ShinyGo gene-set enrichment tool used to carry out GO analysis of differentially expressed genes including protein coding genes and lncRNAs.

RESULTS & DISCUSSION

The transfection of MCF10A cells with siRNA for H3.3A knockdown resulted in a morphological change that can be observed by phase contrast imaging (Fig.1). Confocal images of H3.3A knockdown cells revealed a significant decrease in E-cadherin expression and the presence of actin stress fibers (Fig.1) reminiscent of EMT.

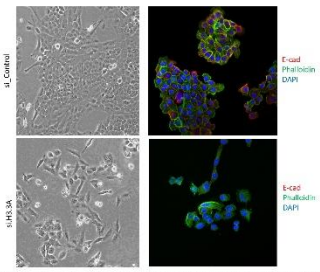

Fig.1. Phase contrast and confocal images visualizing morphological changes and localization and levels of E-cad and actin.

The decrease in RNA expression levels of E-cadherin (Fig.2) and the loss of RNA expression of H3.3A gene (Fig.2) after the depletion of H3.3A showed an efficient knockdown and an EMT-like phenotype accordingly.

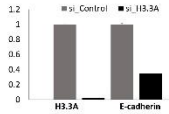

Fig.2. The RT-PCR showing the loss of E-cad and H3.3A expression

704 differentially expressed genes were identified. Among these, 212 upregulated and 492 downregulated genes including widely-accepted EMT markers including, E-Cadherin (Cdh1), Zinc finger E-box binding homeobox (Zeb1/2), E74 Like ETS Transcription Factor 3 (Elf3), Snail Family Transcriptional Repressor 2 (Snai2) were identified (Table 1, Fig.3).

H3.3A	Number of differentially expressed genes				
	total	downregulated		upregulated	
		nGenes	%	nGenes	%
protein coding genes	10463	462	4.42%	179	1.71%
lncRNA genes	1237	30	2.43%	33	2.67%

Table 1. Number and percentage of down-regulated and up-regulated differentially expressed genes.

The results also showed that the depletion of H3.3A histone variant resulted in downregulation of epithelial markers such as Cdh1, Elf3 and Grhl3 and upregulation of mesenchymal markers including Cdh2, Zeb1/2 revealing a major correlation with epithelial to mesenchymal phenotype (Fig.3).

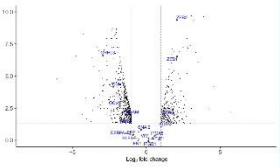

Fig.3. Volcano plot representing down-regulated and up-regulated differentially expressed genes.

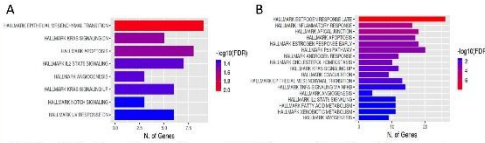

Fig.4. Gene Set Enrichment Analysis of A. up-regulated B. down-regulated differentially expressed genes visualised by bar plot for top enriched biological processes sorted by FDR.

GO enrichment analysis showed that up-regulated genes are enriched on processess including epithelial cell migration, tissue migration, epithelial tube morphogenesis while down-regulated genes are enriched on actin cytoskeleton organization, actin filament organization, cell junction organization, epithelial cell differentiation (Fig.4).

CONCLUSION

The epigenetic regulation of EMT and the role of histone variants haven't been identified to date. Our results suggests that the downregulation of histone variant H3.3A leads to a significant EMT-like effect characterised by the regulation of known EMT markers. Although further experiments need to be done for the validation and better understanding of the role of H3.3 on EMT, our findings present a novel insight into the epigenetic regulation of EMT by histone variants for further research.

REFERENCES

1. Hodge et al. (2018) Histone variant macroH2A2 plays an isoform-specific role in suppressing epithelial-mesenchymal transition. Scientific reports 8.1: 1-11.
2. Dongre A. and Weinberg RA. 2019 New insights into the mechanisms of epithelial-mesenchymal transition and implications for cancer. Nat Rev Mol Cell Biol.Feb;20(2):69-84. doi: 10.1038/s41580-018-0080-4. PMID: 30459476.
3. Domaschenz et al. (2017) The histone variant H2A.Z is a master regulator of the epithelia-mesenchymal transition. Cell reports 21, 943-952.
4. Weyemi et al. 2016 The histone variant H2A.X is a regulator of the epithelial—mesenchymal transition. Nat Commun 7, 10711.
5. Lone et al. 2020. The Role of Histone Variants in the Epithelial-to-Mesenchymal Transition. Cells 9, no. 12: 2699.
6. Yukawa et al.(2014. Genome-Wide Analysis of the Chromatin Composition of Histone H2A and H3 Variants in Mouse Embryonic Stem Cells. PLOS ONE 9(1). e92689.

Acknowledgements: *The study was supported by The Scientific and Technological Research Council of Turkey (TUBITAK) with the project number of 118C354.*

www.ibg.edu.tr

8.4. Curriculum Vitae in Arbis Format

ESİN ŞEKEROĞLU

Personal Information

Contact Information

Contact Address	[redacted]
Phone	[redacted]
Email	[redacted]
Web Page	https://orcid.org/0000-0003-0282-783X

Education Information

04 February 2020 - Now (5 Year 6 Month)
Doktora, Doktora, DOKUZ EYLÜL ÜNİVERSİTESİ, TÜRKİYE
İZMİR ULUSLARARASI BİYOTIP VE GENOM ENSTİTÜSÜ, MOLEKÜLER BİYOLOJİ VE GENETİK (DR) (İNGİLİZCE)
Diploma Number: -

01 September 2015 - 08 May 2018 (2 Year 9 Month)
Yüksek Lisans, Tezli Program, EGE ÜNİVERSİTESİ, TÜRKİYE
FEN BİLİMLERİ ENSTİTÜSÜ, BİYOMÜHENDİSLİK (YL)
Diploma Number: 2017/91/0258
Cumulative Grade Point Average: 3.43 / 4.0

31 August 2010 - 01 July 2015 (4 Year 11 Month)
Lisans, Anadal/Normal Öğretim, EGE ÜNİVERSİTESİ, TÜRKİYE
MÜHENDİSLİK FAKÜLTESİ, BİYOMÜHENDİSLİK PR.
Diploma Number: 2014/05/0395
Cumulative Grade Point Average: 3.16 / 4.0

Experience Information

February 2020 - Now (5 Year 6 Month) (Tam Zamanlı)
DİĞER, DOKTORA ÖĞRENCİSİ, İZMİR BİYOTIP VE GENOM MERKEZİ
Administrative Job: DİĞER

Foreign Language Information

İNGİLİZCE (Reading: İyi, Writing: İyi, Speaking: İyi)

Scientific Technological Activity Fields

Keywords

Biyomühendislik

Moleküler Biyoloji Ve Genetik

Moleküler Genetik

Biyoteknoloji

R&D Competency

Articles

I. N. LONE, E. O. SEKEROGLU, G. I. KAFAZ, A. A. H. A. A. HAIJA, E. TURKER, T. BATUR & M. K. DIRIL, Cost-Effective Production of Biologically Active Leukemia Inhibitory Factor for Mouse Embryonic Stem Cell Culture, MOLECULAR BIOTECHNOLOGY, 2025, 1073-6085, 12, WOS.

A. A. A. ALHAIJA, E. O. SEKEROGLU, T. BATUR, D. ANGELOV, S. DIMITROV, A. HAMICHE, E. N. F. KARALAR, T. YAGCI & M. K. DIRIL et al., Development of a mouse embryonic stem cell model for investigating the functions of the linker histone H1-4, FEBS OPEN BIO, 2024, 2211-5463, null, 13, WOS.

N. KARACA, S. NEMLI, E. OZKURU, H. YILMAZ, B. YAGMUR, C. KARTAL, M. TOSUN, O. O. OCAK, S. OTLES & M. B. TANYOLAC et al., Association mapping of magnesium and manganese concentrations in the seeds of C. arietinum and C. reticulatum, GENOMICS, 2020, 0888-7543, 112, 2, 1633-1642, WOS.

D. ATES, S. NEMLI, E. OZKURU, H. YILMAZ, B. YAGMUR, C. KARTAL, M. TOSUN, O. OZDESTAN, S. OTLES & M. B. TANYOLAC et al., Identification of SNP Markers Associated with Iron and Zinc Concentrations in Cicer Seeds, CURRENT GENOMICS, 2020, 1389-2029, 21, 3, 212-223, WOS.

D. ATES, S. NEMLI, B. YAGMUR, T. K. ASCIOGUL, E. OZKURU, N. KARACA, H. YILMAZ, D. ESIYOK & M. B. TANYOLAC et al., Genome-wide association studies of Ca and Mn in the seeds of the common bean (Phaseolus vulgaris L.), GENOMICS, 2020, 0888-7543, 112, 6, 4536-4546, WOS.

E. ORMAN, D. ATES, E. OZKURU, S. HEPAKSOY, S. KAFKAS & M. B. TANYOLAC, Association mapping of several nut characters in walnut (Juglans regia L.), TURKISH JOURNAL OF AGRICULTURE AND FORESTRY, 2020, 1300-011X, 44, 2, 208-227, WOS.

E. OZKURU, D. ATES, S. NEMLI, S. ERDOGMUS, H. YILMAZ, B. YAGMUR, C. KARTAL, S. OTLES, A. KAHRIMAN & B. TANYOLAC et al., Association mapping of loci linked to copper, phosphorus, and potassium concentrations in the seeds of C. arietinum and C. reticulatum, GENOMICS, 2019, 0888-7543, 111, 6, 1873-1881, WOS.

D. ATES, H. H. ALTINOK, E. OZKURU, F. FERIK, S. ERDOGMUS, C. CAN & M. B. TANYOLAC, Population structure and linkage disequilibrium in a large collection of Fusarium oxysporum strains analysed through iPBS markers, JOURNAL OF PHYTOPATHOLOGY, 2019, 0931-1785, 167, 10, 576-590, WOS.

D. ATES, S. NEMLI, S. ERDOGMUS, N. KARACA, B. YAGMUR, C. KARTAL, O. O. OCAK, S. OTLES & M. B. TANYOLAC et al., Genome-wide association studies of molybdenum and selenium concentrations in C. arietinum and C. reticulatum seeds, MOLECULAR BREEDING, 2019, 1380-3743, 39, 3, WOS.

D. ATES, S. NEMLI, H. YILMAZ, B. YAGMUR, C. KARTAL, M. TOSUN, O. OZDESTAN, S. OTLES & P. CHANG et al., Genome-Wide Association Studies of Protein, Lutein, Vitamin C, and Fructose Concentration in Wild and Cultivated Chickpea Seeds, CROP SCIENCE, 2019, 0011-183X, 59, 6, 2652-2666, WOS.

Conference Papers

E. ŞEKEROĞLU, T. BATUR, Ş. N. YILDIZ, S. DIMITROV & H. ALOTAİBİ, Optimization of Cell Culture Media for MCF10A Cells by Forskolin Mediated cAMP Regulation for EMT Studies, Poster Sunumu, 14th EMBO Young Scientists' Forum, 10 September 2024, 11 September 2024.

E. ŞEKEROĞLU, S. N. YILDIZ, H. ALOTAİBİ & S. I. DIMITROV, HISTONE VARIANT H3.3 ASSOCIATED REGULATION OF EPITHELIAL TO MESENCHYMAL TRANSITION IN HUMAN AND MOUSE BREAST CELL LINES, Poster Sunumu, TBS INTERNATIONAL BIOCHEMISTRY CONGRESS 2022, 26 October 2022, 30 October 2022, 1303-829X, 50, S3, 130 - 130.

S. N. YILDIZ, E. ŞEKEROĞLU, H. ALOTAİBİ & S. I. DIMITROV, THE FUNCTION OF THE HISTONE VARIANT H2A.Z-1 IN THE EPITHELIAL TO MESENCHYMAL TRANSITION IN VARIOUS CELL TYPES, Poster Sunumu, TBS INTERNATIONAL BIOCHEMISTRY CONGRESS 2022, 26 October 2022, 30 October 2022, 1303-829X, 50, S3, 130 - 130.

Y. K. K. G. D. A. OZKURU.E., Epigenetic regulation of epithelial to mesenchymal transition by histone variant H3.3A., Poster Sunumu, 8th International Congress of the Molecular Biology Association of Turkey (MolBiyoKon22), 09 June 2022, 12 June 2022, Poster no:5, Poster Session:1, Abstract book - Poster no:5, Poster Session:1, Abstract book.

O. K. K. G. A. D. YİLDİZ.N.S., The Effect of Histone Variant H2A.Z-1 Knockdown In Epithelial To Mesenchymal Transition., Poster Sunumu, 8th International Congress of the Molecular Biology Association of Turkey (MolBiyoKon22), 09 June 2022, 12 June 2022, Poster no:14, Poster Session: 3, Abstract book - Poster no:14, Poster Session: 3, Abstract book.

E. ÖZKURU & S. E. A. A. D. O. E. K. N. F. F. E. S. O. E. E. S. T. NEMLI, Association Mapping of Fruit Firmness, Weight and Colour in Apricot (Prunus armeniaca L.), Poster Sunumu, I.International Green Biotechnology Congress, 11 September 2017, 13 September 2017, Poster no:MM12, Abstract book, 74 - Poster no:MM12, Abstract book, 74.

S. E. A. A. D. O. E. K. N. F. F. K. N. E. S. O. E. E. S. T. M. NEMLİ, Genetic Diversity of Apricot Revealed by Genotyping by Sequencing (GBS) Technology, Poster Sunumu, I. International Green Biotechnology Congress, 11 September 2017, 13 September 2017, Poster no:MM14, Abstract book, 76, - Poster no:MM14, Abstract book, 76,.

S. E. A. A. D. O. E. K. N. F. F. E. S. O. E. E. S. T. M. NEMLİ, Genome-Wide Association Study (GWAS) of Some Fruit Characters Through Diversity Arrays Technology (DArT) Markers of Apricot Gerplasm in Turkey, Poster Sunumu, I. International Green Biotechnology Congress, 11 September 2017, 13 September 2017, Poster no:MM16, Abstract book, 78 - Poster no:MM16, Abstract book, 78.

E. ŞEKEROĞLU & S. A. D. O. E. K. N. Y. B. K. C. O. S. T. M. O. O. K. A. T. M. NEMLI, Population Structure and Genetic Relationship of Wild (Cicer reticulatum L.) and Cultivated (Cicer arietinum L.) Chickpea Accessions Revealed by GBS Analysis., Poster Sunumu, I. International Green Biotechnology Congress, 11 September 2017, 13 September 2017, Poster no:MM13, Abstract book, 75 - Poster no:MM13, Abstract book, 75.

TÜBİTAK Scholarships and Fundings

Project Info

122N046, Sağlıkta ve Rahman Sendromunda Bağlayıcı Histon H1E, Burslu (Doktora), Sonuçlandı, UPAG - Uluslararasi I?şbi?rli?gi? Projeleri? Araştirma Destek Grubu, Uluslararası / BULGAR, ARDEB, Project Participation/Leave Dates: 3/1/23 - (), Project Start/End Dates: 10/1/22 - 10/1/24.

120N556, Mezenkimal Epitelyal Dönüşümün Epigenetiği, Burslu (Doktora), Sonuçlandı, UPAG - Uluslararasi I?şbi?rli?gi? Projeleri? Araştirma Destek Grubu, Uluslararası / PIA-Bosphorus-Fransa, ARDEB, Project Participation/Leave Dates: 12/29/22 - 3/1/23, Project Start/End Dates: 3/1/21 - 3/1/23.

118C354, Epigenetics of Epithelial-to-Mesenchymal and Mesenchymal-to-Epithelial Transitions : Role of Histone Variants and Pioneer Transcription Factors, Burslu (Doktora), Sonuçlandı, Bilim İnsanı Destek Programları Başkanlığı, BİDEB-2232 / Lider Araştırmacılar Programı- Deneyimli Araştırmacı, BİDEB, Project Participation/Leave Dates: 2/1/20 - 12/1/22, Project Start/End Dates: 12/1/19 - 12/1/22.

214O278, Genome Wide Association Studies (Gwas), Genotyping By Sequencing (Gbs) Ile Ssr Metodlarını Kullanarak Kültür (Cicer Arietinum L.) Ve Yabani Nohut (C. Reticulatum) Populasyonlarında Danede Besin Elementi Ve Besin Değeri Bileşenleri Ile Ilişkili Dna Markörlerinin Saptanması, Burslu (Yüksek Lisans), Sonuçlandı, TOVAG - Tarim, Ormancilik Ve Veteri?nerli?k Araştirma Destek Grubu, 1001 - Araştirma, ARDEB, Project Participation/Leave Dates: 11/7/17 - (), Project Start/End Dates: 5/1/15 - 5/1/18.

114O555, Fasulyede (Phaseolus Vulgaris L.) Genotyping By Sequencing (Gbs) Ve Ssr Markörlerini Kullanarak Danede Besin Elementleri Alınımını Kontrol Eden Genlerle Ilişkili Olan Dna Markörlerinin İlişki Haritalama Metodu (Association Mapping) İle Saptanması, Burslu (Yüksek Lisans), Sonuçlandı, TOVAG - Tarim, Ormancilik Ve Veteri?nerli?k Araştirma Destek Grubu, 1001 - Araştirma, ARDEB, Project Participation/Leave Dates: 9/15/15 - 10/30/17, Project Start/End Dates: 11/15/14 - 11/15/17.

BIDEB Supports

ESİN ŞEKEROĞLU, Bilim İnsanı Destek Programları Başkanlığı, 2250-Lisansüstü Bursları Performans Programı, Destek Sona Erdi, 2022 - 1.

ESİN ŞEKEROĞLU, Bilim İnsanı Destek Programları Başkanlığı, 2250-Lisansüstü Bursları Performans Programı, Destek Sona Erdi, 2023 - 1.

ESİN ŞEKEROĞLU, Bilim İnsanı Destek Programları Başkanlığı, 2250-Lisansüstü Bursları Performans Programı, Destek Sona Erdi, 2023 - 2.

ESİN ŞEKEROĞLU, Bilim İnsanı Destek Programları Başkanlığı, 2250-Lisansüstü Bursları Performans Programı, Destek Sona Erdi, 2024 - 1.

Number of Panelist/Observer/Reporter Jobs

Role	ARDEB	BIDEB	SCIENCE SOCIETY	UIDB	TEYDEB	Total
Refereeing/Panelist/Outer Consultant Count	0	0	0	0	0	0
Moderatorships Count	0	0	0	0	0	0
Number of Observer/Consultant Jobs	0	0	0	0	0	0
Number of Reporter Jobs	0	0	0	0	0	0
Not Attended Refereeing/Panelist/Outer	0	0	0	0	0	0